Criterion-III:

Research, Innovations and Extension

3.3 Research Publications and Awards

3.3.1 Number of research papers published per teacher in the Journals notified on UGC care list during the last five years during the last five years

Date: 06/12/2023

DECLARATION

This is to declare that our college has submitted the Self-Study Report (SSR) for NAAC. After verification of SSR, NAAC raised some queries in Data verification and Validation (DVV) **Metric ID 3.3.1(3.3.1.1)** The college resolved regarding queries and resubmit the document in DVV.

The information, reports, true copies of the supporting documents, numerical data etc. submitted/presented in the files is verified by Internal Quality Assurance Cell (IQAC) and it is correct as per the record.

This declaration is for the purpose of NAAC accreditation of HEI for the 1st cycle period 2018-19 to 2022-23.

Date: 23/01/2024

Place: Shirsondi

IQAC Coordinator
Arts, Science & Commerce College
Shirsondi, Tal. Malegaon (Nashik)

Arts, Science & Commerce College Shirsondi Tal. Malegaon (Nashik)

Principal
Arts, Science & Commerce College
Shirsondi, Tal.Malegaon Dist.Nashik

Criterion III – Research, Innovations and Extension 3.3.1QnM

3.3.1.1. Number of research papers in the Journals notified on UGC care during 2018-19 to 2022-23

Total Number of research Articles/Papers: 2018-2023: - 07

Year	2022-23	2021-22	2020-21	2019-20	2018-19	Total
Number	02	05	00	00	00	07

Table of Contents

Criterion III – Research, Innovations and Extension 3.3.1QnM

List of the Research Articles/ Papers

Sr. No	Title of paper	Name of the author/s	Department of the teacher	Year of Publication	ISSN number	Link to the recognition in UGC enlistment of the Journal
1	Study of p-n Hetero junction Thin Films for Reducing Gas Sensing Application Fabricated by Thermal Evaporation Technique.	Dr. U. J. Tupe	Electronics	06-06-2022	1662-8985	Vol. 1172, pp. 67-82 doi:10.4028/p-2zz6i6
2	Influence Of Annealing Temperature In Structural And Electrical Properties Of Screen Printed Lanthanum Oxide Thick Films.	Dr. U. J. Tupe	Electronics	04-12-2022	1735-0808	January 2019, Volume 6, Issue 1 [1872- 1878]
3	Synthesis techniques and applications of rare earth metal oxides semiconductors: A review	Dr. U. J. Tupe	Electronics	15-03-2022	139555	139555 https://doi.org/10.1016/j.cplett.2022.139555
4	SYNTHESIS AND CHARACTERIZATIONS OF CUO-ZNO NANO COMPOSITE BINARY OXIDE THICK FILMS AS H_2S GAS SENSOR	Dr. U. J. Tupe	Electronics	02-02-2022	2320-2882	Volume 10, Issue 2 February 2022, Page-302-309
5	Review on: Synthesis of	Dr. U. J. Tupe	Electronics	02-02-2022	2320-2882	Volume 10, Issue 2 February 2022, Page-

	Perovskite using Sol-Gel approach					**289-301**
6	**Review on: IoT based Air pollution monitoring techniques**	**Dr. U. J. Tupe**	**Electronics**	**02-02-2022**	**2320-2882**	**Volume 10, Issue 2 February 2022, Page-242-247.**
7	**Synthesis And Characterization Of Zinc Oxide Nanoparticles Using Green Synthesis Method**	**Dr. U. J. Tupe**	**Electronics**	**02-02-2022**	**2320-2882**	**Volume 10, Issue 2 February 2022, Page-302-309.**

Advanced Materials Research
ISSN: 1662-8985, Vol. 1172, pp 67-82

Submitted: 2021-11-12
Revised: 2022-03-23
Accepted: 2022-04-01
Online: 2022-06-06

Study of p-n Heterojunction Thin Films for Reducing Gas Sensing Application Fabricated by Thermal Evaporation Technique

Upendra D. Lad[1,a*], Namdeo S. Kokode[2,b], Umesh. J. Tupe[3,c]

[1,2] Research Centre in Physics, Department of Physics, N.H. College, Bramhapuri, Dist- Gadchiroli, (MS) India.

[3]Department of Electronics, Vidya-Amrut Dnyan Pratishtan's, Arts, Science & Commerce College, Shirsondi, Tal: - Malegaon Dist: - Nashik, (MS) India.

[a*]upendra.lad@gmail.com, [b]drns.kokode@gmail.com [c]umeshtupe14@gmail.com

Keywords: Heterojunction, Reducing gas, metal oxide semiconductor, Thermal Evaporation Technique, liquefied petroleum gas.

Abstract. Gas sensors have been widely implemented to address concerns about air pollution, monitor human health, and increase crop yields. Because of their high sensitivity, quick response time, and short recovery time, metal oxide semiconductor (MOS) gas sensors have become a significant topic of research in the field of gas sensing. In the last decade, many researchers have been working on the different types of pure and doped MOS to improve gas sensor response. The present research work deals with the fabrication of p-n heterojunction thin films on an alumina substrate by using the thermal evaporation technique for reduced gas sensing applications. In the current research work, ZnO is used as a functional material and MgO as a dopant. The structural, electrical, and gas sensing properties of fabricated p-n (CuO-ZnO) heterojunction thin films were studied. The resistivity of p-n heterojunction thin films was found to be 23.461Ω/m. The TCR was found to be negative for p-n heterojunction thin films. The morphological, elemental, and structural characterization of fabricated CuO-ZnO heterojunction thin films were analysed by using SEM, EDAX, and XRD standard tools, respectively. By using Scherer's formula, the crystallite size of CuO-ZnO heterojunction thin films was found to be 36.83 nm. The fabricated CuO-ZnO heterojunction thin films were exposed to reducing gases such as liquefied petroleum gas (LPG), ammonia (NH_3), ethanol (C_2H_5OH), and dichlorofluoromethane (R12) to determine gas response and selectivity. Fabricated CuO-ZnO heterojunction thin films show a maximum response to LPG gas as compared to other gases. The maximum sensitivity has to be found at 89.23% to LPG gas at a concentration of 300 ppm. Fabricated MgO-ZnO thin films also show fast response and recovery time in seconds.

1. Introduction

Pollution surveillance, biosensors, and agriculture are just a few of the applications for gas sensors in daily life [1]. Semiconductor gas sensors can detect a particular target gas by changing the impedance of a sensing body, which is a porous assembly of small crystals or particles of oxide semiconductors like ZnO, SnO_2, CuO, WO_3, etc. [2, 3]. Chemical and thermal properties are both stable over time. The sensors are mostly used to estimate real amounts as well as to run a few structures. A sensor is an electronic device that detects a variety of different input signals. The high demand for gas detection and monitoring has created a challenge. Exposure to poisonous and hazardous gases can result in cardiac problems, respiratory disorders, and cellular disintegration in the lungs, haemoglobin depletion, cognitive disability, edema, and other difficulties. Automobile emissions and technological waste damage the atmosphere [3, 4].

Gas sensors made of metal oxide semiconductors (MOS) and nanocomposites are quite popular because of their quick detection, ease of use, and low cost [5]. Due to their wide range of applications in fields such as photovoltaic panels, photocatalysts, sensors, microelectronic circuit fabrication, piezoelectric devices, fuel cells, display panels, optoelectronics, gas sensors, and other fields, metal oxide thin films and nanostructures have attracted much interest during the last decades. The development of thin ZnO films has sparked particular interest among them [6, 7].

Nanomaterials with diameters of fewer than 100 nanometers are now being studied in a variety of applications. Nanoparticles have a large surface-to-volume ratio, which is advantageous for gas sensing [8]. In addition to noble metal ornamentation, doping can be used to improve the features of chemical resistance gas sensors. Certain researchers have used doping to improve MOS sensor properties like sensitivity, reaction time, and recovery time. Dopants include metal oxide, noble metals such as Au, Pt, Pd, Ag, Cu, Co, non-metallic elements, and others [9, 10]. The p–n heterostructures, which are made up of n-type and p-type MOSs, have been widely explored in the field of gas sensing core-shell nanostructures. Researchers have been looking into CuO-ZnO heterostructured H_2S gas sensors ever since Kim et al. reported that CuO-SnO_2 nanostructures were good at detecting H_2S gas [11, 12].

The contact transition region formed at the interface between two semiconductors with different bandgap widths is referred to as a heterojunction. As we all know, P-type semiconductors and n-type semiconductors are two types of semiconductors. As a consequence, a heterojunction can be divided into two types: homogeneous heterojunctions (n-n and p-p heterojunctions) and heteromorphic heterojunctions (p-n heterojunctions). Heterojunctions can be found in nanoparticles, nanosheets, flower-like hollow microspheres, nanofibers, nanorods, and nanoneedles, among other structures [11-13].

People are interested in research on heterogeneous materials and devices because the two materials have different chemical and physical properties, such as band structure, dielectric constant, lattice constant, and electron affinity, which make the heterojunction different from other types of materials.

Several researchers synthesised p-n heterojunctions and demonstrated their utility in a variety of fields. Thermal decomposition, co-precipitation, chemical vapour deposition, sol-gel and wet-impregnation procedures, complex-directed hybridization, and heating brass in the air have all been used to synthesise CuO-ZnO nanocomposites. P-N heterojunction, thin films or nanocomposites, on the other hand, are better for some practical applications than pure metal oxide [13, 14].

Thermal evaporation is the most effective technique for the fabrication of p-n heterojunction thin films. Vaporization of the material to be deposited, vapour transmission from the source to the substrate, and lastly, condensation on the substrate surface are all physical processes of film deposition. The process is ideally carried out under a vacuum to avoid the formation of dense films. In the deposition of thin films, nucleation and growth are necessary. The atoms and molecules on the substrate surface lose thermal energy during nucleation. The strength of the deposited film is determined by the physical and chemical interactions between the thin-film material and the substrate surface. This technique is efficient, inexpensive, non-catalytic, and requires low-temperature growth [6, 15, 16].

Zinc oxide (ZnO) is a nontoxic n-type semiconducting material with a large direct band gap (Eg = 3.37 eV) at ambient temperature and a high exciton binding energy (60 meV) [17]. Undoped ZnO typically shows n-type conductivity with a typical carrier concentration due to intrinsic defects of oxygen vacancies and zinc interstitials. ZnO thin films have a variety of micro morphologies and properties, so it's possible to improve the electrical and gas sensing properties of ZnO thin films using purposeful doping and appropriate synthesis processes. Many ZnO studies currently focus on doping elements to reduce the film's resistivity. As a result, numerous studies have been conducted on n-type doping. It has been shown that ZnO-coated electronics can be used for a wide range of things, which has led to a lot of attention in the field of gas sensors [18, 19].

In the present research work, the authors have emphasised the fabrication of p-n heterojunction thin films on an alumina substrate by using sophisticated thermal evaporation techniques. This present work focuses on the study of structural, electrical, and gas sensing properties of fabricated p-n (CuO-ZnO) heterojunction thin films for reducing gas.

2. Materials and Methods

2.1 Fabrication of p-n heterojunction thin films by thermal evaporation technique

Commercially available AR grade (99.99% purity) nanopowder of ZnO and CuO were used in this study. For p-n heterojunction fabrication, ZnO was utilised as the base and CuO as the dopant material. All the films were developed on a clean alumina substrate. For fabricating thin films, all substrates were thoroughly cleaned with acetone and then exposed to an IR lamp for 30 minutes to remove contaminants. The thermal evaporation technique was used to make thin films. The system consists of a vacuum pump system that was evacuated to a pressure of 10^{-5}-10^{-6} mbar using a rotational and diffusion pump setup as indicated in Figure 1. A vacuum was formed inside the chamber, and clean alumina substrates were placed inside the deposition chamber. A molybdenum boat was placed in a molybdenum boat using a conventional arrangement, and a high-voltage power supply was provided to the evaporation target. The fabricated thin films were then annealed in a muffle furnace at 650 °C for 2 hours before being used in future research.

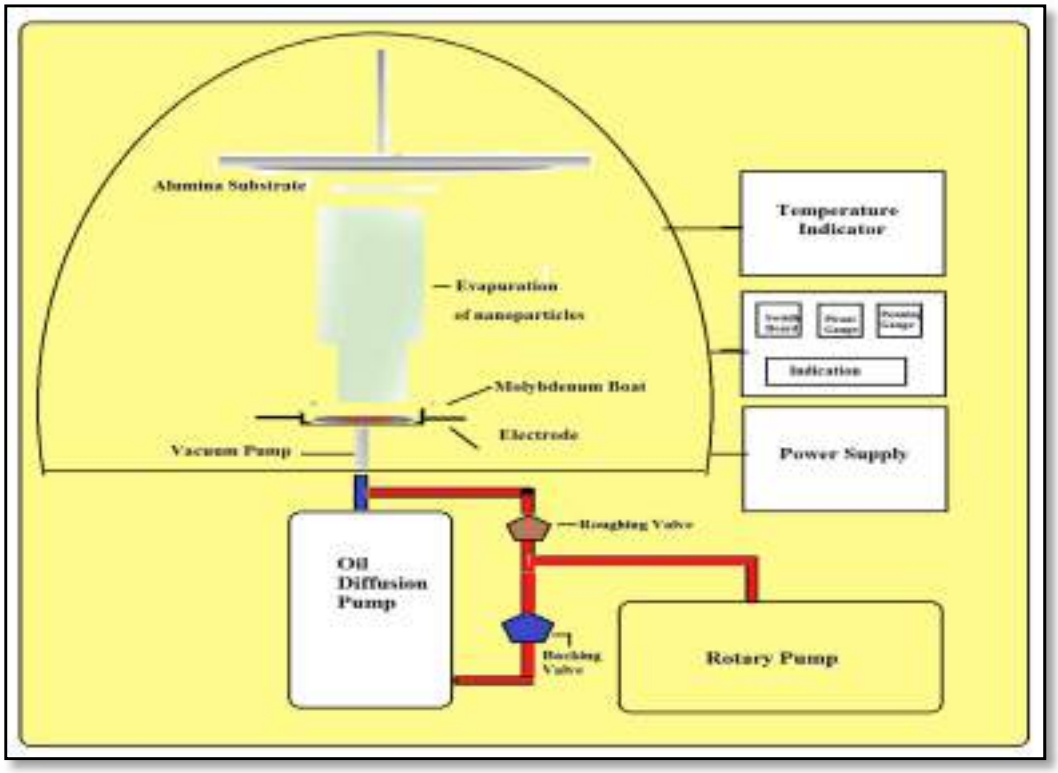

Fig.1 Schematic of thermal evaporation technique for thin film fabrication

2.2 Structural Characterization

The fabricated CuO-ZnO heterojunction thin films were characterized by XRD, FESEM, and EDAX to study the structural properties, surface morphology, and elemental composition analysis, respectively. The thickness of the fabricated films was measured using the Taylor-Hobson (Taly-step UK) system.

2.2.1 X-Ray Diffraction

On a Rigaku diffractometer (DMAX-500), an X-ray diffractometer with CuKα radiation and wavelength (λ) = 0.154059 nm, XRD patterns of fabricated thin films were observed. The samples were examined between the range of 10° to 80°. The 2θ values obtained were compared to data files from the Joint Committee on Powder Diffraction Standards (JCPDS). Origin 9.5 software was used to calculate the full width of half maxima (FWHM). Debye Scherer's formula, Eq. 1, was used to determine the crystallite size [21].

$$D = \frac{K\lambda}{\beta Cos\theta} \tag{1}$$

Where,

D= Crystallite size,

K= Scherrer constant (0.9),

β = Full width of half maxima (FWHM),

λ =wavelength of X source (0.154059 nm).

By using Bragg's formula Eq.2, the interplaner spacing was calculated.

$$d = \frac{\lambda}{2Sin\theta} \tag{2}$$

Where, λ = wavelength of X-radiation.

2.2.2 FESEM and EDAX

The surface morphology of the fabricated thin films was characterized using a Field Emission Scanning Electron Microscope (FESEM) [Model JOEL 6300 LA GERMANY]. Image-J software was used to find the average particle size of the fabricated thin films. Energy dispersive X-ray spectrometer (JEOL-2300, Germany) was used to do the elemental analysis.

The specific surface area calculated using FESEM images of fabricated thin films. The following Eq.3, was used to measure the specific surface area of thin films using the BET method for spherical particles [21].

$$S_w = \frac{6}{\rho d} \tag{3}$$

Where,

S*w* - Specific surface area,

d - Diameter of the spherical particles, and

ρ – Composite density.

2.3 Electrical characterization

The half-bridge method was used to determine the DC resistance of the films as a function of temperature. A fixed DC voltage was provided to the circuit and the thick film was series connected with an external load resistor, RL. The output voltage across the RL resistor was measured with a digital multimeter (classic 5175 DM) to determine the film resistance values. A chromel-alumel thermo-couple was used to indicate the operating temperature on a digital temperature indicator system. Equations 4, 5, and 6 were used to compute the resistivity, activation energy, and temperature coefficient of resistance of the fabricated thin films [21, 22].

$$\rho = \left(\frac{R \times b \times t}{l}\right) ohm - m \tag{4}$$

Where,

R= Resistance of the film at room temperature, t = thickness of the film, b = breadth of the film, l = length of the film and ρ = resistivity.

$$\Delta E = \frac{log\, R}{log\ Ro} \times KT \tag{5}$$

Where,

ΔE = Activation energy,

R = Resistance at elevated temperature,

R_0 = Resistance at 0°C.

K = Boltzmann constant and

T = Absolute temperature.

$$TCR = \frac{1}{R_o}\left(\frac{\Delta R}{\Delta T}\right) /^{O} C \tag{6}$$

Where,

ΔR = change in resistance between temperature T_1 and T_2,

ΔT = temperature difference between T_1 and T_2 and

R_o = Resistance of the film at room temperature.

2.4 Gas Sensing Characterization

Gas sensors have essential performance parameters such as sensitivity, selectivity, response and recovery time.

2.4.1 Sensitivity

A static gas sensing system was used to investigate the gas response of fabricated CuO-ZnO heterojunction thin films. For the study of gas response, liquefied petroleum (LPG), ammonia (NH_3), ethanol (C_2H_5OH), and dichlorofluoroethane (R12) reducing gases were used for the study of gas response. To evaluate the gas response in the form of sensitivity, the electrical resistance of thin films in the air (Ra) and the presence of gas (Rg) were measured. The gas response or gas sensitivity was calculated by utilizing Eq. 7. [23]

$$Sensitivity(\%) = \frac{\Delta R}{R_a} \times 100 \tag{7}$$

Where,

Ra - Ra-Rg, Here, Resistance of a thin film in air and

Rg - Resistance of thin film after exposing to target gas.

2.4.2 Selectivity

In a mixed gas environment, a sensor should respond to only one type of gas. The ratio of a gas sensor's reaction to that of another dominant interfering gas in the atmosphere determines its selectivity towards a specific gas. Eq. 8 was used to determine the selectivity of the fabricated CuO-ZnO heterojunction thin films for a particular gas over others.

$$Selectivity\% = \frac{S_{gas}}{S_{target\,gas}} X100 \tag{8}$$

Where,

S_{gas} = sensitivity of interfering gas at an optimum operating temperature and

$S_{target\ gas}$ = sensitivity of the target gas at the same temperature.

2.4.3 Response and recovery time of thin films

Rapid response and recovery are important for optimal operation and consistent results. Since the sensor's effective parameters for working at a certain gas concentration and temperature are response and recovery time.

3. Results and Discussion

3.1 Structural properties

3.1.1 X-Ray Diffraction (XRD)

In Figure 2, the X-ray diffraction pattern for the fabricated CuO-ZnO heterojunction thin film annealed at 650 °C is shown in Figure 2. The hkl parameters of the CuO-ZnO thin film are determined using the JCPDS Card. The XRD peaks match the reported diffraction pattern of CuO with a monoclinic structure (JCPDS card # 80-1917). Similarly, diffraction peaks for ZnO having a hexagonal structure match well with the reported XRD pattern (JCPDS card # 36- 1451). The prominent peak of XRD is to be found at 36.16 degrees and the maximum intensity of (1 0 1) reflections has been observed. The same results were reported by Al Abdullah, Khalaf, et al. [24, 25].

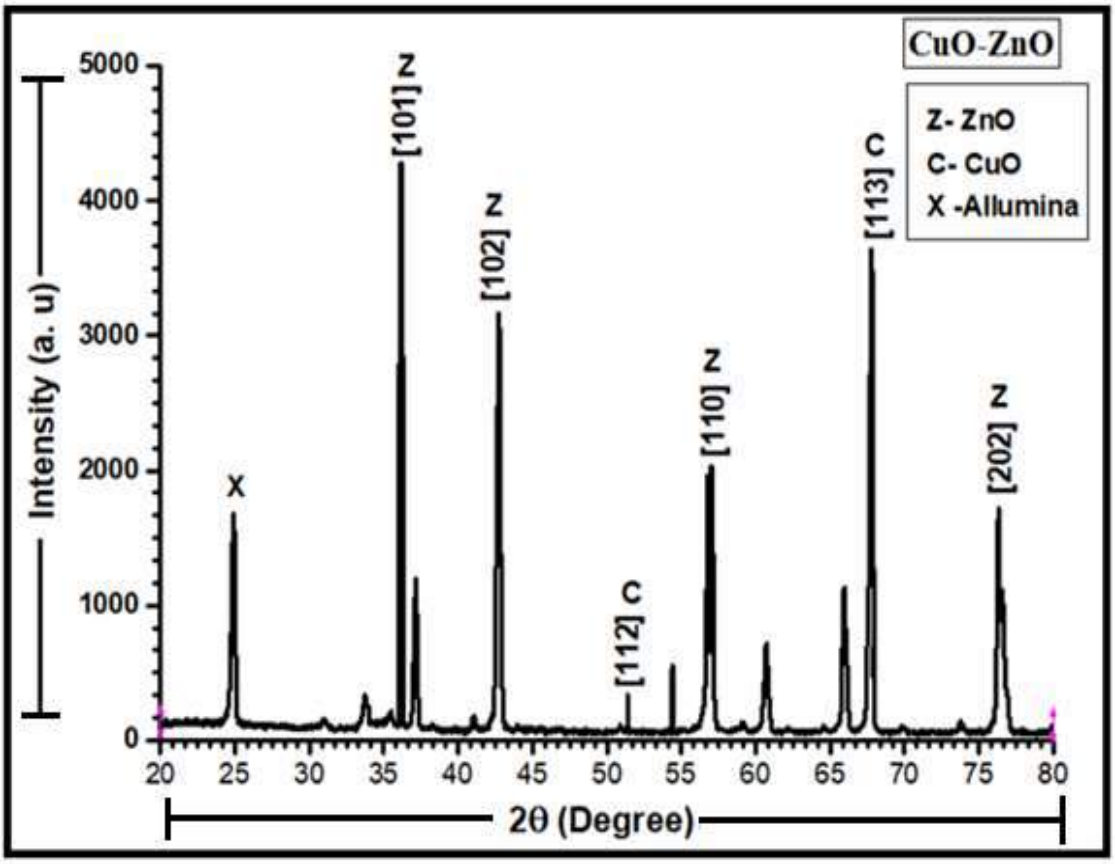

Fig.2 XRD pattern of CuO-ZnO heterojunction thin film

Table 1 Structural outcomes of CuO-ZnO heterojunction thin film

Interplaner spacing (Aº)	Crystallite size (nm)	Degree of crystallinity (%)
2.482079	36.83	88.76

3.1.2 Field Emission Scanning Electron Microscopy (FESEM)

Figure 3 indicates the FESEM micrograph of the fabricated CuO-ZnO thin film. From Figure 3, it is observed that the particle sizes are smaller, and the spherical shape of nanoparticles of deposited material has been found. The presence of tightly packed particles allows the surface morphologies to become more compact and continuous, which may be due to the attraction between the CuO and ZnO nanoparticles. Large agglomerated grains were uniformly distributed and adhered to the substrates well. High porosity, voids, and trapezium-shaped grains are also available in large numbers, and a more effective surface area has been observed for oxygen species adsorption. The large voids and larger surface area improved the gas sensing performance of the films [26, 27].

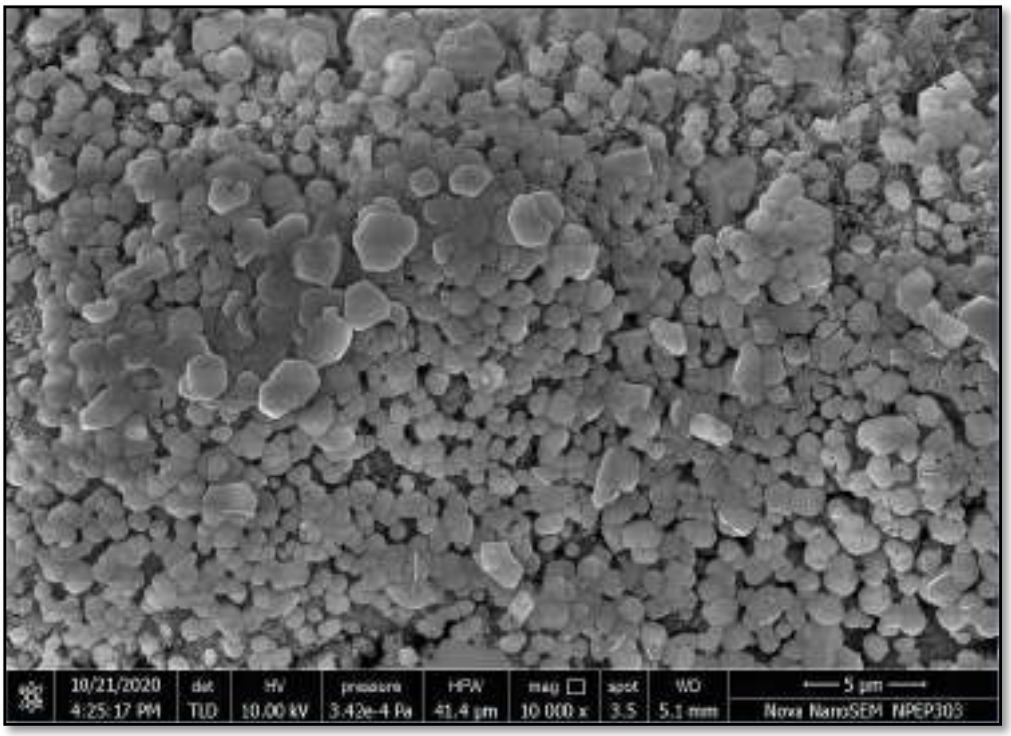

Fig.3 SEM image of CuO-ZnO heterojunction thin films

The catalytic oxidation of a gas molecule is catalysed by the reactive surface of a semiconductor material, which allows for indirect gas detection. CuO-ZnO heterojunctions or nanocomposites have a high surface-to-volume ratio, specific surface area, and increased porosity, which improves catalysis, gas diffusion, and mass transportation in gas-sensing materials. [13, 14]
The average particle size of CuO-ZnO heterojunction thin films was calculated by using image J software. Figure 4 reveals average particle size range of fabricated CuO-ZnO thin films.

Table 2 Outcomes form FESEM

CuO-ZnO Thin Films	Particle size (nm)	Specific Surface Area m^2/g
Annealed at 650 ºC	135	76.406

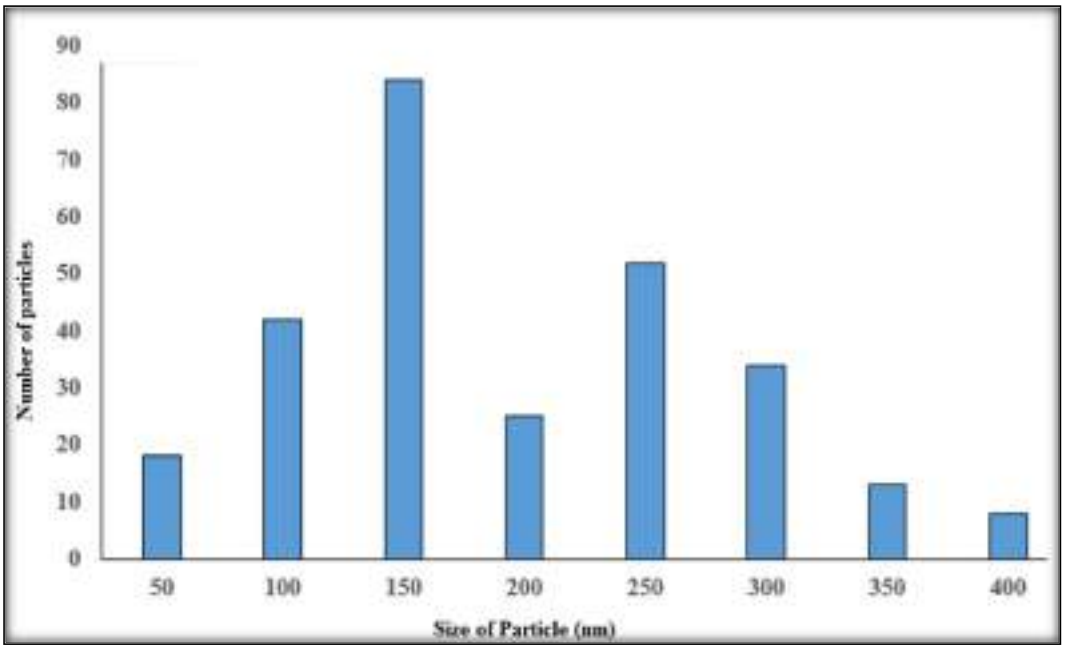

Fig. 4 Particle size distribution

3.1.3 EDAX

Figure 5 reveals the EDAX spectra of fabricated CuO-ZnO thin films. From Figure 4, it is clear that the film shows Zn, Cu, and O according to the EDAX outcomes. The mass percent and atomic weight percent of Zn, Cu, and O are nearly identical. From the EDAX spectra, it is found that atomic weight percentages of Zn, Cu, and O are nonstoichiometric. The atomic and weight percentages of analysis of film elements are tabulated in Table 3.

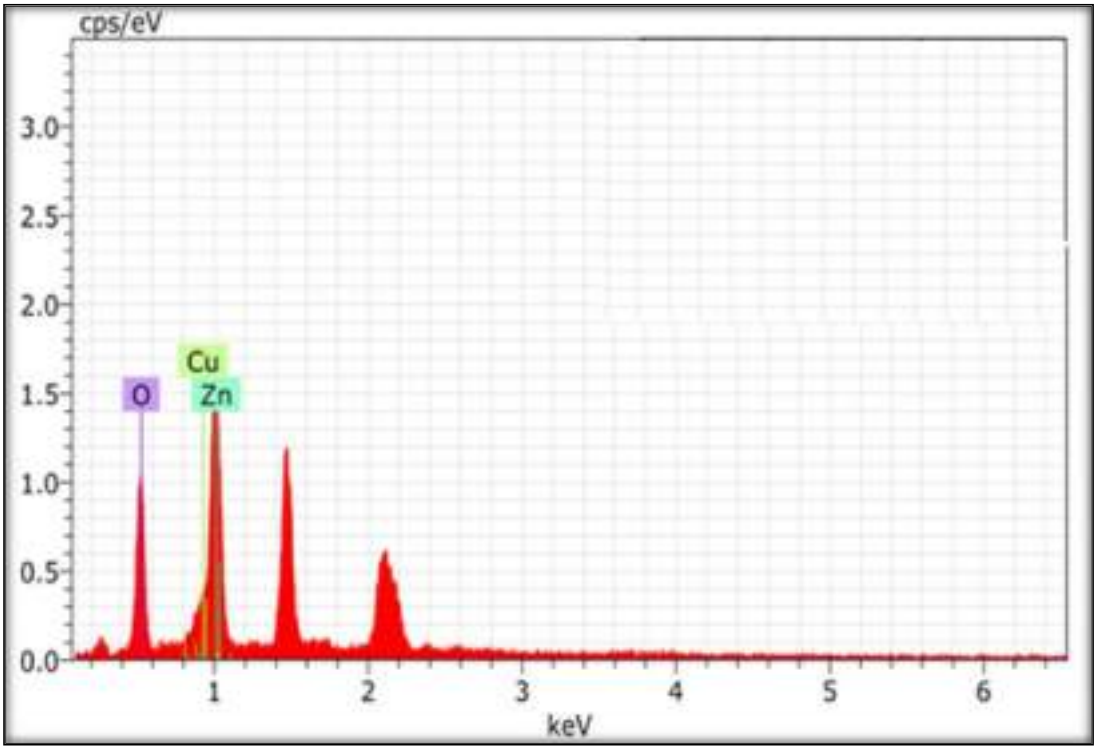

Fig. 5 EDAX of CuO-ZnO heterojunction thin films

Table 3 Elemental Composition of CuO-ZnO heterojunction thin films

Element	At. Wt. %	Mass %
Zn	26.87	55.46
Cu	05.08	10.18
O	68.05	34.36

3.2 Electrical Properties

3.2.1 Resistivity

The resistivity of material plays an important role in gas sensing, because it directly impacts the gas sensing characteristics of films. The resistances of CuO-ZnO heterojunction thin films were plotted against temperature in Figure 6. The resistance of fabricated CuO-ZnO thin films declines as the temperature of the film rises, showing that the films are semiconducting. The decrease in resistance could be produced by an increase in charge carrier drift mobility as temperature rises, or by lattice vibrations as temperature rises, when the atoms are generally close enough for charge carriers to migrate and conduction is induced by lattice vibration [20, 21]. Because oxygen is released in CuO-ZnO thin films, the resistivity of the film decreases with rising temperature [27-29]. The resistivity of fabricated CuO-ZnO thin films was found to be a 23.461 Ω/m.

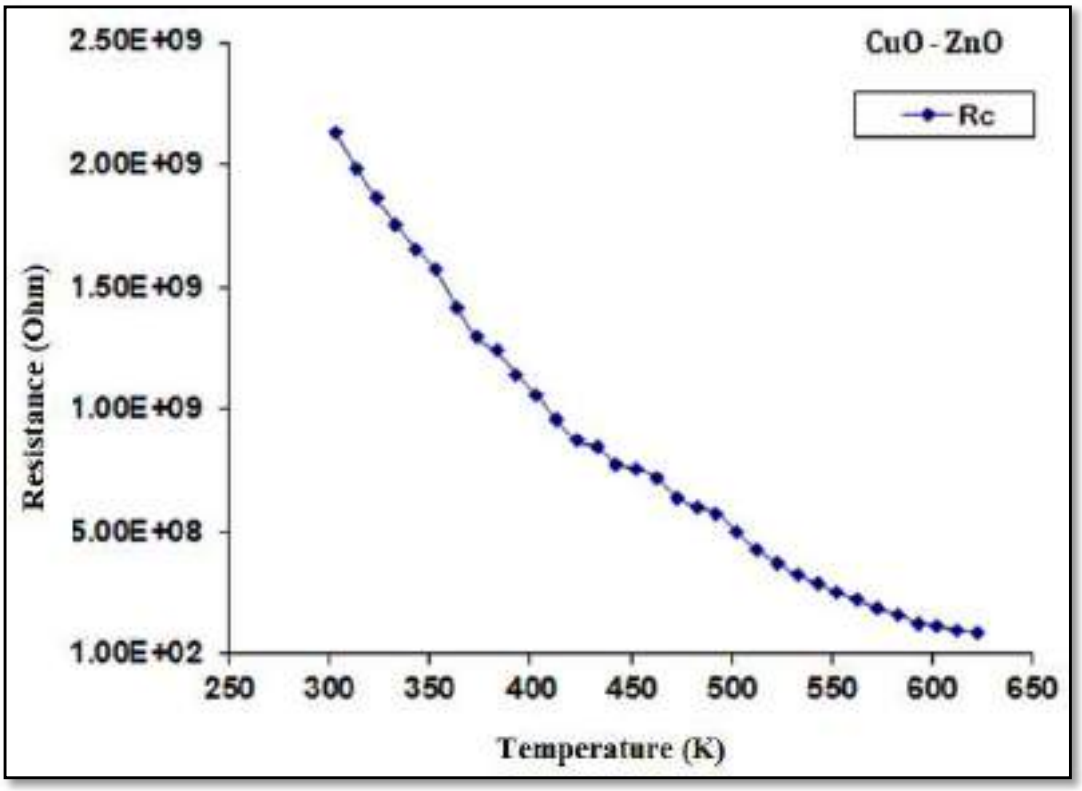

Fig. 6 Resistance versus temperature of CuO-ZnO heterojunction thin films

3.2.2 Activation energy

The activation energy of the fabricated CuO-ZnO heterojunction thin films was calculated using an Arrhenius plot for low and high temperature regions. Figure 7 illustrates the variance of log R versus the reciprocal of temperature (1/T) of the CuO-ZnO thin film. Figure 7 depicts two separate linear regions for fabricated the CuO-ZnO heterojunction thin films, indicating two different activation energies, one for higher temperatures and the other for lower temperature regions. Because material passes from one conduction band to another, the activation energy in the lower temperature region is always lower than the energy in the higher temperature region [27, 29]. From Figure 7, the activation energy for fabricated CuO-ZnO thin film at the low temperature region was found to be 0.10932 eV and at the high temperature region was found to be 0.40032 eV, respectively. The increase in conductivity at low temperatures is related to the mobility of charge carriers, which is determined by the defect concentration that occurred due to doping. As a result, the region of low temperature conduction is often referred to as the conduction mechanism. The activation energy decreases in this region because a modest amount of thermal energy is sufficient to activate the charge carriers and allow them to participate in the conduction process. In other words, defects in the lattice that are loosely linked can simply migrate. As a result, an increase in charge mobility can be attributed to a rise in conductivity in the lower temperature region, the same result reported by Garde, A. S. et al. [29].

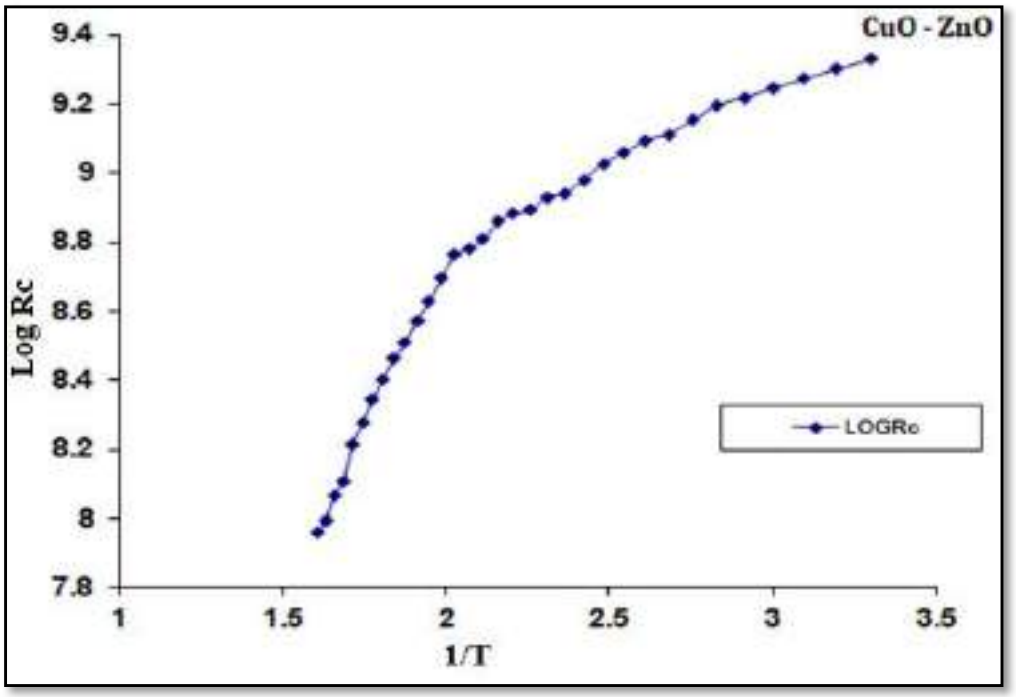

Fig. 7 Arrhenius plot of CuO-ZnO heterojunction thin films

3.2.3 Temperature coefficient of resistance (TCR)

Eq. 4 was used to compute the TCR of a fabricated CuO-ZnO heterojunction thin film. It was found to be -0.004413/°C. The negative sign indicates that the fabricated thin films of CuO-ZnO have semiconducting properties. Table 3 summarizes the electrical results of the CuO-ZnO thin film.

Table 4 Summary of electrical results of fabricated CuO-ZnO heterojunction thin films

Resistivity (Ω/m)	TCR (/°C)	Activation energy (eV)	
		LTR	HTR
23.461	-0.004413	0.10932	0.40032

3.3 Gas sensing properties

The gas-sensing properties of the fabricated CuO-ZnO heterojunction thin films were investigated in this study using a locally developed gas system. The developed system was used to inject the target gases such as dichlorofluoromethane (R12), ammonia (NH_3), ethanol (C_2H_5OH), and liquefied petroleum (LPG) onto the surface of fabricated CuO-ZnO thin films. The fabricated CuO-ZnO thin film has been used as a sensing element. At different working temperatures, the fabricated thin film's resistance was measured in the ambient condition as well as in the presence of gas (at various ppm quantities).

3.3.1 Sensitivity

Eq. 7 was used to investigate the sensitivity of the fabricated CuO-ZnO heterojunction thin film. The results in Fig. 8 reveal the gas sensitivity of a fabricated CuO-ZnO thin film at various temperatures to LPG gas. At a working temperature of 50 °C and a gas concentration of 300 ppm, the fabricated CuO-ZnO thin film exhibited a maximum sensitivity of 89.23% to LPG gas, among other selected reducing gases. The variance in sensitivity to LPG gas was observed to be relatively small above 50°C. As the temperature rises, the sensitivity of CuO-ZnO thin films drops continuously to LPG gas. From Figure 8, it is observed that the fabricated CuO-ZnO thin film shows very little sensitivity to R12 gas. It was also observed that the sensitivity of the fabricated CuO-ZnO thin film varied as the temperature rise for ammonia and ethanol.

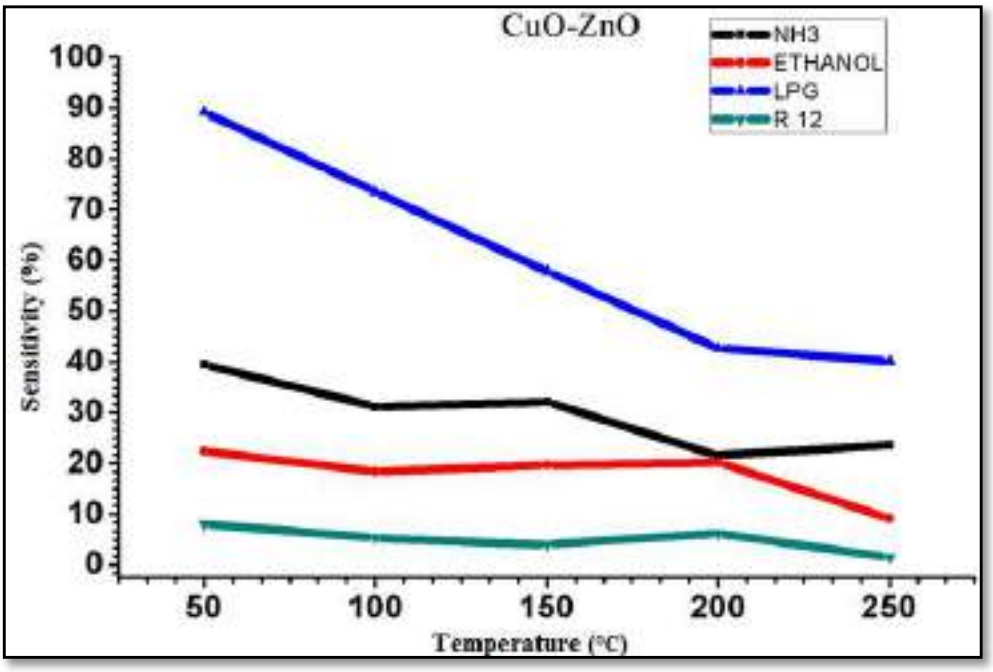

Fig.8 Sensitivity of fabricated CuO-ZnO thin film

3.3.2 Selectivity

The ability of a gas sensor to distinguish between various target gases is a critical feature of a successful gas sensor. An optimum operating temperature was noted in order to measure the selectivity of a sensor for a specific target gas. Selectivity of the fabricated CuO-ZnO thin films was determined by using Eq. 8.

The sensor's sensitivity to the target gas should be higher than that to the other selected gases. Other gases such as NH_3, ethanol, and R12 were also tested on the CuO-ZnO thin film. In our lab, these gases were readily available. Figure 9 shows the selectivity of the fabricated CuO-ZnO thin film for selected reducing gases. At 50°C, LPG gas has the maximum selectivity against all other tested gases, including ethanol, NH_3, and R12.

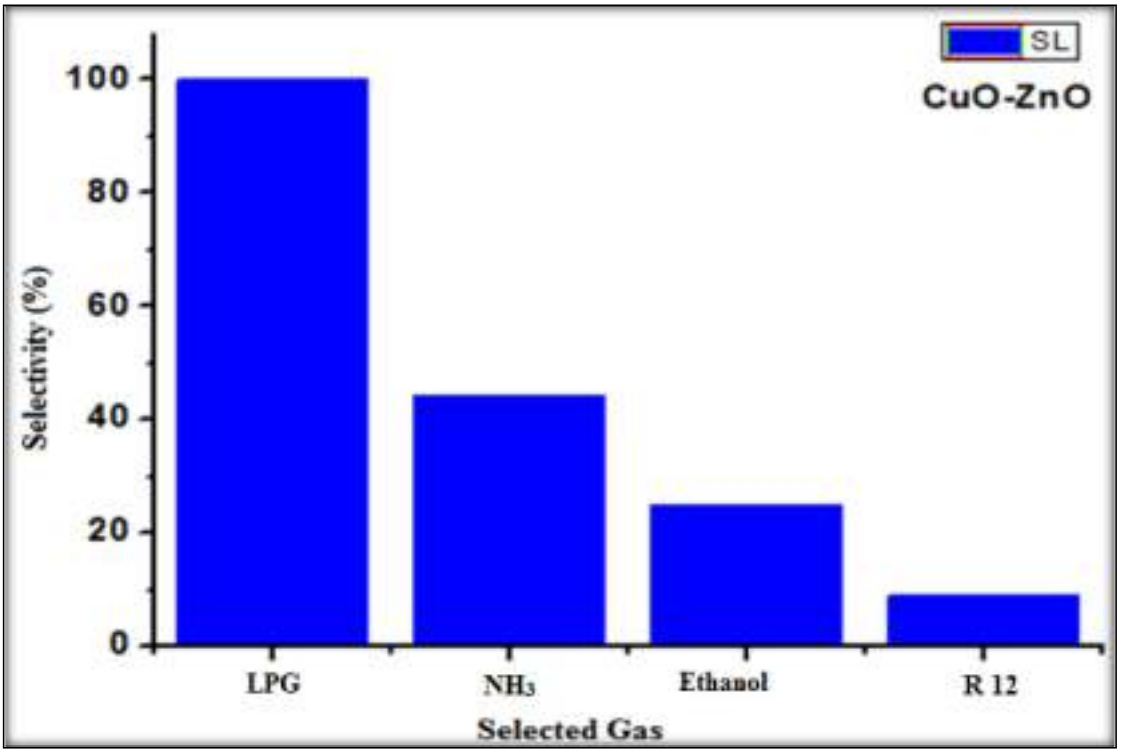

Fig. 9 Selectivity fabricated CuO-ZnO thin film for selected gases at 50°C.

3.3.3 Response and recovery time

The response and recovery time of the fabricated CuO-ZnO thin film are depicted in Figure 10. It has a response time of 9 seconds and a recovery time of 17 seconds to LPG at a concentration of 300 ppm and an optimum temperature of 50 ^{o}C. It's possible that the quick response is due to faster gas oxidation. Its high volatility explains why it reacts quickly and recovers quickly from its initial chemical state. The small amounts of surface reaction products and their high volatility account for the rapid response to LPG and its return to its original chemical state [29, 30].

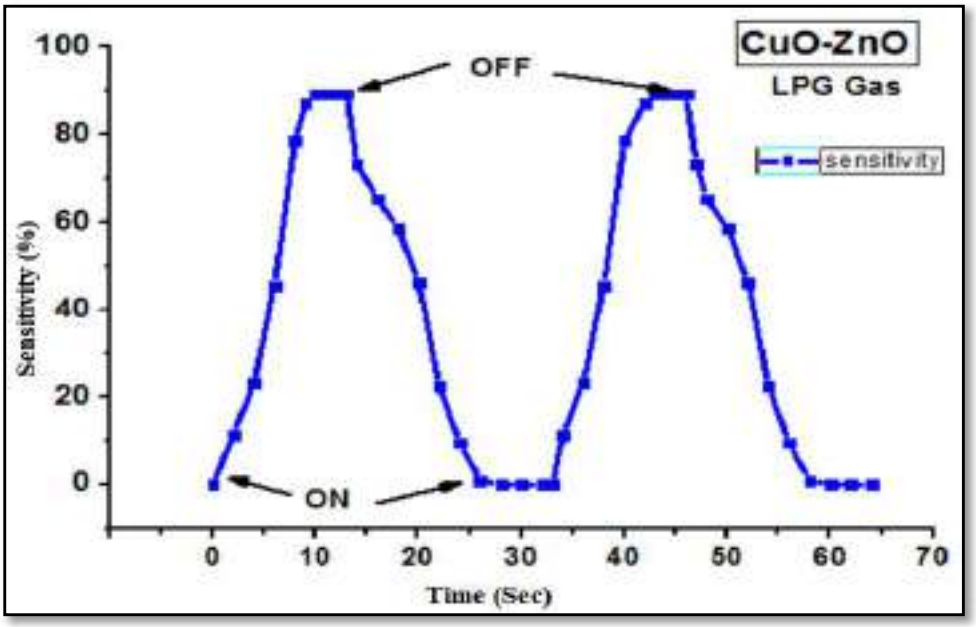

Fig. 10 Response and recovery time of fabricated CuO-ZnO thin film for LPG gas.

3.3.4 LPG gas sensing mechanism for CuO-ZnO heterojunction thin film

LPG is a complex gas composed primarily of methane, propane, butane, and other hydrocarbons. The surface reaction of composite metal oxide semiconductors is used in the sensing part of the sensors. In air, molecular oxygen is chemisorbed as O_2^-, O^-, or O_2^-, depending on the operating temperature [29, 30]. Electron transfer reactions, also known as redox reactions, are the major part of the sensing response. Gas sensing is concerned with oxygen vacancies, which serve as adsorption sites for gas molecules passing through the atmosphere. As the sensor is exposed to LPG, the adsorbed oxygen ions bind with the sensor, forming H_2O and CO_2. Figure 11 depicts a possible LPG sensing mechanism in pictographic form.

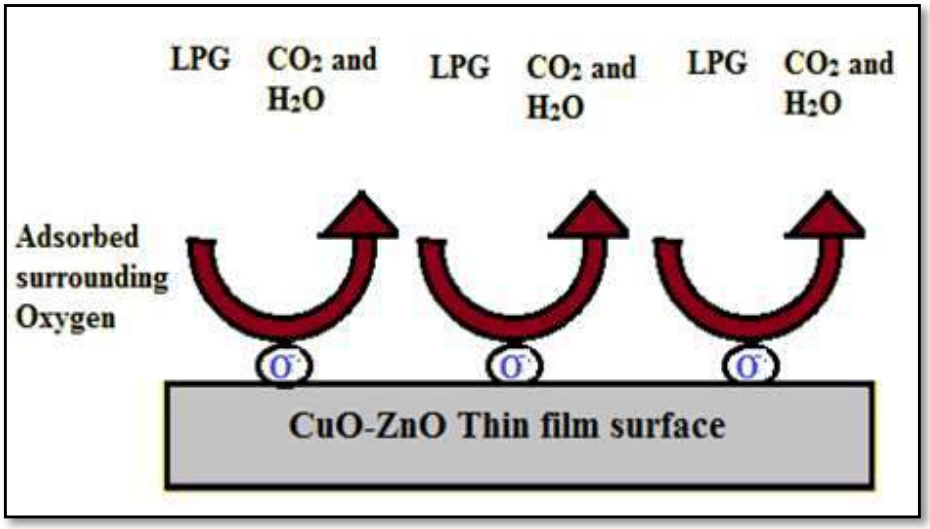

Fig. 11 Schematic of CuO-ZnO LPG gas sensing mechanism

Figure 11 depicts the schematic of the CuO-ZnO LPG gas sensing mechanism. LPG molecules were oxidised with adsorbed oxygen ions, resulting in CO_2 and H_2O. As a result, oxygen evolves into electrically neutral atoms that are trapped behind the negative charges (electrons). The energy released during the decomposition of LPG molecules will be enough to cause trapped electrons to hop into the conduction band of activated ZnO, increasing the film's conductivity. The change in conductivity of the fabricated thin film was recorded as a response to the LPG gas in the form of a change in resistance [30, 31].

3.3.5 Spillover effect in p-n (CuO-ZnO) heterojunctions thin film

CuO, which has a lot of oxygen, has p-type conductivity with holes, while ZnO, which also has a lot of oxygen, has n-type conductivity with electrons. A deep charged depletion layer forms across the grain boundaries of ZnO and CuO in a gaseous environment, resulting in p-n heterojunctions. The electron associated with this charged species was extracted from the bulk material's conduction band, causing the film's resistance to increase. As a result, at the border, a potential barrier emerges, generating a continuous chain of p-n junctions. Figure 12 depicts the band diagram of the heterojunction of p-type (CuO) and n-type (ZnO) semiconductors at equilibrium. The electrons spilled over from the donor CuO to ZnO, where they were caught in the potential well, because of the discontinuity in the conduction band. When a film is exposed to reducing LPG gas, the gas molecules are oxidised by adsorbed oxygen ions (O-, O_2-, and O_2-), resulting in oxygen desorption [32, 33]. The reaction of LPG gas with adsorbed oxygen ions at 50 ^oC, where the film was, exhibits the highest gas response.

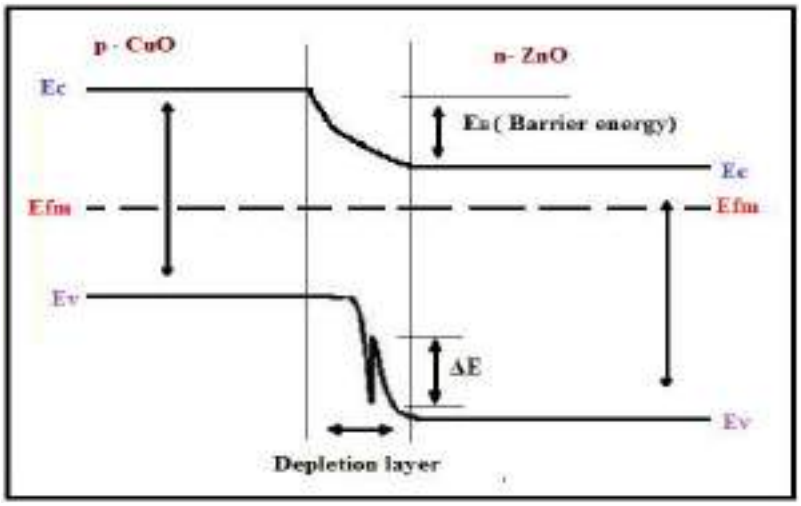

Fig. 12 Energy band diagram of p-n heterojunctions at equilibrium

Conclusion

The CuO-ZnO heterojunction thin film could be fabricated on an alumina substrate using the thermal evaporation technique. High sensitivity to liquefied petroleum gas at low temperature is a prominent property of the fabricated CuO-ZnO thin film. The nanostructured nature of the fabricated CuO-ZnO thin film was validated by the structural characterization. From Joint Committee on Powder Diffraction Standards data, the structure of ZnO is a hexagonal wurtzite phase and crystalline structure, and CuO is a monoclinic structure. By using Scherer's formula, the crystallite size of CuO-ZnO heterojunction thin films was found to be 36.83 nm. The Field emission scanning electron microscopy micrograph shows high porosity, voids, and trapezium-shaped grains as well as small particle size. The specific surface area found to be 76.406 m^2/g. Energy dispersive X-ray analysis of the fabricated thin film showed the presence of Zn, Cu, and O as the only detected elements. The elemental analysis reveals that films are nonstoichiometric. At a working temperature of 50 °C and a gas concentration of 300 ppm, the fabricated CuO-ZnO heterojunction thin film exhibits the highest sensitivity to liquefied petroleum gas. Response and recovery times are also found to be quick in seconds.

Acknowledgment

The authors are grateful to the Department of Physics and Research Center, N.H. College, Bramhapuri, Dist. Gadchiroli, India for providing laboratory facilities. The author also thanks the Department of Physics at Savitribai Phule Pune University, Pune for providing the facilities for SEM, EDAX, and XRD characterization for current research work. The author also thanks the Department of Electronic Science and Research Center, LVH College, Nashik, Maharashtra, India, for providing the required laboratory facilities.

References

[1] Yamazoe N, toward innovations of gas sensor technology. Sensors and Actuators B: Chemical 108, no. 1-2 (2005): 2-14.

[2] Kim, J.H, Low-voltage-driven sensors based on ZnO nanowires for room-temperature detection of NO_2 and CO gases. ACS applied materials & interfaces 11, no. 27 (2019): 24172-24183.

[3] Patil S. J, Semiconductor metal oxide compounds based gas sensors: A literature review. Frontiers of Materials Science 9, no. 1 (2015): 14-37.

[4] Dey, Ananya. Semiconductor metal oxide gas sensors: A review. Materials Science and Engineering: B 229 (2018): 206-217.

[5] Xue, S, Improving Gas-Sensing Performance Based on MOS Nanomaterials: A Review. Materials 14, no. 15 (2021): 4263.

[6] Kumar R, ZnO nanostructured thin films: Depositions, properties and applications—A review. Materials Express 5, no. 1 (2015): 3-23.

[7] Hwang, Dae-Kue, Min-Suk Oh, Jae-Hong Lim, and Seong-Ju Park. ZnO thin films and light-emitting diodes. Journal of Physics D: Applied Physics 40, no. 22 (2007): R387.

[8] Abdel-Karim, R., Y. Reda, and A. Abdel-Fattah. Nanostructured materials-based nanosensors. Journal of the Electrochemical Society 167, no. 3 (2020): 037554.

[9] Eranna, G., B. C. Joshi, D. P. Runthala, and R. P. Gupta. Oxide materials for development of integrated gas sensors—a comprehensive review. Critical Reviews in Solid State and Materials Sciences 29, no. 3-4 (2004): 111-188.

[10] Anukunprasert, T., C. Saiwan, and Enrico Traversa. The development of gas sensor for carbon monoxide monitoring using nanostructure of Nb–TiO_2. Science and Technology of Advanced Materials 6, no. 3-4 (2005): 359-363.

[11] Bochenkov, V. E., and G. B. Sergeev. Sensitivity, selectivity, and stability of gas-sensitive metal-oxide nanostructures. Metal oxide nanostructures and their applications 3 (2010): 31-52.

[12] Park, Sunghoon, Soohyun Kim, Hyejoon Kheel, Soong Keun Hyun, Changhyun Jin, and Chongmu Lee. Enhanced H_2S gas sensing performance of networked CuO-ZnO composite nanoparticle sensor. Materials Research Bulletin 82 (2016): 130-135.

[13] Das, Susmita, and Vimal Chandra Srivastava. An overview of the synthesis of CuO-ZnO nanocomposite for environmental and other applications. Nanotechnology Reviews 7, no. 3 (2018): 267-282.

[14] Nakamura, Yoshinobu, Hiroyuki Yoshioka, Msaru Miyayama, Hiroaki Yanagida, Tsuyoshi Tsurutani, and Yuji Nakamura. Selective CO gas sensing mechanism with CuO/ZnO heterocontact. Journal of the Electrochemical Society 137, no. 3 (1990): 940.

[15] Baptista, Andresa, F. J. G. Silva, J. Porteiro, J. L. Míguez, G. Pinto, and L. Fernandes. On the physical vapour deposition (PVD): Evolution of magnetron sputtering processes for industrial applications. Procedia Manufacturing 17 (2018): 746-757.

[16] Shahidi, Sheila, Bahareh Moazzenchi, and Mahmood Ghoranneviss. A review-application of physical vapor deposition (PVD) and related methods in the textile industry. The European Physical Journal Applied Physics 71, no. 3 (2015): 31302.

[17] Ponzoni, Andrea, Camilla Baratto, Nicola Cattabiani, Matteo Falasconi, Vardan Galstyan, Estefania Nunez-Carmona, Federica Rigoni, Veronica Sberveglieri, Giulia Zambotti, and Dario Zappa. Metal oxide gas sensors, a survey of selectivity issues addressed at the SENSOR Lab, Brescia (Italy). Sensors 17, no. 4 (2017): 714.

[18] Tsay C.Y., Cheng H.C., Tung Y.T., Tuan W.H., and Lin C.K., Effect of Sn-doped on microstructural and optical properties of ZnO thin films deposited by sol-gel method, Thin Solid Films, 2008, 517 (3): 1032.

[19] Sertel, Buse Comert, Nihan Akin Sonmez, Meltem Donmez Kaya, and Suleyman Ozcelik. Development of MgO: TiO_2 thin films for gas sensor applications. Ceramics International 45, no. 3 (2019): 2917-2921.

[20] Yatskiv, R., Tiagulskyi, S., Grym, J., Vaniš, J., Bašinová, N., Horak, P., Torrisi, A., Ceccio, G., Vacik, J. and Vrňata, M., (2020). Optical and electrical characterization of CuO/ZnO heterojunctions. Thin Solid Films, 693, p.137656.

[21] Tupe, Umesh Jagannath, M. S. Zambare, Arun Vitthal Patil, and Prashant Bhimrao Koli. The Binary Oxide NiO-CuO Nanocomposite Based Thick Film Sensor for the Acute Detection of Hydrogen Sulphide Gas Vapours. Material Science Research India 17, no. 3 (2020): 260-269.

[22] Halwar, Dharma K., Vikas V. Deshmane, and Arun V. Patil. Orthorhombic molybdenum trioxide micro-planks as carbon monoxide gas sensor. Materials Research Express 6, no. 10 (2019): 105913.

[23] Ahire, Satish Arvind, Arun V. Patil, Ashwini A. Bachhav, Prashant Bhimrao Koli, and Thansing B. Pawar. Designing of Screen-Printed Stannous Oxide Thick Film Sensors Modified by Cobalt and Nitrogen for Sensing Some Toxic Gases and Volatile Organic Compounds. Available at SSRN 3894844 (2021).

[24] Vallejo, William, Alvaro Cantillo, Briggitte Salazar, Carlos Diaz-Uribe, Wilkendry Ramos, Eduard Romero, and Mikel Hurtado. Comparative Study of ZnO Thin Films Doped with Transition Metals (Cu and Co) for Methylene Blue Photodegradation under Visible Irradiation. Catalysts 10, no. 5 (2020): 528.

[25] Al Abdullah, Khalaf, et al. Synthesis of ZnO nanopowders by using sol-gel and studying their structural and electrical properties at different temperature. Energy Procedia 119 (2017): 565-570.

[26] Nagaraju, P., Y. Vijayakumar, MV Ramana Reddy, and U. P. Deshpande. Effect of vanadium pentoxide concentration in ZnO/V_2O_5 nanostructured composite thin films for toluene detection. RSC advances 9, no. 29 (2019): 16515-16524.

[27] Patil, Arun, Chandrakant Dighavkar, Ratan Borse, Shriram Patil, and Rajendra Khadayate. Effect of Cr_2O_3 by Doping and Dipping On Gas Sensing Characteristics of ZnO Thick Films. Journal of Electron Devices 15 (2012): 1274-1281.

[28] Muchharla, Baleeswaraiah, T. N. Narayanan, Kaushik Balakrishnan, Pulickel M. Ajayan, and Saikat Talapatra. Temperature dependent electrical transport of disordered reduced graphene oxide. 2D Materials 1, no. 1 (2014): 011008.

[29] Garde, A. S. LPG and NH_3 Sensing Properties of SnO_2 Thick Film Resistors Prepared by Screen Printing Techniqu. Sensors & Transducers 122, no. 11 (2010): 128.

[30] Deore, M. K., V. B. Gaikwad, R. M. Chaudhari, N. U. Patil, P. D. Hire, S. B. Deshmukh, G. E. Patil, V. G. Wagh, and G. H. Jain. Formulation, characterization and LPG-sensing properties of CuO-doped ZnO thick film resistor. In Advancement in Sensing Technology, pp. 283-298. Springer, Berlin, Heidelberg, 2013.

[31] Nemade, K. R., and S. A. Waghuley. LPG sensing performance of CuO–Ag_2O bimetallic oxide nanoparticles. St. Petersburg Polytechnical University Journal: Physics and Mathematics 1, no. 3 (2015): 249-255.

[32] Deore, Madhavrao K., Vishwas B. Gaikwad, and Gotan H. Jain. Role of CuO-ZnO Heterojunctions in Gas Sensing Response of CuO-ZnO Thick Films. Journal of Physical Science and Application 6, no. 2 (2016): 51-60.

[33] Liu, Jinhuai, Xingjiu Huang, Gang Ye, Wei Liu, Zheng Jiao, Wnaglian Chao, Zhongbai Zhou, and Zenglian Yu. H_2S detection sensing characteristic of CuO/SnO_2 sensor. Sensors 3, no. 5 (2003): 110-118.

Iranian Journal of Materials Science and Engineering, Vol. 19, Number 4, December 2022
RESEARCH PAPER

Influence of Annealing Temperature on Structural and Electrical Properties of Screen Printed Lanthanum Oxide Thick Films

Sonali Laxman Wagh[1,*], Umesh Jagannath Tupe[2], Anil Bhimrao Patil[1], Arun Vitthal Patil[3]

* *sonalilwagh@gmail.com*

[1] Department of Electronic Science and Research Center, Loknete Vyankatrao Hiray Arts, Science and Commerce College, Panchavati, Nashik, Affiliated to SPPU, Pune, Maharashtra, 422003, India
[2] Department of Electronics, Vidya-Amrut Dnyan Pratishtan's, Arts, Science & Commerce College, Shirsondi, Affiliated to SPPU, Pune, Tal: - Malegaon Dist: - Nashik, Affiliated to SPPU, Maharashtra– 423208, India
[3] Department of Physics, MGV's, Arts, Science and Commerce College, Manmad, Dist. Nashik, Affiliated to SPPU, Pune, Maharashtra - 423104, India

Received: June 2022 **Revised: November 2022** **Accepted: December 2022**
DOI: 10.22068/ijmse.2716

Abstract: *Temperature is one of the key factor that affecting the electrical, physical, structural, and morphological properties as well as the crystallinity of the nanomaterials. The current study investigates the effect of annealing temperature on the structural and electrical properties of lanthanum oxide (La_2O_3) thick films. La_2O_3 thick films were prepared on a glass substrate using a conventional screen printing technique. In this work, T1 is an unannealed prepared film, whereas T2 and T3 are annealed in a muffle furnace for 3 hours at 350°C and 450°C, respectively. XRD technique was exploited to investigate the crystallization behavior of the films. It was found that the crystal structure of La_2O_3 thick films are pure hexagonal phase. The annealing temperatures were revealed to have influence on the crystallite sizes of the films. SEM and EDS was used to study the morphology and elemental analysis of the films respectively. The electrical properties of the films were explored by measuring resistivity, temperature coefficient of resistivity (TCR), and activation energy at lower and higher temperatures regions. The film annealed at 450°C has high resistivity, a high TCR, and small crystallite size. The thickness of the La_2O_3 thick films was also found to decrease as the annealing temperature increased.*

Keywords: *Lanthanum oxide, annealed, glass substrate, activation energy, structural, electrical properties.*

Graphical Abstract:

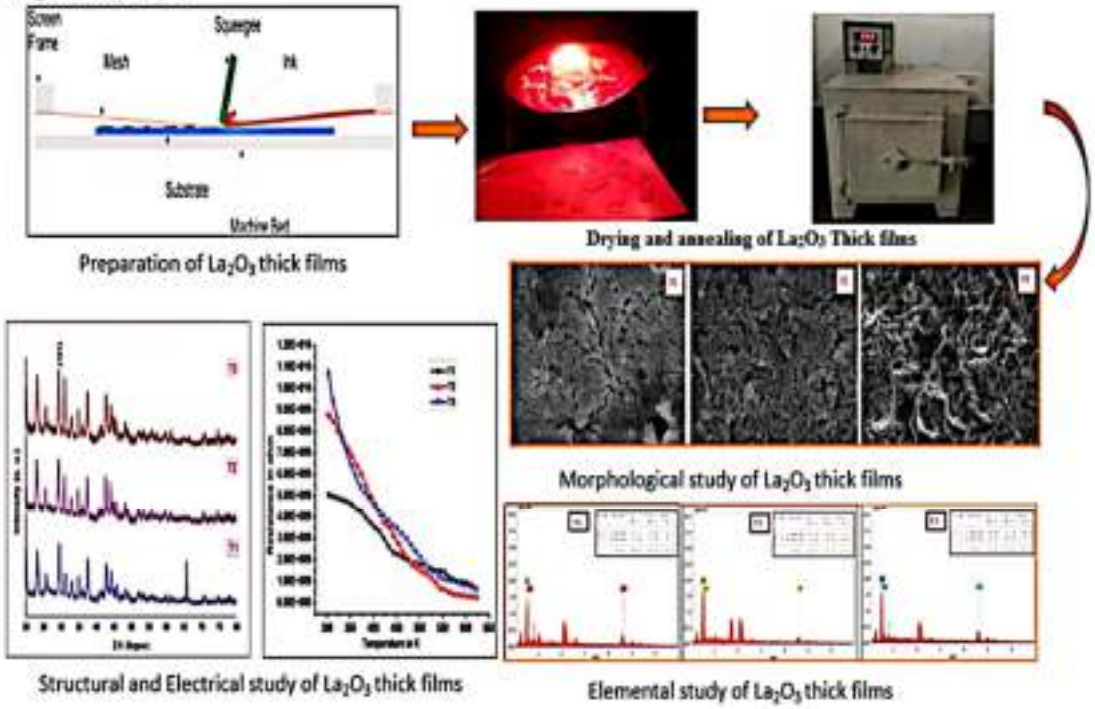

1. INTRODUCTION

Lanthanum oxide (La_2O_3) is one of the most promising material in advanced metal-oxide semiconductor technology. La_2O_3 is an appealing functional rare earth oxide compound that has increasingly piqued the interest of researchers in recent years [1, 2]. Recent research has revealed that La_2O_3, as a p-type semiconductor oxide, has unique chemical, thermodynamic, physical, electrical and chemical properties, making it a suitable candidate for use in many areas. By combining the valences La_3^+/La_2^+, La_2O_3 can use to store energy [3, 4].

La_2O_3 is a colourless, odourless substance. It is not soluble in water, although it is soluble in dilute acid. Lanthanum oxide nanoparticles have very high photoelectric conversion efficiency. La_2O_3 is a low-cost basic material with a wide spectrum of organic reactions. La_2O_3 is a non-toxic substance that is used in a wide range of applications such as gas sensors, catalysts, supercapacitors, batteries, optoelectronics, luminescence, and biomedicine [5, 6].

various variety of approaches were used to synthesis of La_2O_3 nanoparticles like sol-gel, spray pyrolysis, solvothermal, thermal decomposition, precipitation, co-precipitation, hydrothermal, Chemical Bath Deposition, Reflux method, Solution combustion, microemulsion method, chemical vapour deposition, sputtering, thermal oxidation, and combustion methods. High crystallisation degree, pure phase, and variable particle size of nano powders or nanoparticles can be obtained using these approaches [6-9].

Annealing is a typical technique for improving thin film adhesion and performance, with its benefits attributed to changes in the nature of the interface and segregant diffusion. By modifying yield qualities, it also impacts plasticity in the process zone [10]. Annealing is the process of atoms or charges restructuring in a material throughout time after irradiation. Although high temperatures may be required to achieve these results, some annealing effects can be achieved at ambient temperature over extended periods of time [11].

Sen B. et. al (2007) reported effect of annealing temperature on thin films using sol gel method. The cell dimensions and unit cell volume continued to shrink as the annealing temperature increased. Furthermore, as the annealing temperatures were raised, the difference between the unit cells of films was found to decrease. This could be owing to a strong ionic interaction between the unit cell's sub-lattice ions when the oxygen stoichiometry and/or oxygen concentration increase with higher annealing temperatures. Increasing the annealing temperature also increases film density and decreases lattice and volume defects, reducing internal stress in the film and reducing cell dimensions [12, 13].

In the field of gas sensor the electrical parameters like resistivity, temperature coefficient of resistivity (TCR), and activation energy are very important. The gas response of the films are depends on these parameters. As well as the structural parameters including morphological, specific surface area, grain size, crystallite size, dislocation density and crystallinity of the nanomaterials also plays a vital role for gas sensing mechanism. Hence the current research work focus on the study of influence or impact of annealing temperature on the structural and electrical properties of La_2O_3 thick films prepared by conventional screen printing technique.

2. EXPERIMENTAL WORK

2.1. Preparation of La_2O_3 Thick Films by Standard Screen-Printing Technique

In this experiment work, commercially available AR grade (99.99% purity) Lanthanum oxide nano powder was used. On a clean glass substrate, all La_2O_3 films were prepared. All glass substrates were thoroughly cleaned with double distilled water and acetone and exposed to an IR lamp for 30 minutes to remove contaminants. Pure thick films of La_2O_3 were prepared using a mixture of 70% inorganic and 30% organic materials. Inorganic materials included commercially available La_2O_3 nano powder while organic materials included ethyl cellulose and butyl carbitol acetate (BCA). The La_2O_3 powder and ethyl cellulose were combined and mixed together in a mortar and pestle then adding BCA drop by drop to make a thixotropic paste. To prepare thick films, this paste was uniformly applied to a glass substrate through a screen printing technique. The thick films were prepared and exposed to IR radiation for 45-50 minutes to eliminate any residual impurities and local binder.

After that some prepared thick films were annealed at 350°C and 450°C in a muffle furnace for 3 hours and then used future study.

The prepared thick films unannealed and annealed at 350, and 400°C temperatures are labelled as T1, T2 and T3 respectively in all further discussions.

2.2. Structural Characterization

The standard tools like XRD, FESEM, and EDS were used to study the structural characteristics, surface morphology, and elemental composition of the prepared La_2O_3 thick films, respectively. The mass difference method was used to determine the thickness of the prepared thick films [14]. The prepared films thickness was found to be in the μm range.

2.2.1. X-Ray Diffraction

XRD patterns of La_2O_3 thick films were recorded on Rigaku diffractometer (DMAX-500), X-ray diffractometer with CuKα radiation and wavelength λ= 1.54059 A°. The samples were scanned for 2θ ranges from 10° to 80°. The obtained values of 2θ were compared with Joint Committee on Powder Diffraction Standards (JCPDS) data files. Full width of half maxima was calculated using origin 9 software. The crystallite size (D) was calculated by Debye Scherer's formula [14] that is Eq. 1.

Rigaku diffractometer (DMAX-500), X-ray diffractometer with CuKα radiation and wavelength λ= 1.54059 A°, was used to record XRD patterns of prepared La_2O_3 thick films. The films were examined for two different ranges ranging from 10° to 80°. The obtained 2θ values were compared to standard data files from the Joint Committee on Powder Diffraction Standards (JCPDS). Origin 9.5 software was used to compute the full width of half maxima of obtained prominent peak in XRD plot. Debye Scherer's formula, Eq. 1, was used to calculate the crystallite size (D).

$$D = \frac{K\lambda}{\beta \cos\theta} \quad (1)$$

Where, K= Scherrer constant (0.9), β= Full width of half maxima (FWHM),

λ =wavelength of X source (1.540598 A°)

2.2.2. FESEM and EDAX

The surface morphology of the prepared thick films was characterized using Field Emission Scanning Electron Microscopy (FESEM) [Model JOEL 6300 LA GERMANY]. Using Image-J software, the spherical size particle diameter of La_2O_3 thick film was calculated. An energy dispersive X-ray spectrometer (EDAX) [JOEL-2300, Germany] was used to conduct the elemental composition of prepared films. FESEM images and the Brunauer-Emmett-Teller (BET) method were used to calculate the surface area of unannealed and annealed films [14].

2.3. Electrical Characterization

The half bridge method was used to determine the DC resistance of the films as a function of temperature. A constant DC voltage was provided to the circuit and the thick film was connected in series with an external load resistor RL. The output voltage across the RL resistor was measured with a digital multimeter (classic 5175 DM, 0.5) to determine the film resistance values. A chromel-alumel thermo-couple was used to indicate the operating temperature on a digital temperature display device. Equations 2, 3, and 4 were used to compute the resistivity, temperature coefficient of resistance and activation energy at lower and higher temperature region of the prepared La_2O_3 thick films [14, 15].

$$p = \left(\frac{R \times b \times t}{l}\right) \text{ohm} - \text{m} \quad (2)$$

Where,

R= Resistance of the film at room temperature, t= thickness of the film,

b= breadth of the film, *l*= length of the film.

$$TCR = \frac{1}{R_0}\frac{\Delta R}{\Delta T} /°C \quad (3)$$

Where,

ΔR= change in resistance between temperature T_1 and T_2,

ΔT= temperature difference between T_1 and T_2 and

R_0= Resistance of the film at room temperature.

$$\Delta E = \frac{\log R}{\log R_0} \times KT \quad (4)$$

Where,

ΔE= Activation energy, R= Resistance at elevated temperature, R_0= Resistance at 0°C.

3. RESULT AND DISCUSSION

3.1. Structural properties

3.1.1. X-Ray Diffraction (XRD)

The XRD analysis was performed to determine the crystal structure of the prepared thick films. The X-ray diffraction patterns of La_2O_3 are depicted in Fig. 1. T1 is an unannealed prepared film, whereas T2 and T3 indicate annealed

prepared films at 350°C and 450°C, respectively. The overall crystal structure of La_2O_3 thick films is revealed by XRD patterns. By using 2θ value the prominent peak was found at 29.58°, 29.34° and 29.44° to T1, T2 and T3 samples respectively as shown in Fig. 1. The crystal structure was found to be pure hexagonal phase for lanthanum oxide and the diffraction peak observed at (101) reflection plane. These results were match with standard JCPDS card No. 83-1348 [7]. The strong, and sharp diffraction peaks confirmed crystallinity of La_2O_3. The nanostructures of La_2O_3 are indicated by the broader nature of the XRD peaks. From the XRD pattern of T2 and T3 it is found the height and the FWHM value of prominent peak is decreased and decreased respectively as shown in table 1. As compare to JCPDS card No. 83-1348 the prominent peaks are shifted due to annealing.

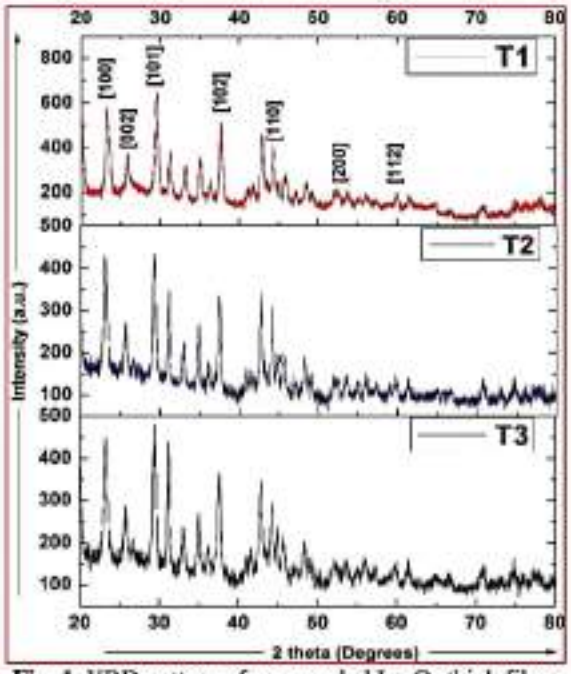

Fig. 1. XRD pattern of unannealed La_2O_3 thick films (T1), XRD pattern of La_2O_3 thick films annealed at 350°C (T2), XRD pattern of La_2O_3 thick films annealed at 450°C (T3)

By using Debye-Scherrer formula equation 1, the crystalline size of T1, T2 and T3 was determined 20.11 nm, 22.53 nm and 19.51 nm respectively. It is also found that the as annealing temperature increases the crystalline size increased for T2 and decreased for T3 samples. The small crystallite size (D) influence the specific surface area of the film. As crystallite size reduces the specific surface area increases, which is important to gas sensing properties of the films.

3.1.2. Field Emission Scanning Electron Microscopy (FESEM)

Surface properties of materials are frequently examined using FESEM magnification at 10K. Surface features such as homogenous, heterogeneous, porosity, and voids can be visualised by SEM investigation of the materials [14].

FESEM micrographs of unannealed and annealed La_2O_3 thick films are shown in Fig. 2. Field emission scanning electron microscopy was used to characterize the microstructure. The samples T1 and T2 shows microstructure is fairly homogeneous, with small open porosity, according to FESEM micrographs. There was, nevertheless, considerable residual intragranular porosity to sample T1. It was observed that as the annealing temperature was raised, the grain size and crystalline quality changes. The atoms can be shifted to more energetically favorable places such as voids, grain boundaries, and interstitial locations as a result of annealing. As the temperature rises, the crystallinity improves, increasing the mobility of atoms at the of films surface [15, 16]. The sample T3 shows good adhesion and more porosity as compare to T1 and T2 samples, it may be the annealing temperature of sample T3 is more as compare to T1 and T2 samples.

3.1.3. Energy Dispersive X-ray Spectrometer (EDAX)

The elemental composition of the films unannealed and annealed at 350°C and 450°C is shown in Table 2. From Fig. 3, both lanthanum and oxygen peaks can be seen in the EDAX spectra, with no impurities in all samples.

Table 1. XRD parameters of La_2O_3 thick films

Sample	2 Theta (Degree)	FWHM	Max. Intensity (A.U)	Crystallite Size (nm)
T1	29.58	0.427	648	20.11
T2	29.34	0.381	434	22.53
T3	29.44	0.440	480	19.51

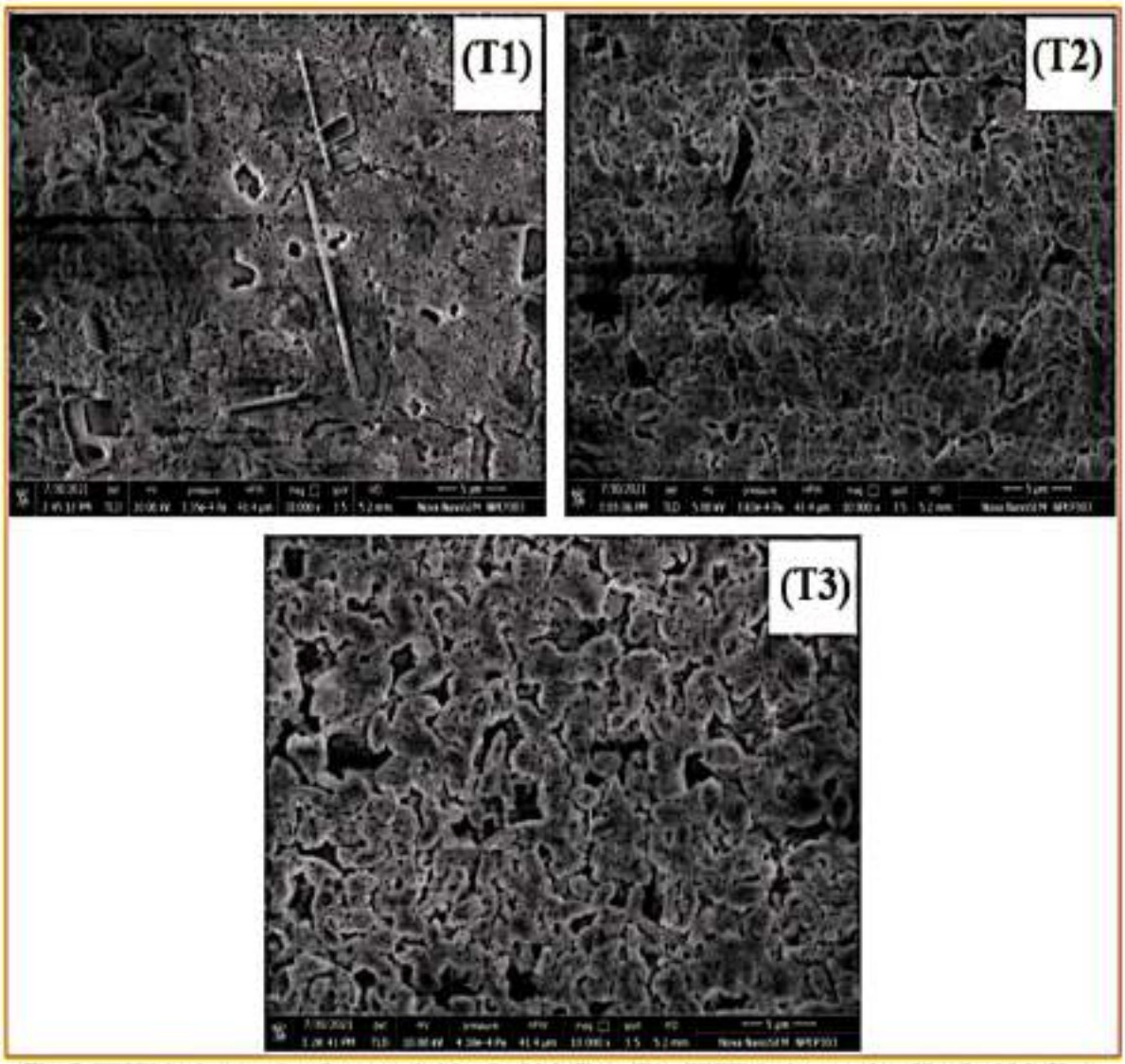

Fig. 2. FESEM micrographs of unannealed La_2O_3 thick films (T1), FESEM micrographs of La_2O_3 thick films annealed at 350°C (T2), FESEM micrographs of La_2O_3 thick films annealed at 450°C (T3)

Due to the release of extra oxygen, the mass percentage of oxygen in the T3 sample decreased as the annealing temperature was increased. According to the results, La_2O_3 thick films are non-stoichiometric [15, 17].

4. ELECTRICAL PROPERTIES

4.1. Resistivity

Fig. 4 depicts the resistance of prepared La_2O_3 thick films samples in air as a function of temperature for T1, T2 and T3 samples. Resistance decreases as temperature rises, showing semiconducting behaviour.

Any increase in the temperature of a thick film leads electrons to gain enough energy to overcome the grain boundary barrier. Because oxygen adsorbates are desorbed from the surface of the films at higher temperatures, the potential barrier at grain boundries may be reduced. The carrier concentration rises at higher temperatures due to intrinsic thermal excitation, and the electron transport process enhances as the temperature rises.

The thick film's resistance decreases as temperature rises, which could be owing to increased charge carrier drift mobility or increased lattice vibrations, in which the atoms periodically come close enough for charge carrier transfer and conduction is generated by lattice vibration [15-18].

Table 2. Composition of La_2O_3 thick films

Sample	Element	At. Wt. %	Mass %
T1	La	23.21	72.40
	O	76.79	27.60
T2	La	13.07	56.62
	O	86.93	43.38
T3	La	24.44	73.74
	O	75.56	26.26

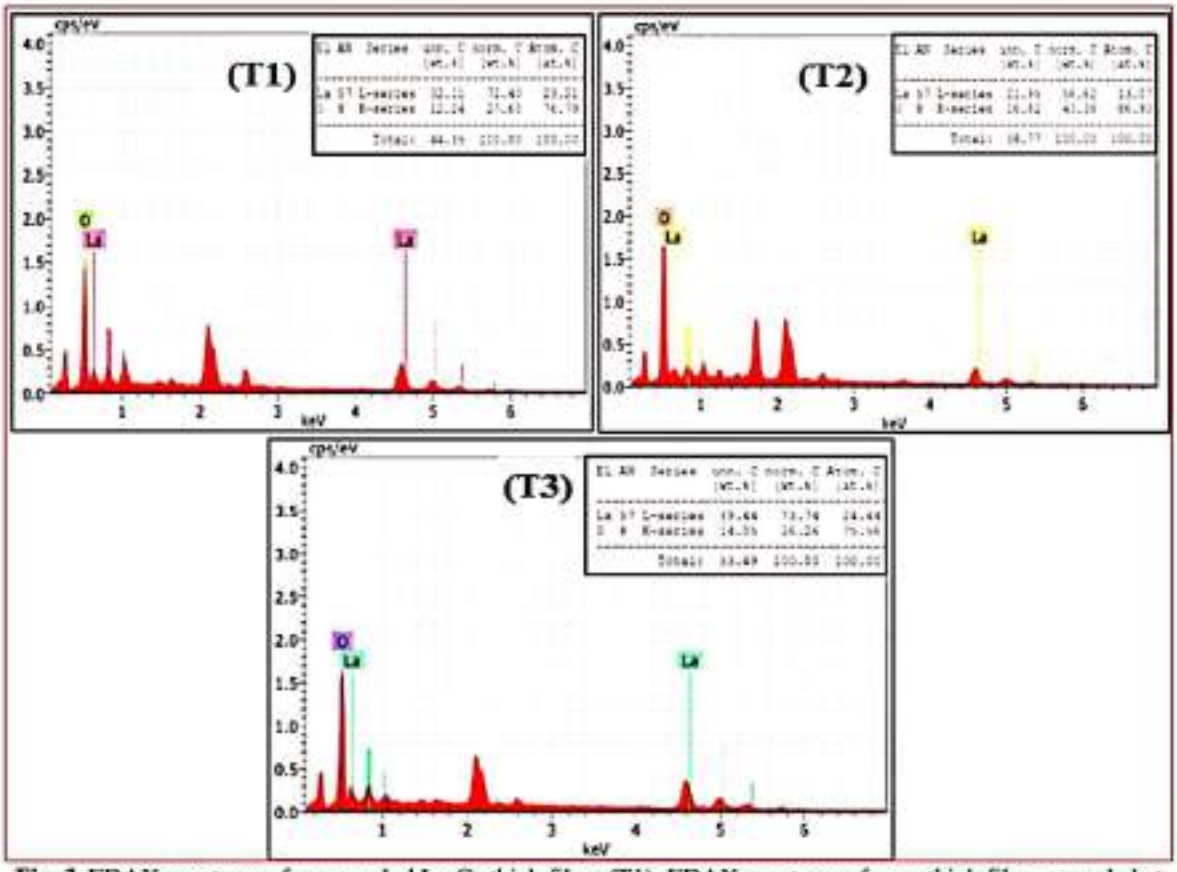

Fig. 3. EDAX spectrum of unannealed La_2O_3 thick films (T1), EDAX spectrum of La_2O_3 thick films annealed at 350 °C (T2), EDAX spectrum of La_2O_3 thick films annealed at 450 °C (T3).

From Fig. 4, it is also observed that the resistance of prepared La_2O_3 thick films samples reduces rapidly from ambient temperature to a particular temperature range, whereas the resistance drops slowly at higher temperatures. Due to the graph's exponential structure, the resistance attain a constant lowest saturation level with respect to temperature. Equation 2 is used to calculate the resistivity of prepared La_2O_3 thick film samples at constant temperature. The resistivity of T1, T2 and T3 samples was found to be 65971.69 Ω-m, 96948.83 Ω-m and 1101690.72 Ω-m respectively. It is also found that the as annealing temperature increases the resistivity of prepared La_2O_3 thick film samples increased. The gas sensors constructed using metal oxide semiconductors (MOS) in which resistance as well as resistivity is a key parameter because the sensing behaviour/principle of MOS sensor depends on the change in resistance with nature of gas (oxidizing or reducing).

4.1.1. Temperature Coefficient of Resistance (TCR)

The influence of temperature on resistance was examined in order to compute the TCR, which was calculated using Equation 3. TCR of prepared La_2O_3 thick film was negative for all samples, indicating that the thick films were

semiconducting nature. The variation of TCR with prepared La_2O_3 thick film samples is shown in Fig. 5. TCR is found to be negative, and its value dropped to T2 sample and raised to T3 sample as the annealing temperature was increased. TCR increased gradually with increasing annealing temperature in the T3 sample, indicating an electron emission mechanism that expanded exponentially with increasing annealing temperature [15, 20]. The TCR of T1, T2 and T3 samples was found to be -0.0049678/°C, -0.0054271/°C and -0.0036719/°C respectively.

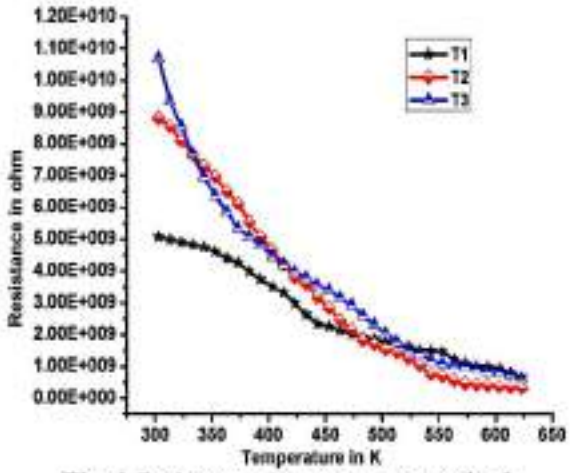

Fig. 4. Resistance v/s temperature graph of unannealed La_2O_3 thick films (T1), Resistance v/s temperature graph of La2O3 thick films annealed at 350°C (T2), Resistance v/s temperature graph of La2O3 thick films annealed at 450°C (T3)

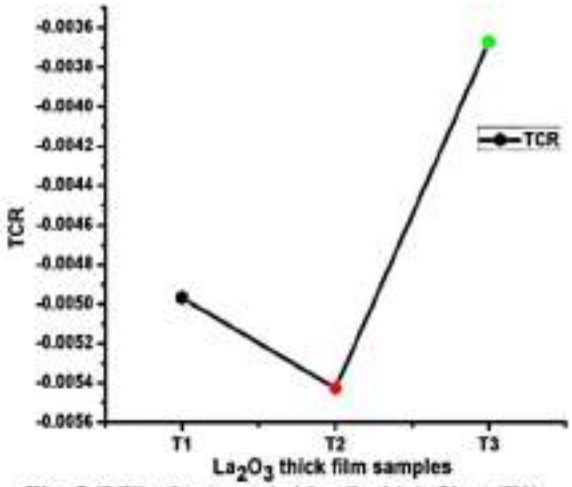

Fig. 5. TCR of unannealed La_2O_3 thick films (T1), TCR of La_2O_3 thick films annealed at 350°C (T2), TCR of La_2O_3 thick films annealed at 450°C (T3)

4.1.2. Activation Energy

The Arrhenius plot of Log Rs v/s 1/T for prepared La_2O_3 thick film samples is shown in Fig. 6. Because material passes from one conduction mechanism to another, the activation energy in the low temperature region is always lower than the energy in the high temperature region. The rise in conductivity in the low-temperature region is due to the mobility of charge carriers, which is dependent on the defects concentration. As a result, the region of low temperature conduction is commonly referred to as the conduction mechanism. Because low thermal energies are adequate for the activation of charge carriers to participate in the conduction process, activation energy reduces in this range. In other words, imperfections in the lattice that are loosely attached can simply transfer. As a result, an increase in conductivity at lower temperatures can be attributed to a rise in charge mobility.

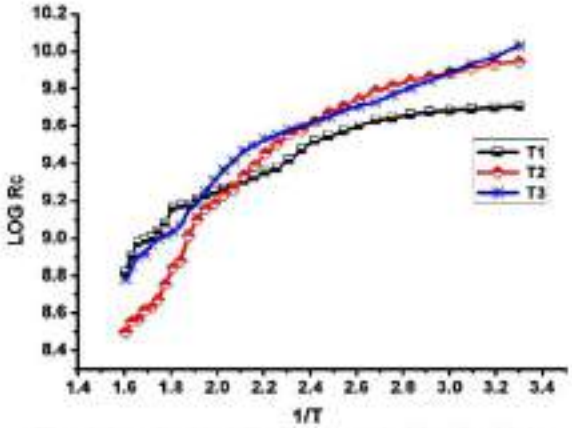

Fig. 6. Log Rc Vs 1/T of unannealed La_2O_3 thick films (T1), Log Rc Vs 1/T of La2O3 thick films annealed at 350°C (T2), Log Rc Vs 1/T of La_2O_3 thick films annealed at 450°C (T3)

The activation energy in a high-temperature region is larger than in a low-temperature region [15, 16]. The electrical conductivity in this region is mostly determined by intrinsic imperfections; hence it is referred to as intrinsic conduction. The high activation energy values in this region can be driven by the fact that the energy necessary to generate the imperfections is significantly more than that required to drift it. As a result, only at high temperatures the intrinsic imperfections generated by thermal fluctuations impact the electrical conductivity of the films [15, 18, 20]. Equation 4 is used to calculate the action energy

at higher and lower regions of prepared La_2O_3 thick film samples. The action energy at higher region of T1, T2 and T3 samples was found to be 0.160346 eV, 0.772415 eV and 0.26699 eV respectively and the action energy at lower region of T1, T2 and T3 samples was found to be 0.00846831 eV, 0.123552 eV and 0.097387 eV respectively.

Table 3 summarizes the influence of annealing on the electrical properties of prepared La_2O_3 thick films.

5. CONCLUSIONS

La_2O_3 thick films could be prepared using screen printing technique on a glass substrate. The crystal structure of La_2O_3 thick films was found to be pure hexagonal phase, according to XRD analysis. The voids between the particles were found using FESEM micrographs to be caused by the evaporation of the organic solvent during the annealing of the prepared films. The films annealed at 450°C (sample T3) are found to have a high resistivity, a high TCR, and a small crystallite size. The thickness of the La_2O_3 thick films was also found to decrease as the annealing temperature increased. The obtained results are helpful in the field of gas sensor.

The impact of annealing temperature on prepared thick films were studied. According to obtained results few important points were observed those listed are below-

The annealing temperature increased-

1. From XRD, the size of crystallite (D) decreased.
2. The resistivity of the La_2O_3 thick films decreased.
3. The TCR of the La_2O_3 thick films increased.
4. The thickness of the La_2O_3 thick films decreased.
5. From FESEM, the morphology of La_2O_3 thick films changes (more porosity/voids was found)

ACKNOWLEDGMENT

The authors thank to Head, Department of Electronic Science and Research Center, L. V. H. College, Nashik, Maharashtra, India, for providing laboratory facilities.

The authors also acknowledge and pay sincere thanks to Head, Department of Physics, S. P. Pune University, Pune and B. R. Gholap College, Pune, India for providing the laboratory facilities for SEM, EDAX and XRD characterization for present research work.

This research received no specific grant from any funding agency.

The authors have no conflicts of interest to disclose.

REFERENCES:

[1] Goh KH, Haseeb AS, Wong YH. Lanthanide rare earth oxide thin film as an alternative gate oxide. Materials Science in Semiconductor Processing. 2017 Sep 1; 68:302-15.

[2] Yang C, Fan H, Qiu S, Xi Y, Fu Y. Microstructure and dielectric properties of La_2O_3 films prepared by ion beam assistant electron-beam evaporation. Journal of Non-Crystalline Solids. 2009 Jan 1; 355(1):33-7.

[3] Miranda E, Molina J, Kim Y, Iwai H. Tunneling in sub -5 nm La_2O_3 films deposited by E-beam evaporation. Journal of non-crystalline solids. 2006 Jan 1; 352(1):92-7.

[4] Yang C, Fan H, Qiu S, Xi Y, Fu Y. Microstructure and dielectric properties of La2O3 films prepared by ion beam assistant electron-beam evaporation. Journal of Non-Crystalline Solids. 2009 Jan 1; 355(1):33-7.

[5] Vignolo MF, Duhalde S, Bormioli M, Quintana G, Cervera M, Tocho J. Structural and electrical properties of lanthanum oxide thin films deposited by laser ablation. Applied surface science. 2002 Sep 30; 197:522-6.

[6] Dabhane, H., Ghotekar, S., Tambade, P. and Medhane, V., 2020. Plant mediated green synthesis of lanthanum oxide (La2O3) nanoparticles: A review. Asian Journal of Nanosciences and Materials, 3(4):291-299.

[7] Kabir H, Nandyala SH, Rahman MM, Kabir MA, Stamboulis A. Influence of calcination on the sol–gel synthesis of lanthanum oxide nanoparticles. Applied Physics A. 2018 Dec; 124(12):1-1.

Table 3. Summary of thickness, resistivity, activation energy and TCR of prepared La_2O_3 thick films

Sample	Thickness of film (µm)	Resistivity (Ω-m)	TCR (/°C)	Activation energy (eV)	
				HTR	LTR
T1	26	65971.69	-0.0049678	0.160346	0.084683
T2	22	96948.83	-0.0054271	0.772415	0.123552
T3	19	1101690.72	-0.0036719	0.266991	0.097387

[8] Nejad SJ, Abolghasemi H, Moosavian MA, Golzary A, Maragheh MG. Fractional factorial design for the optimization of hydrothermal synthesis of lanthanum oxide nanoparticles under supercritical water condition. The Journal of Supercritical Fluids. 2010 Apr 1; 52(3):292-7.

[9] Sheng J, Zhang S, Lv S, Sun W. Surfactant-assisted synthesis and characterization of lanthanum oxide nanostructures. Journal of materials science. 2007 Dec; 42(23):9565-71.

[10] Koli PB, Kapadnis KH, Deshpande UG, Tupe UJ, Shinde SG, Ingale RS. Fabrication of thin film sensors by spin coating using sol-gel $LaCrO_3$ Perovskite material modified with transition metals for sensing environmental pollutants, greenhouse gases and relative humidity. Environmental Challenges. 2021 Apr 1; 3:100043.

[11] Shinde VS, Kapadnis KH, Sawant CP, Koli PB, Patil RP. Screen print fabricated In3+ decorated perovskite lanthanum chromium oxide ($LaCrO_3$) thick film sensors for selective detection of volatile petrol vapors. Journal of Inorganic and Organometallic Polymers and Materials. 2020 Dec; 30 (12):5118-32.

[12] Sen B, Wong H, Molina J, Iwai H, Ng JA, Kakushima K, Sarkar CK. Trapping characteristics of lanthanum oxide gate dielectric film explored from temperature dependent current–voltage and capacitance–voltage measurements. Solid-state electronics. 2007 Mar 1; 51 (3):475-80.

[13] Salinas, D., Sepúlveda, C., Escalona, N., Gfierro, J.L. and Pecchi, G., 2018. Sol–gel La_2O_3–ZrO_2 mixed oxide catalysts for biodiesel production. Journal of energy chemistry, 27(2): 565-572.

[14] Singh RD, Koli PB, Jagdale BS, Patil AV. Effect of firing temperature on structural and electrical parameters of synthesized CeO_2 thick films. SN Applied Sciences. 2019 Apr; 1 (4):1-9.

[15] Adole VA, Pawar TB, Koli PB, Jagdale BS. Exploration of catalytic performance of nano-La_2O_3 as an efficient catalyst for dihydropyrimidinone/thione synthesis and gas sensing. Journal of Nanostructure in Chemistry. 2019 Mar; 9(1):61-76.

[16] Dighavkar CG, Patil AV, Patil SJ, Borse RY. Influence of Firing Temperature on Compositional and Structural Properties of TiO_2 Thick Films. Invertis Journal of Science & Technology. 2010; 3 (3):184-93.

[17] Mangla O, Srivastava A, Malhotra Y, Ostrikov K. Lanthanum oxide nanostructured films synthesized using hot dense and extremely non-equilibrium plasma for nanoelectronic device applications. Journal of Materials Science. 2014 Feb; 49(4):1594-605.

[18] Koli PB, Kapadnis KH, Deshpande UG, Tupe UJ, Shinde SG, Ingale RS. Fabrication of thin film sensors by spin coating using sol-gel $LaCrO_3$ Perovskite material modified with transition metals for sensing environmental pollutants, greenhouse gases and relative humidity. Environmental Challenges. 2021 Apr 1; 3:100043.

[19] Yang Z, Kumar A. The impacts of thermal pretreatments on biomass gasification and pyrolysis processes. InBiomass Preprocessing and Pretreatments for Production of Biofuels 2018 Jul 26 (pp. 292-324). CRC Press.

[20] Tupe UJ, Zambare MS, Patil AV, Koli PB. The Binary Oxide NiO-CuO Nanocomposite Based Thick Film Sensor for the Acute Detection of Hydrogen Sulphide Gas Vapours. Material Science Research India. 2020; 17(3):260-9.

Chemical Physics Letters 796 (2022) 139555

Contents lists available at ScienceDirect

Chemical Physics Letters

journal homepage: www.elsevier.com/locate/cplett

Synthesis techniques and applications of rare earth metal oxides semiconductors: A review

Amol S. Patil [a], Arun V. Patil [b], Chandrakant G. Dighavkar [c], Vishnu A. Adole [d], Umesh J. Tupe [e,*]

[a] Department of Electronics, SSR College, Silvassa 396230, India
[b] Department of Physics, MGV's, Arts, Science and Commerce College, Manmad, Dist. Nashik 423104, India
[c] Departmet of Physics, MGV's, Arts, Science and Commerce College, Surgana, Dist. Nashik 422211, India
[d] Department of Chemistry, MGV's, Loknete Vyankatrao Hiray Arts, Science and Commerce College, Panchavati, Dist. Nashik 422003, India
[e] Department of Electronics, Vidya-Amrut Dnyan Pratishtan's Arts, Science and Commerce College, Shirsondi, Dist. Nashik 423208, India

ARTICLE INFO

Keywords:
Rare earth metal oxides
Lanthanide series
Yttrium Oxide
Semiconductors
High-tech industries

ABSTRACT

Rare earth elements have seen a rise in demand in recent years due to their distinctive properties and diverse applications. Rare earth-based nanomaterials can be synthesized using techniques such as hydrothermal, solvothermal, electrode position, and atomic layer deposition methods. REMOSs nanoparticles have found use in trace gas sensors, batteries, magnetic storage devices, photovoltaic cells, catalysts, energy conversion, engineering, medicines, food, agriculture, cosmetics, textiles, and antennas. This review elaborates the various synthetic pathways, applications and future prospects of rare earth metal oxides.

1. Introduction

Rare earth elements (REEs) are the lanthanide series of the periodic table, which includes atomic numbers 57 to 71 and contains lanthanum (La) to lutetium (Lu) along with scandium (Sc), and yttrium (Y). Promethium (Pm) is a radioactive and extremely rare element of the lanthanide family. Nuclear transformations are the most common source of promethium (Pm). The difference between the unpaired and paired electrons in the 4f shell divides rare-earth into light rare earth elements (LREE) and heavy rare earth elements (HREE). Rare earth elements are divided into two categories: heavy rare earth elements and light rare earth elements. The heavy rare earth elements include europium, gadolinium, terbium, dysprosium, holmium, erbium, thulium, ytterbium, lutetium, and yttrium. The light rare earth elements include lanthanum, cerium, praseodymium, neodymium, promethium, and samarium as shown in Fig. 1.

REE's global situation, from their applications in high-tech products to their occurrence in diverse types of economic deposits on land and in the water, their behaviour in various geological systems, state-of-the-art chemical characterization techniques, and recycling. Other topics, such as their usage in agriculture and medicine, as well as their environmental implications, REMOSs are very important in technologies like television, wind turbines, LED light bulbs, and cell phones. REE and their alloys have seen a surge in use in a variety of technological devices in the last three decades, including computer memory, DVDs, rechargeable batteries, autocatalytic converters, super magnets, mobile phones, LED lighting, superconductors, glass additives, fluorescent materials, phosphate binding agents, solar panels, and MRI agents. These elements are crucial components in all high-tech devices. For example, Nd is widely used in super magnets for disc drives, Ce is an important component of autocatalysts, and all REE are used in flat-panel televisions. Several REE compounds may be found in smart-batteries, which are used to power all electric and hybrid vehicles. These elements contribute to various technical advantages, such as lower energy consumption, higher efficiency, downsizing, speed, durability, and thermal stability, due to their unique physical, chemical, magnetic, and luminous properties. Their demand has risen in recent years, especially for energy saving gadgets (green technology) that are faster, lighter, smaller, and more efficient. These technologies are also assisting in the reduction of the size and efficiency of analytical instruments [1].

Environmental consequences such as radioactive potential, acidification, eutrophication, solid waste creation, water use, gross primary energy footprint, toxicity, and any other regional or global impact should all be considered. The majority of REEs, on the other hand, are likely to be utilised in energy conservation, efficiency, and renewable energy technologies. Rare earths with large volumes, low reserves, and significant dispersion are the rare earths most at risk. Rare earth elements are essentially concentrated at extremely low levels in the ground

* Corresponding author.
E-mail address: umeshtupe14@gmail.com (U.J. Tupe).

https://doi.org/10.1016/j.cplett.2022.139555
Received 25 November 2021; Received in revised form 28 February 2022; Accepted 11 March 2022
Available online 15 March 2022
0009-2614/

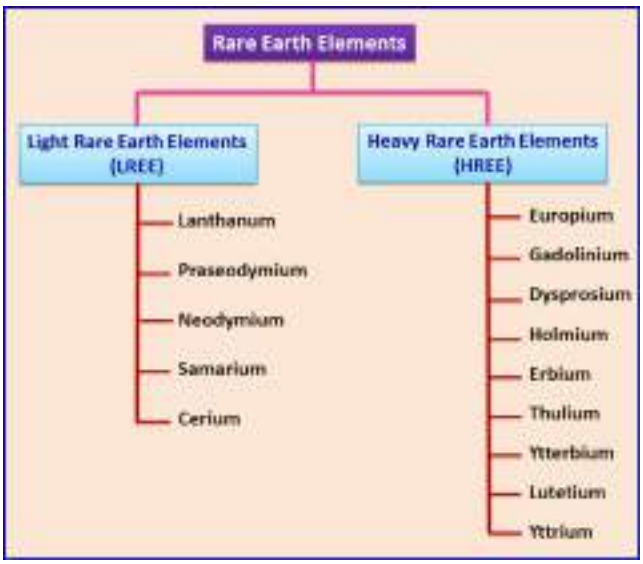

Fig. 1. Classification of rare earth elements.

and then disseminated in small amounts into various devices. As a result, unless the materials are retrieved, they are more likely to be lost when the equipment is disposed of. Rare earth recycling and recovery is difficult because it takes a lot of energy to collect, reprocess, and make new products that can be used to replace the parent metals at the right price [2].

The Engineering Demonstration System (EDS) experiments only use rare-earth elements from the lanthanide class that are not radioactive. Many rare-earth elements are found in greater abundance in the earth's crust than conventional commercial elements. Thus, the earth's crust has more yttrium, cerium, lanthanum, and neodymium than lead [1,2]. Carl Axel Arrhenius discovered rare earth elements in Sweden in 1787 when he discovered ytterbite, a black stone containing yttrium. All 15 lanthanides, as well as yttrium and scandium, were classified as rare earth elements by the 1920 s. Rare earth elements are a set of 17 chemical elements that are present in the earth's crust and are therefore rare. The lanthanides, as well as scandium and yttrium, make up this group of elements [2].

The physicochemical properties of all rare-earth elements are similar, making separation challenging in the past. Their atomic structure determines their common properties. Each outer electron has two, while the next inner shell has eight or nine electrons. Many physical and chemical properties are unchanged when electrons are added to the inner shells. Rare earth metals are all soft and malleable, with a striking silver shine. When metal powders are finely split and exposed to the air, they oxidise quickly. The metal will not spontaneously burn when present in solid lumps but will oxidise slowly, similar to how other metals rust [3,4]. Rare earth metals and compounds are in high demand, and their chemical, catalytic, electromagnetic, magnetic, and optical properties are vital in a wide range of applications. Metallurgy, petrochemicals, fabrics, and agriculture are just a few of the classic industries that use rare earth. In several high-tech industries, such as hybrid automobiles, wind turbines, compact fluorescent lamps, flat-screen televisions, cell phones, hard disks, and defence technologies, they are also becoming increasingly essential. Rare earth elements are used a lot because they have high transition numbers, which cover a wide range of wavelengths from near-ultraviolet to infrared [4,5].

Yttrium is a significant rare earth element, and ensuring a supply for future generations is necessary. Because of the strong similarities in the outer electronic layers between yttrium and lanthanides, yttrium oxide is classified as a rare earth oxide. It has a high melting point (2450 °C), a high free energy formation, good dielectric properties, and good optical properties, including a high refractive index. These materials' physical and mechanical properties can be dramatically altered by varying their composition or introducing imperfections. One thing is certain: yttrium will never be found in nature as a free element. On the Ellingham chart, yttrium oxide has a free energy of formation of 1817 kJ/mole, which is exceptionally low. Yttrium can be found in bastnasite, monazite, xenotime, and ion-absorption clays. It can also be found in uranium ores, samarskite, and fergusonite, but yttrium is rarely recovered from these materials. It can also be found in nearly every other rare earth mineral. Yttrium has a wide range of applications, like as an electrolyte in solid oxide fuel cells (SOFCs) for distributed power generation, as well as in gas turbines for stationary power generation, where it is employed for thermal barrier coatings on the turbine blades, efficient microwave filters, and to make the high-temperature superconductor yttrium barium copper oxide (YBCO), commonly used in alloys that enhance the hardness of aluminium and magnesium alloys, and as a catalyst in ethylene polymerization [6–10].

Oxides are increasingly essential as future electronic materials in information and communication technology, with - applications in data storage and processing, optics, magnetic,energy conversion, and power converters. Rare-earth metal oxide semiconductor (REMOSs) films have recently received increased interest as gate dielectrics in metal–oxidesemiconductor (MOS) devices, owing to their high dielectric constant (k value), wide band gap (Eg), and excellent physical and chemical stability in contact with silicon substrates. Three methodologies are reported in recent articles, namely doping modification, nitriding treatment, and composites, which can provide some insights for the long-term growth of MOS devices in integrated circuits [11–13].

Rare earth metal oxide semiconductors (REMOSs), rare earth sulphides, rare earth hydroxides, and their composites are currently the most investigated rare earth based nanomaterials. Environmentally safe, cost-effective, and scalable synthetic techniques can be used to make rare-earth based nanomaterials with substantial electrochemical characteristics [14].

Rare-earth based nanomaterials have a low specific capacitance when compared to other transition metal oxides. Furthermore, the properties of rare-earth based nanomaterials, such as inferior conductivity, small specific surface area, and weak cycle stability, restrict their use in superconductors. Fortunately, the electronic conductivity of rare-earth based nanomaterials may be increased simply by altering their form and size, whereas other metal oxides require a conductive phase to couple with. Furthermore, a nanostructuring rare-earth-based material increases the surface area to volume ratio, allowing for the exposure of additional active areas. The active sites and high-energy crystal planes are exposed in a particular shape, allowing the material to be easily reduced and oxidised, resulting in a longer cycle life. There are also ways to improve the pseudocapacitance and cycle efficiency of nanomaterials made from rare earths by mixing them with other transition metal oxides.

To the best of our knowledge, publications on rare-earth metal oxide semiconductor-based nanomaterials are quite rare and are being used in a wide range of applications. In order to encourage future advances in this field, this review thoroughly covers the many synthesis techniques and applications of REMOSs nanoparticles, as well as the obstacles and possibilities that will face the material's future development.

2. Types of rare earth metal oxides Semiconductors:

Now a day's, rare earth metals are used in the form of nanomaterials in many diverse applications. Rare-earth based nanomaterials are categorized in three types such as rare earth sulphides, rare earth hydroxides and composites of sulphides and hydroxide [14–18].

2.1. (REOs):

The rare earth elements broadly divided into two types. Fig. 1 shows

that the classification of rare earth elements. Many researchers now days are work on listed rare earth elements by using various synthesis techniques and also prepared their oxide for the study of different applications. Rare-earth oxide surfaces are important for catalysis, and it was recently shown that they have inherent hydrophobicity. The surface chemistry of these oxides at low temperatures, on the other hand, is largely unknown [19–21].Rare earth oxides like CeO_2 and La_2O_3 are pseudocapacitor materials. CeO_2 is a new electrode material that presents a number of challenges. REOs surfaces play a significant role in catalysis and are used to catalyze a wide range of on-surface reactions, such as the conversion of syngas ($CO + H_2$) to alcohol, CO oxidation, NO to N_2 conversion, and the water–gas shift reaction, as well as the oxidation of alcohols [21,22]. Sato, Satoshi, et al. (2009) investigated the fundamental properties of REOs calcined at various temperatures. It has been reported with increasing calcination temperature, the crystal structures of Lu, Yb, Tm, Er, Y, Ho, and Dy oxides changed from monoclinic to cubic, but those of Sc, Ce, La, Pr, Nd, Sm, Eu, Gd, and Tb oxides remained unchanged. In the measurement of NH_3 adsorbed on the REOs at 25 °C, no acidic sites were found. CO_2 was adsorbed on the REOs, with CO_2 desorption peaks varying with the strength of the basic sites. Surface basic sites in light REOs like La_2O_3, Pr_6O_{11}, Nd_2O_3, and Sm_2O_3 desorbed CO_2 at temperatures below 500 °C, whereas structural carbonate degraded above 500 °C. Heavy REOs with weak basic sites include Dy_2O_3, Ho_2O_3, Y_2O_3, Er_2O_3, Tm_2O_3, Yb_2O_3, and Lu_2O_3. The basic characteristics of REOs are due to lanthanide contraction, which means that the strength of the basic sites reduces as the radius of the rare earth cation reduces [23].

2.2. Rare earth sulfides:

The most extensively explored and widely utilized rare earth sulphide in research is rare earth sesquisulfide, which can be denoted as RE_2S_3. It is a wide band gap semiconductor material with tunable band gap via doping. RE_2S_3 has a complicated structure and a variety of crystal shapes. It has a complex structures and a variety of crystal shapes. Light rare earth RE_2S_3 has three distinct crystal forms, such as α, β, and γ but heavy rare earth RE_2S_3 has many crystal forms, including δ, ε, and τ. By varying the temperature, the three crystal forms of RE_2S_3 α, β, and γ can be changed [14,24]. Rare earth sulphides (RES) have attracted attention in recent decades due to their intriguing physiochemical properties. RES been used as paints, photonic materials, and thermoelectric candidate materials. Rare earth sesquisulfides can be found in a variety of crystal forms, including structures of α, β, γ, δ, and ε. By sulfurizing rare earth compounds with H_2S or CS_2 gas at a lower temperature, rare earth sulphides could be synthesized at a lower tempe rature.To decrease the sulfurization time and examine the optimum sulfurization conditions of rare earth sulphides, YUAN Haibin et al. (2009) synthesized rare earth sulphides powders by sulfurizing their oxide powders with CS_2 gas.

2.3. Rare earth hydroxides:

Hexagonal crystal structures are common in rare earth hydroxides, such as $La(OH)_3$ and Nd(OH)3. Gd(OH)3. Hexagonal $RE(OH)_3$ (h-RE $(OH)_3$) nanostructures, a rare earth hydroxide, have been synthesised using a variety of techniques, including precipitation, microemulsion, and hydrothermal procedures. Metal hydroxides have larger theoretical specific capacitances than their oxide equivalents, according to recent research. Due to the strong attraction between the interlayer anions and the host layer, h-$RE(OH)_3$ is difficult to delaminate, unlike other hydroxides. Pre-intercalation with a long-chain surfactant (such as dodecyl sulphate) is necessary to facilitate the delamination of h-$RE(OH)_3$. Due to its unusual structure, h-RE $(OH)_3$ is more likely to develop a two-dimensional (2D) layered structure than rare earth oxides and rare earth sulphides, allowing it to increase active sites for electrochemical processes. With the inclusion of OH in the electrolyte, h-$RE(OH)_3$ stores charge by deprotonation (i.e. O–H bond breaking) processes [14,16,24]. Rare earth hydroxides, like other hydroxides, can form a 2D layered structure, which improves the movement of electrolyte ions, and as a result, they have steadily drawn the interest of researchers in recent years.

2.4. Thick and thin films of rare earth Oxides/Materials:

Rare earth materials as thin and thick films are an interesting research topic. A great number of articles on thick and thin films of rare earth-transition element alloys suited for various applications have been published. Because of the high reactivity, producing pure rare earth metal thin films has proven to be extremely difficult. Thin films of rare earth hydrides and rare earth oxides were created instead of pure rare earth metal thin films, and they were occasionally mistaken for metals. When the chemical problem was solved, however, it became clear that the actual inaterials generated, hydrides and oxides, were highly interesting research subjects in and of themselves. Because these materials have so many intriguing features, the majority of the results in the literature are focused on them.

Thin films of hydride and oxide are ideal for electron diffraction and electron microscopy studies. The oxides, in particular, provided a lot of new facts on topics like phase transitions, defects, and twinning mechanisms due to their polymorphism. The exceptional quality of these refractory materials' thin films, as well as their stability, regular thickness, and well-defined textures, as well as the ability to heat them with an electron beam and produce phase transitions directly within the electron microscope via pulse annealing or other methods, allowed for a number of direct observations not possible with other materials. With the advent of high-resolution electron microscopes, it was possible to obtain lattice images that directly project the crystal potential in these materials at resolutions as low as 2 A°, revealing details such as grain boundaries, twin planes, defect mechanisms, and coherent intergrowth of different phases or chemical compounds. As a result of the early attempts to manufacture and study pure rare earth metal thin films failing, fundamental crystallography has benefited the most. With the advent of even more powerful instruments like the high resolution scanning transmission electron microscope (STEM), it has become possible to use even raw thin films containing metallic parts, hgdrided parts, and oxidised parts, to distinguish their components through chemical analysis and interpretation of electron loss spectra, and finally to get on the metals. In this way, some progress has been made. Even when the most modern tools are utilized, it is still essential to be aware of all the pitfalls that a researcher may fall into while working with thin films containing rare earth materials [25,26].

3. Synthesis techniques of rare earth metal oxides semiconductors

Over the last decade, significant progress has been achieved in the controlled manufacturing of rare earth oxide nanoparticles. The design of size and form controlled nanoparticles, such as nanorods, nanoplates, nanopolyhedrons, and other nanostructures, has been the subject of numerous studies. Rare earth elements have a unique electrical layer structure and atomic radius, as well as chemical properties that are distinct from those of conventional elements. As a result, nano-rare earth oxide powder synthesis and post-processing techniques differ from those of other elements. The problems in synthesizing highquality materials with controlled size and shape, as well as finding - robust pathways in many systems, continue to make the preparation of rare earth oxide nanoparticles with suitable features a major task.

Rare earth elements have a distinct structure and properties. Due to their excellent redox capabilities and environmentally acceptable qualities, rare earth-based nanomaterials, particularly rare earth oxides, hydroxides, and sulphides, have attracted a lot of interest.

Hydrothermal, sol gel, CVD, electrodeposition, atomic layer deposition, micro-emulsion method, thermal decomposition, sonication, and electrochemistry physical vapour deposition, sputtering, thermal oxidation, and combustion methods are ecologically benign, easy, and low-cost techniques that can be used to synthesize rare earth-based nanomaterials [14].

3.1. Hydrothermal:

The hydrothermal process uses water or an alcohol-water mixed solution as a solvent in a highly sealed autoclave, which is then heated to a certain temperature to create a high temperature and high pressure environment. Under normal conditions, it is insoluble or insoluble at this time. The reactants dissolve and react, and then intense convection is generated, driven by the temperature differential of the solution in the autoclave, to form a supersaturated solution that then crystallises out. The process can produce nanopowders with uniform dispersion, narrow particle size distribution, good crystal shape, and controllable appearance, but it necessitates high temperature and high pressure equipment, which is costly, inefficient, and dangerous to use. One of the most essential and well-established processes for nonmaterial synthesis is hydrothermal synthesis. It deals with aqueous chemical processes in a closed, heated device, such as an autoclave or a bomb calorimeter.

Rare earth oxides can be synthesised using a simple hydrothermal process by precipitating rare earth hydroxide gels in basic solutions like NaOH, KOH, etc., at room temperature or at high temperatures. A simple hydrothermal approach, unlike vapor–liquid-solid or template-confined methods, can absorb specific reactant molecules or enhance nanoparticle growth in a certain direction. Consequently, hydrothermal methods have been found to be useful for making low-dimensional materials such as nanorods, nanowires, nanotubes, and nanoparticles [27].

Mai et al. devised a hydrothermal method for the synthesis of ceria nanorods, nanocubes, and nanopolyhedra by varying the temperature and NaOH content from 0.01 to 9 mol/L. Ceria nanorods were made at a high base concentration (6–9 mol/L) at a low temperature of 100 °C, while ceria nanopolyhedra were made at a very low NaOH solution (0.01 mol/L) at temperatures ranging from 100 to 180 °C. High temperatures (140–180 °C) and a high NaOH content were used to create ceria cubes. Hydrothermal treatment was carried out for 24 h in a very representative hydrothermal reactor, a stainless steel autoclave with a Teflon liner. Centrifugation was used to collect the white precipitates, which were then washed with deionized water and ethanol. After drying in the air at 60 °C overnight, yellow powders were obtained. At 1000 °C, the final calcination phase took 4 h [28]. Xu et al. demonstrated a simple hydrothermal synthesis technique for dysprosium and holmium hydroxide nanotubes [29]. These hydroxides must be separated, washed, dried, and calcined at high temperatures of 300–600 °C to obtain the final rare earth oxides. Wang and Li wrote about how to make single-crystal lanthanide hydroxide nanowires (RE = Y, La, Nd, Sm-Tm) [30].

Yang and colleagues reported a PVP-assisted easy hydrothermal process technique for making monodispersed CeO_2 hollow spheres from nano-octahedron building blocks. The synthesis technique included intense magnetic swirling of 0.099 g $CeCl_3{\cdot}7H_2O$ and 0.178 g PVP in 19 mL of deionized water, followed by adding 1 mL of formamide and 0.1 mL of H_2O_2 and stirring for 30 min. The yellow solution was transferred to a Teflon-lined autoclave and heated for 24 h at 180 °C. The collected light brown products were cleaned with distilled water and ethanol after cooling to ambient temperature, and then dried in an oven at 70 °C for 6 h to obtain CeO_2 hollow spheres. The hollow spheres have a pore size distribution of 3 to 15 nm and a diameter of 120–140 nm. The Oswald ripening method was used to create unique shaped hollow spheres from a nano-octahedron composite with an average edge length of 20 nm. The smaller crystallites in the centre disintegrated slowly, while the larger ones acted as growth seeds and continued to expand. After a long time and a lot of mass transfer, the hollow spheres finally formed [31]. The hydrothermal synthesis of rare-earth oxide nanocatalysts containing Ce, Pr, and Tb are depicted in Fig. 2 [32].

3.2. Precipitation

The precipitation method involves adding a precipitation agent to a rare earth salt solution, or hydrolyzing the solution at a specific temperature to generate insoluble hydroxides, hydrated oxides, or salts that precipitate out of the solution, and then removing the solvent. The original ions in the solution are then washed away, and the necessary oxide powder is formed by roasting, decomposing, or dehydrating. Oxalic acid precipitation, carbonic acid precipitation, hydroxide precipitation, homogeneous precipitation, complex precipitation, and other techniques of precipitation are used. For research and industrial production, the precipitation method is the most widely utilized technique. The benefits of this technique are inexpensive raw material costs, low equipment requirements, a simple process, simple operation, precise chemical composition control, and easy preparation of ultrafine powders with homogenous components. It is convenient in particle shape and size, and it can make high-purity products, but it is difficult to filter and agglomerate [33,34]. The flow of the precipitation synthesis method is shown in Fig. 3.

3.3. Co-precipitation

The co-precipitation technique has a strong history in the synthesis techniques of different materials. Two salt precursors, such as oxalates, carbonates, and hydroxides, are commonly dissolved in a common medium and precipitated out with a precipitant after pH adjustment. The precipitates are then calcined at high temperatures to obtain the final product [35]. The procedure of co-precipitation is quick and straightforward. However, in order to produce high-quality nanoparticles, the essential factors such as feed solution and precipitant content, temperature, mixing duration and medium pH must all be carefully monitored. The majority of rare earth nano-oxides generated via co-precipitation are nanoparticles, and only a handful has been reported for the production of other specific shaped nanostructures.

Higashi, Kenji, et al. Synthesis and sintering of rare-earth-doped ceria powder by the oxalate co-precipitation method. By mixing rare earth/cerium nitrate solution and an oxalic solution, rare earth/cerium doped ceria powders with a composition of $Ce_{0.8}RE_{0.2}O_{1.9}$ (RE = Yb, Y, Gd, Sm, Nd, and La) were synthesized. The oxalate solid solutions were generated by dropping the mixed 0.20 M nitrate solution into oxalic acid solutions ranging from 0.025 to 0.75 M, for example, in the $Ce_{0.8}Y_{0.2}O_3$ sample. Plate like particles with an average aspect ratio of 2.2–2.4 was produced from the oxalate. The oxalate converted into fine polycrystalline oxides with a particle size of 10 nm after being heated for 1 h at 600 °C [36]. The example of co-precipitation method is shown in Fig. 4.

3.4. Micro-emulsion

Another low-temperature method of producing mono-dispersed rare earth oxide nanoparticles in the range of 1 to 100 nm is the micro-emulsion method. Micro-emulsion is liquid systems made up of water, oil, and surfactant that are homogeneous, transparent, and thermodynamically stable. Although oil and water are incompatible, surfactant molecules can form an interfacial film between the water and oil phases, resulting in spontaneous mixing of the two phases. Co-surfactant is frequently used to ensure the interfacial layer's flexibility. This approach has the potential to develop micro-emulsion carriers that can improve drug loading capacity, solubility, and bioavailability, and hence could have an impact on the pharmaceutical sector [37,38].

Bumajdad et al. [39] reported the formation of ceria nanopowder from heptane-micro emulsified aqueous solutions of $CeCl_3$ or $Ce(NO_3)_3$ utilizing several surfactants such as AOT, DDAB, DDAB, and BRrij 35. In

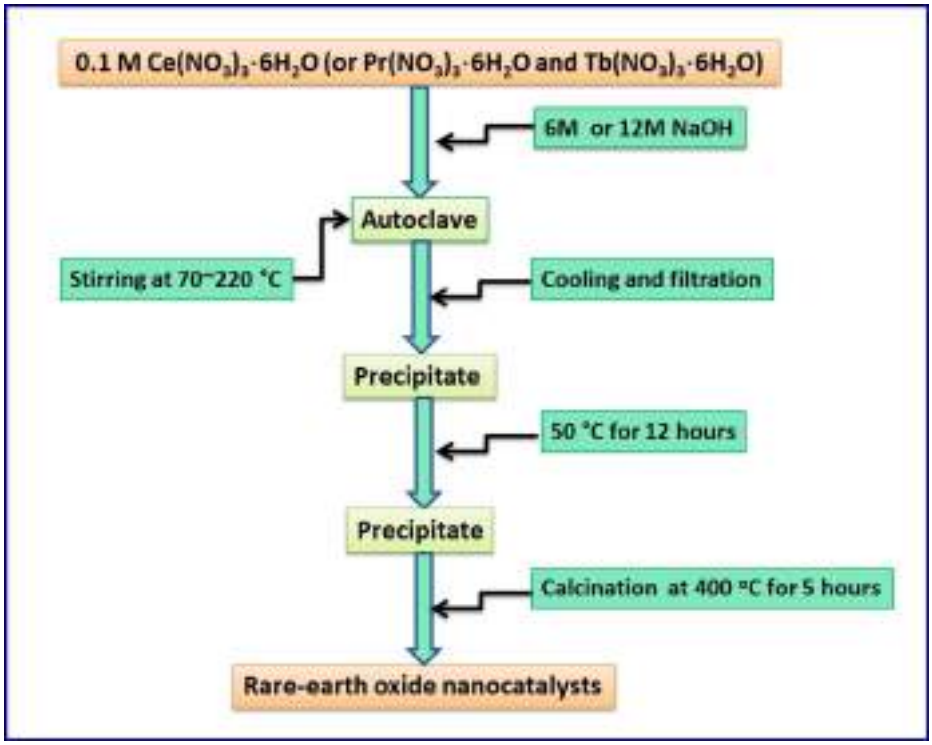

Fig. 2. Flowchart of hydrothermal synthesis technique for CeO_2, PrO_2 and TbO_2.

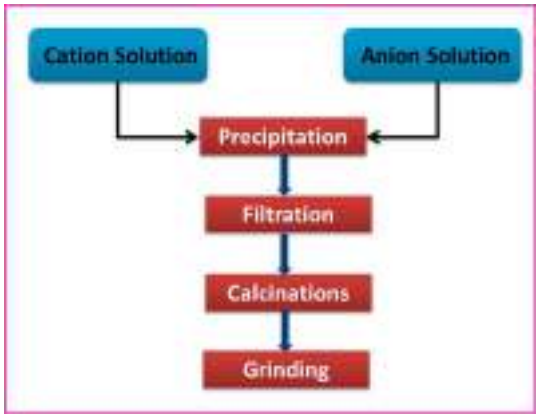

Fig. 3. Flowchart of the precipitation synthesis technique.

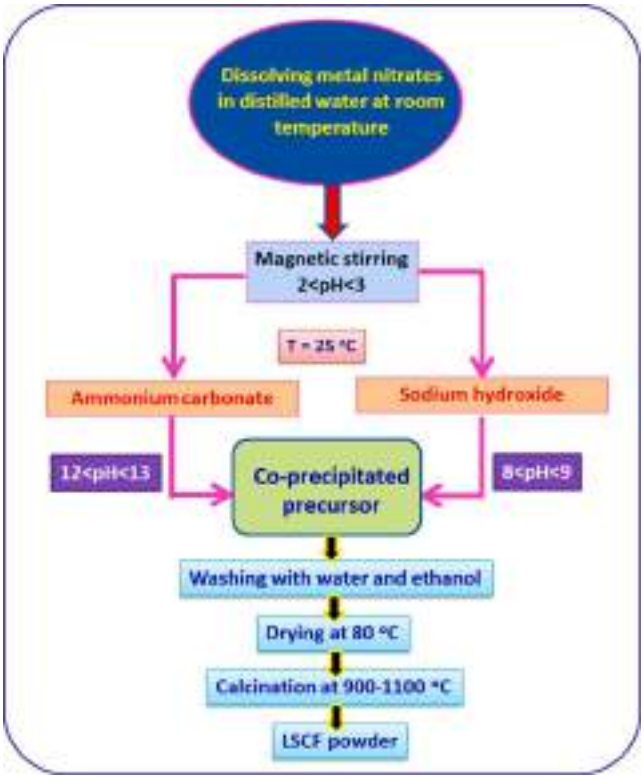

Fig. 4. Graphical flow of co-precipitation technique.

the presence of surfactants, they discovered nearly agglomerate-free nanosized ceria crystallites with a size range of 6–13 nm. Ceria with large specific areas (ca. 250 m^2/g) were seen in batches containing AOT or (DDAB + Brij 35)-stabilized microemulsions, but they agglomerated heavily when calcined at 800 °C (13–28 m^2/g). The double-calcined DDAB was able to create ceria with a high initial surface area (144 m^2/g) and good thermal stability (45–55 m^2/g at 800 °C).The Example of micro emulsion method as shown in Fig. 5.

3.5. *Microwave assisted synthesis*

Microwave assisted synthesis technique has several advantages, including time savings, cost savings, and environmental friendliness. Because of these advantages, microwave-assisted synthesis has piqued the interest of synthetic chemists and researchers. Microwave irradiation interacts with compounds selectively based on their microwave absorbing capability, allowing microwave energy transfer on specific molecules directly without thermal gradient effects, and causing superheating of solvents and super saturation of reactants. The quick heating has an impact on molecular mobility and collision, which could lead to an increase in chemical reaction rate and, as a result, a reduction in reaction time. It has been coupled with several traditional methods for creating inorganic nanomaterials, including as hydrothermal, sol–gel,

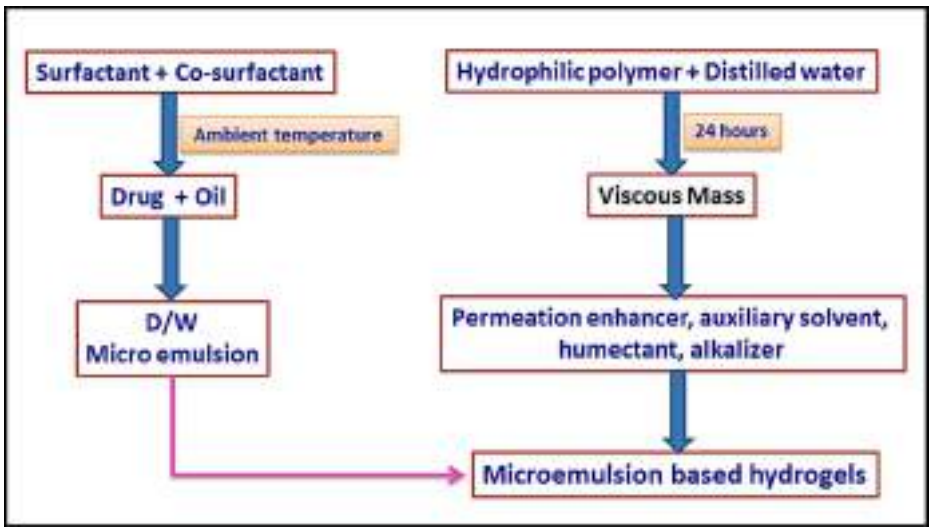

Fig. 5. Formulation of micro-emulsion based hydrogel.

solvothermal, and combustion processes, to speed up the reaction and save time [40–42].

Cao et al [43] used a programmable microwave oven to develop a template-free microwave aided hydrothermal technique for synthesis of ceria hollow spheres. In terms of temperature control, reaction time, and experiment feasibility and reproducibility, the programmable microwave outperforms the ordinary microwave. The ceria precursor was made by heating a mixture of $Ce(NO_3)_3{\cdot}6H_2O$, urea, and water to 170 °C in 2 min and keeping it there for 30 min. After that, the precursor was cooled, separated, and ethanol washed. The nanomaterial precursor was transformed to required ceria nanostructures by calcination at 500 °C for 2 h. Microwave heating was also thought to distribute heat consistently, resulting in ceria nanoparticles with uniform shapes and sizes. The development of hollow structures has been proposed as a self-templated, self-assembly process with an Ostwald ripening growth mechanism. Microwave synthesis and optical properties of uniform nanorods and nanoplates of rare earth oxides is shown in Fig. 6.

3.6. Sol-gel

Sol gel is a critical process for producing inorganic materials and plays a vital role in inorganic synthesis. Organometallic compounds or organic complexes produce a sol at low temperatures, then form a gel

Fig. 6. Flow chart of microwave assisted synthesis technique.

under certain conditions, and then undergo heat treatment. That is, the ultrafine nanopowder with bigger specific surface and better dispersion may be obtained by preparing the homogeneous solution, the sol, the gelation process, the drying of the gel, and the heat treatment process of the xerogel. The procedure may be performed in mild conditions, and the resulting powder is larger than the surface and has strong dispersibility; however, the reaction time is longer, taking several days to complete, and it is difficult to meet the criteria of large-scale manufacturing [44]. Another typical soft chemical technique for synthesizing solid materials like metal oxide from solution state precursors is the sol–gel process. It usually entails converting liquid precursors to a colloidal suspension known as a sol and subsequently, at low temperatures, to a multiphase network structure known as a gel. The size of a sol particle is determined by the solution composition, temperature, pH, and other factors, whereas the quality of a gel is primarily determined by the hydrolysis and condensation processes, which are influenced by metal ion electronegativity, precursor types, pH, solvent, and temperature. Calcinations at high temperatures are frequently required to generate high-purity and high-crystalline nanostructures. In fact, depending on the qualities of the final products, sol–gel chemistry can form materials such as films, powder, thick ceramics, bulk and nanoparticles, and so on [45–47].

The non-aqueous sol–gel technique has been used to synthesis rare earth mesoporous structures in recent years. Sol–gel chemistry has the advantage of producing metal oxides from homogeneous precursors, as opposed to furnace-based techniques such as hydrothermal, co-precipitation, or solvothermal methods, which are primarily based on inhomogeneous reacting materials. This allows for good control of complex inorganic metal oxides involving three or four metal precursors. Creating a homogeneous precursor at room temperature, on the other hand, does not ensure a homogeneous end result. Moreover, phase segregation occurs during the synthesis of several sol–gel methods shown in Fig. 7 [27,47].

Yuan and colleagues used Plutonic P123 as the template and ceric nitrate and zirconium oxide chloride as the precursors to make ordered mesoporous ceria-zirconia solid solutions using a sol–gel technique combined with evaporation-induced self-assembly in ethanol. Under optimal temperature and humidity conditions, a series of mesoporous $Ce1\text{-}xZrxO_2$ with various Ce/Zr ratios was produced. The TEM revealed a vast area of $Ce1\text{-}xZrxO_2$, implying a long-range organisedmesostructure. High-crystalline pore walls formed of multiple nanocrystallites with well-defined lattice planes were seen in the $Ce1\text{-}xZrxO_2$ structure. The nanocrystallite was about 3–4 nm in size. $Ce1\text{-}xZrxO_2$ solid solutions, which are highly ordered and porous, have demonstrated to be

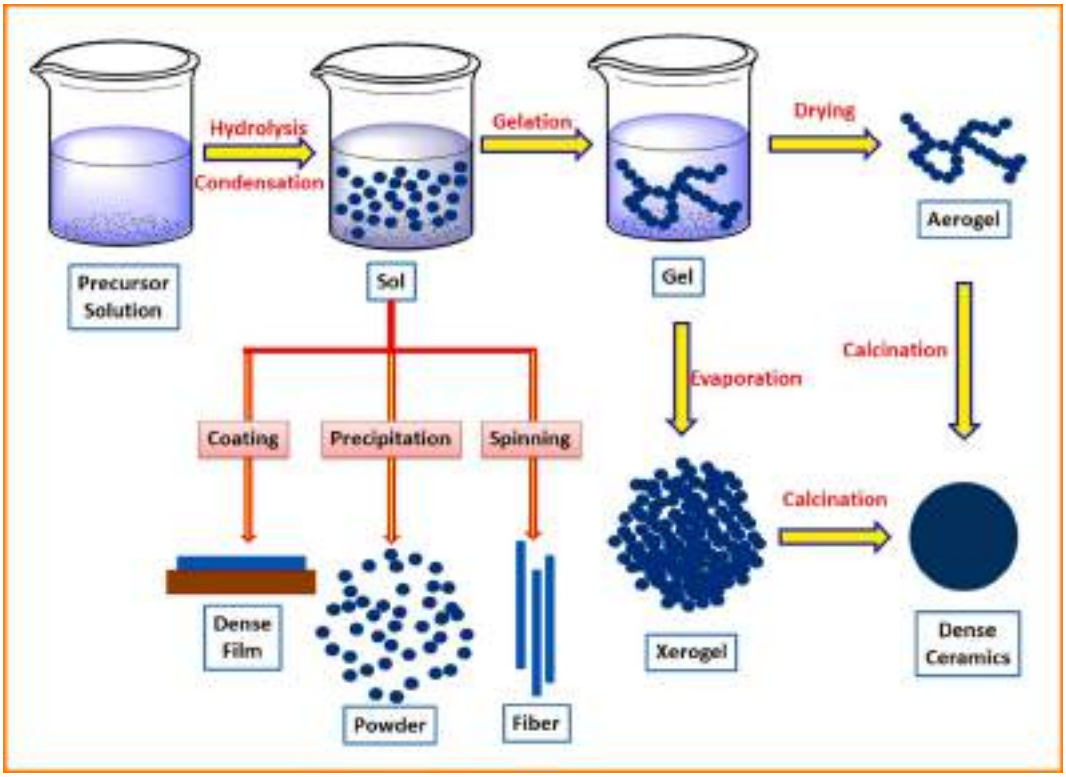

Fig. 7. Schematic of sol gel technique.

excellent catalytic supports for Pt in CO oxidation and cyclohexene hydrogenation [48].

Hu et al. proposed a sol–gel method for fabricating ceria hollow microspheres from cerium nitrate using polymeric templates on a large scale. PSAA colloids were spread equally in water to electrostatically adsorb Ce^{3+} ions onto the surface. After precipitating $Ce(OH)_3$ with NaOH, cerium hollow spheres were calcined at 773 K for 3 h to obtain cerium hollow spheres [49].

Reddy and his team synthesized. Yttrium Trioxide (Y_2O_3) by sol–gel technique [50]. Author reported the cubic phase crystalline structure of Y_2O_3has been confirmed by X-ray diffraction. The creation of an uneven plate-like structure with variable grain orientation has been confirmed by SEM pictures of Y_2O_3. In the range of 10–97 percent R_H, the humidity sensing characteristics of Y_2O_3 were investigated. The humidity sensor device made of Y_2O_3 pellets is subjected to various R_H levels. At normal temperature, the Y_2O_3 exhibits a 60-second response time and an 80-second recovery time. Y_2O_3 nanostructure humidity sensor is a promising device for industrial applications.

Richard, Diego, et al.reported the Pechini-type sol–gel (PSG) technique was used to successfully manufacture fine-grained nanocrystalline In-doped yttria powders [51]. The resulting materials crystallise in a cubic bixbyite structure, according to our findings by authors, and the In impurities are substituted at the cationic sites. The EIS tests revealed that the PSG samples had greater conductivities at grain interiors than the reference pellet made from Y_2O_3 commercial powder, and that the resistivity of the PSG samples is unaffected by in doping. These findings are supported by PAC spectroscopy of 111In(111Cd)-doped yttria crystals. The analysis of dynamic hyperfine interactions as a function of temperature revealed that the electron availability near the impurities responds differently depending on the sample fabrication process. These findings pave the way for a better understanding of the structural and electrical aspects of sol–gel processing.

3.7. Solvothermal:

The solvothermal technique is similar to the hydrothermal method in terms of nanomaterial synthesis, has been widely used in the production of accurate metal oxide nanostructures and microstructures. The composition of the reagents and solvents, as well as temperature and pressure, are key factors in solvothermal reactions. The reaction medium is the distinction between hydrothermal and solvothermal processes. Organic solvents like ethanol, CCl_4, or mixed solvents are used in solvothermal synthesis, whereas aqueous solutions are used in hydrothermal processes. Many scholars prefer to combine these two methods and refer to them as the hydro/solvothermal method for discussion because they have comparable synthetic rules and principles. Hydrothermal methods, on the other hand, are typically employed to make hydroxides, oxides, or oxyhydroxides, whilst solvothermal methods can be used to make non-oxide compounds like nitrides, chalcogenides, and so on. Solvothermal synthesis is important for the production of novel materials, especially those with unique structures and characteristics [52–55].

Chen and his team also focused on solvothermal synthesis for single-crystalline-like hollow nanostructures. Cerium chloride heptahydrate was dissolved in anhydrous ethanol, then proxyacetic acid was added as the oxidant in the manufacture of CeO_2 hollow nanocubes. The resulting slurry was placed in a Teflon-lined steel autoclave and cooked in the oven at 160 °C for 9 h. The white-brown goods were collected and cleansed after cooling. The final product, ceria hollow nanocubes, was made under vacuum for 24 h at 60°Celsius. The same cerium precursor $CeCl_3{\cdot}7H_2O$ was used in the CeO_2 hollow nanocrystals production. The capping agent was PVP, the solvent was a water–ethanol combination, and no oxidant was used. The resultant mixture was also sealed in a Teflon-lined steel autoclave with a capacity of 20 mL and heated at 160 °C for 24 h. The rest of the washing and drying procedures were identical to those used with the ceria hollow nanocubes. The catalytic activity of the final CeO_2 hollow nanocubes and nanostructures for CO oxidation was higher than that of commercial CeO_2 powder. A

combination mechanism of directed attachment and Ostwald ripening was proposed for the synthesis of hollow nanocubes. A dissolution followed by a recrystallization process was hypothesized as the mechanism for the latter nanostructure creation [53,54].

Yang, Jun, et al. has described a solvothermal method for generating homogeneous Y_2O_3:Eu^{3+} microspheres on a large scale and with ease. The spheres were made up of nanoparticles that were randomly aggregated. Their development was thought to be the result of an isotropic growth mechanism. Temperature, ethylene glycol, and CH_3COONa all had a role in the creation of such structures. Instead of acting as a solvent, ethylene glycol served as a capping agent to limit the rate at which nanoparticles grew in different directions. Without the presence of CH_3COONa, no solid product was produced [55]. Example of solvothermal synthesis method is depicted in Fig. 8 [56].

3.8. Thermal decomposition

Thermal decomposition of rare earth complexes such acetate, oleate, carbonate, and acetonate has been demonstrated to be a viable method for producing monodisperse, single crystalline, and high-dimension rare earth oxide nanocrystals. It's also the most effective approach to make high-quality nanoparticles smaller than 10 nm, which is useful for core–shell architectures. Organic surfactants were thought to serve a vital function in shape and size management. They operate as a capping agent, preventing nanoparticle development and aggregation while also controlling nanocrystal growth through a selective absorption action. This method is relatively new compared to the methods previously covered, however it is gaining popularity due to its excellent control over nanocrystalline characteristics. Despite its many benefits, thermal decomposition has a number of disadvantages, including a high operating temperature (usually between 250 and 330 °C), a high cost of metal precursors, different surfactants, and potentially hazardous byproducts [57–59].

Cao was the first to use a thermal decomposition approach technique to synthesis rare earth nano-oxides. He described the colloidal synthesis of squire Gd_2O_3nanoplates using oleylamine, oleic acid, and octadecene as solvents for the thermolysis of gadolinium acetate. 0.75 mmol gadolinium nitrate hydrate was dissolved in a solution containing oleylamine, oleic acid, and octadecene at 100 °C with stirring under a pressure of 20 mTorr in a conventional synthesis. The resultant solution was then heated to 320 °C for 5 min and then cooled to room temperature under Ar flow for 1 h. The precipitant adopted was a 1:1 combination of hexane and acetone. Under an Ar flow, the nanocrystalscrystallised and dried. These single-crystalline nanoplates had consistent shape and size and could self-assemble into superlattice structures [60]. The typical thermal decomposition method for the synthesis of lanthanum oxide is portrayed in Fig. 9 [61].

3.9. Sonochemical method

Sonochemical synthesis is a synthetic method that uses ultrasonic radiation (20 KHz-10 MHz). This approach allows for the creation of unique materials at room temperature, under low pressure, and with a quick reaction time. The strong ultrasound interacts with molecules to cause chemical changes in this approach. Ultrasound irradiation cannot directly interact with chemical bonds and break them because of the lower frequencies. Sonochemistry is caused by a physical phenomenon known as acoustic cavitation, which is connected to the development, growth, and implosive collapse of bubbles. Acoustic cavitation creates intense, transitory circumstances that allow chemical processes to take place and new materials to be synthesized. Metal nanoparticles, metal sulphides, metal alloys, and metal oxides, among other nanomaterials, have all been produced using the sonochemical approach. In sonochemical synthesis, the regulating parameters are sonication time, pH, temperature, ultrasound power, solvent, and gas pressure [62–64].

Zhong et al. adopted a simple sonochemical technique to synthesis

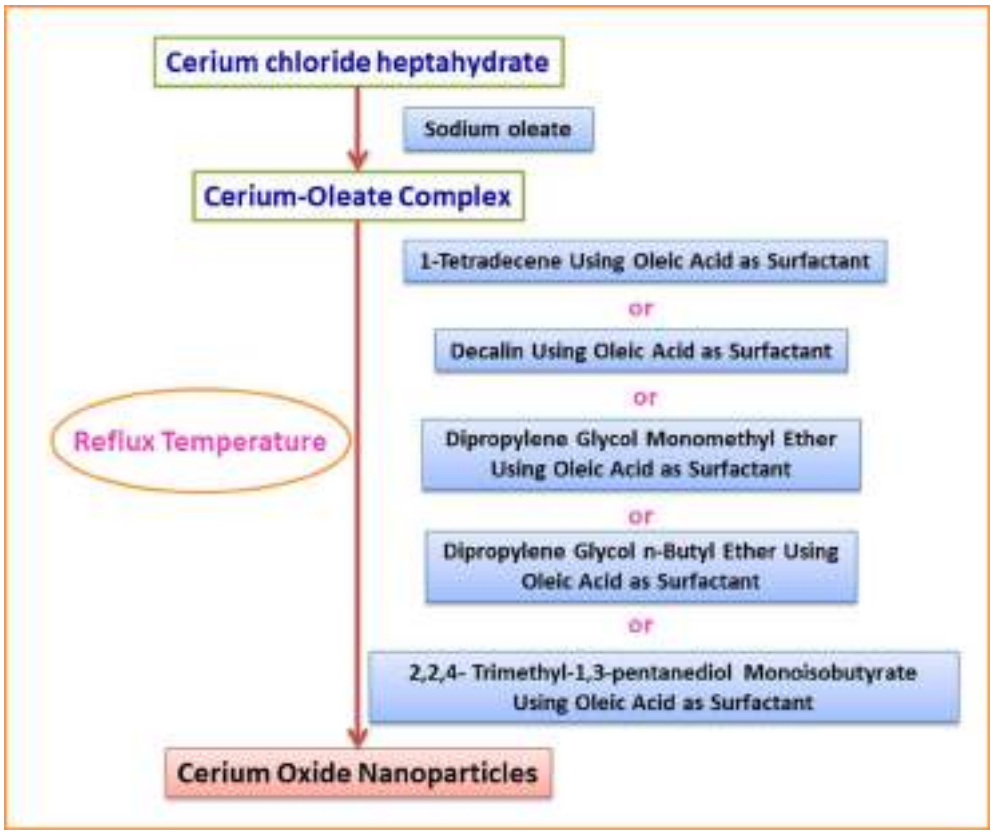

Fig. 8. Solvothermal synthesis technique.

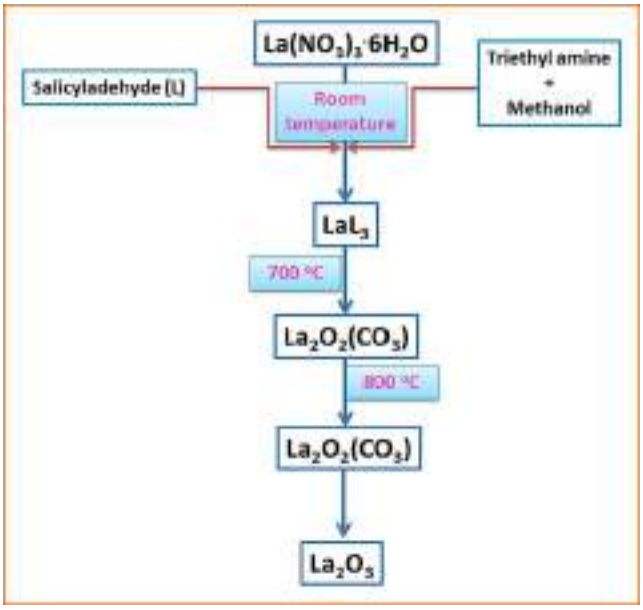

Fig. 9. Example of thermal decomposition of technique.

the flowerlike Y_2O_3. He reported that various factors might alter the structure growth. Commercial Y_2O_3 was dissolved in diluted HNO_3 (10 wt%) to prepare a solution for the synthesis. The mixed solution was sonicated for 30 min at 35–50 °C after evaporation, mixing with H_2O, and agitation. After that, the solution was filtered, washed, and dried, producing the flower like $Y_2(OH)_5NO_3{\cdot}1.5H_2O$. Calcinations of $Y_2(OH)_5NO_3{\bullet}1.5H_2O$ at 600 °C produced a Y_2O_3 flowerlike product. Several essential parameters, including time, precursor concentration, pH, and ultrasonication, were used to control the flowerlike structure. The flowerlike structure was retained in the 2 h response time, according with time-dependent experiment. The flower structure had totally changed after 2 h [65]. The example of Sonochemical synthesis is shown in Fig. 10 [66].

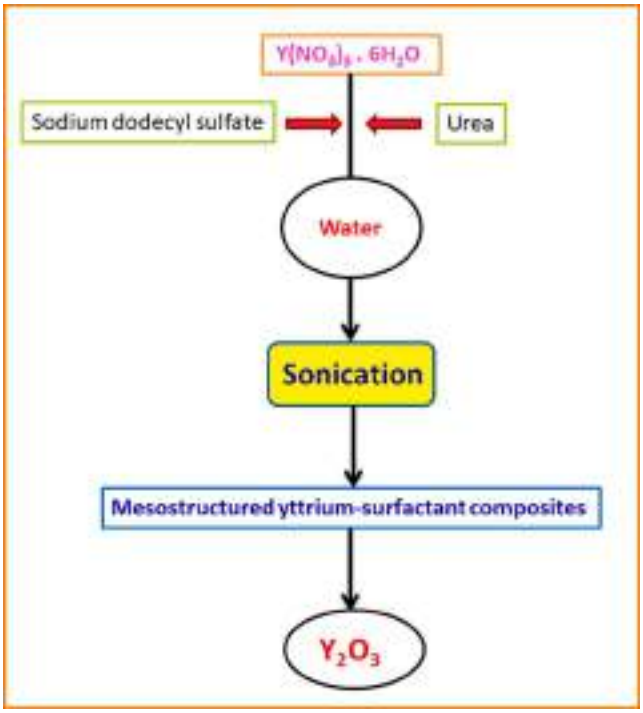

Fig. 10. Sonochemical synthesis of Y_2O_{3e}.

3.10. Other miscellaneous synthesis

While the methods outlined above are common in lab-scale and industrial-scale synthesis, there are many more traditional and non-traditional methods for creating rare earth oxide nanomaterials that merit our attention. Ball milling, thermal evaporation, spray pyrolysis, electro deposition, chemical vapor deposition (CVD), pulsed laser deposition, and other techniques are among them [67–72]. During the preparation of thin films of REMOSs the nanoparticles were synthesized in different ambient conditions. Thin films have a wide range of applications in technological advancements. Physical and chemical thin-film deposition techniques can be split into two parts based on the nature of the deposition process. Physical vapour deposition (PVD), laser ablation, molecular beam epitaxy, and sputtering are examples of physical techniques. Gas-phase deposition methods and solution techniques are among the chemical procedures. Chemical vapour deposition (CVD) and atomic layer epitaxy (ALE) are gas-phase techniques, while spray pyrolysis, sol–gel, spin, and dip-coating use precursor solutions.

Spin coating was used to deposit thin films for decades, and it is now the most used process for producing uniform thin films of photosensitive organic materials for gas sensing applications with thicknesses in the micrometre and nanometer range. Spin coating is a simple and quick way to make thin, uniform organic films from solutions. It's a technique for applying thin films on flat substrates in a consistent manner. In a nutshell, an excess of a solution is applied to the substrate, which is subsequently rotated at a high speed to disseminate the fluid using centrifugal force. A spin coater is a machine that is used for spin coating. Unlike many other film deposition techniques, spin coating is a reasonably simple and cost-effective method of processing (especially with regard to equipment costs). It provides a simple method for creating films of any composition. Repeatability is one of the most significant aspects of spin coating. Changes in the parameters that determine the spin process might cause significant changes in the coated films.

4. Applications of rare earth metal oxides Semiconductors:

Rare earth luminous materials can be used in a variety of applications. Industrially, they can be used to make metal and glass, but they can also be used for medical imaging, radar or computer screens, and everyday lighting fixtures. The application of rare earth nano-powder modified epoxy resin has significantly improved high temperature resistance, toughness, strength, and other properties in the application of electronic circuit substrates and packaging materials, and overall performance has been significantly improved and improved, with a small amount of material and low price. It can be used to increase the high temperature resistance, anti-ultraviolet, anti-aging, anti-radiation, and other properties of organic silicon materials, allowing them to better fulfill the unique needs of electronic and electrical appliances. The YBCO superconductor, which is made from nanoscale Y_2O_3, is a unique thin film material with great performance, max hardness, ease of production, application potential, and a wide range of applications. Rare earth luminescent nanomaterials are a new type of material with stable chemical and physical properties that can withstand the effects of high-power electron beams, high temperature resistance, strong ultraviolet light and high-energy radiation, and bright colors, high colour purity, and narrow emission bands; high conversion efficiency, strong light absorption, and fluorescence lifetime can be reacquired. The rare earth ion luminous compounds are also used in biomedicine and the energy sectors. In high-energy ion detectors, rare earth ions are employed. Scintillators are a group of materials that are related. These scintillators can be used in many different ways to detect cosmic rays in biomedical tests [73,74].

REOs such as Yttrium oxide (Y_2O_3), Lanthanum oxide (La_2O_3), Cerium oxide (CeO_2), Praseodymium oxide (Pr_6O_{11}), Neodymium oxide (Nd_2O_3), Samarium oxide (Sm_2O_3) Europium oxide (Eu_2O_3),

Gadolinium oxide (Gd_2O_3), Terbium oxide (Tb_4O_7), Dysprosium oxide (Dy_2O_3), Holmium oxide (Ho_2O_3), Erbium oxide (Er_2O_3), Ytterbium oxide (Yb_2O_3), Lutetium oxide (Lu_2O_3), Scandium oxide (Sc_2O_3) and Thulium oxide (Tm_2O_3) are employed in a variety of applications, including solar cell, optics, catalysis, ceramics, accuracy investment casting, glass fusing, and glass polishing, photocatalysis and other applications [75–93].

The use of lanthanoid absorptions for the production of photoprotective materials able to selectively attenuate different wavelengths is receiving increasing interest when it comes to the wide variety of uses of RE materials. Light absorption can sometimes result in the controlled conversion or breakdown of organic molecules, allowing RE-based materials to be used as photocatalysts. This section covers photoprotective and photocatalytic systems based on RE ions, with a focus on UV attenuation in biological systems and the ability to perform sunlight-activated processes using customisedphotocatalysts. The most investigated RE-containing material for photoprotection and UV absorption has been ceria nanoparticles (CeO_2). A variety of techniques are used to get materials with the right particle size, morphology, and structure for certain applications [74,94,95].

Nano-rare earth is being used in high-performance ceramics. Ceramics with electrical components (electronic sensors, PTC materials, microwave materials, capacitors, thermistors, etc.). Y_2O_3, La_2O_3, Nd_2O_3, Sm_2O_3, etc., are used as ceramic materials. Ceramics sintered with nano $Y_2O_3$and ZrO_2 at a lower temperature, for example, have high strength and toughness and are used in wear-resistant devices such as bearings and tools; multilayer chip capacitors and microwave devices made of nano Y_2O_3, Nd_2O_3, Sm_2O_3 and other materials have significantly improved performance [65]. The various applications of rare earth elements [96–99] have been listed in Table 1.

Food toxin (AFB1) detection using an electrochemical immunosensor modified with Sm_2O_3 nanorods. It has been shown that the electrophoretically deposited n-Sm_2O_3 film may be employed to immobilise Ab-AFB1 and BSA, as well as to inhibit non-specific binding sites of Ab-AFB1 in order to detect aflatoxins. This immunoelectrode's exceptional sensing performance has been paired with high thermal stability, good repeatability, and long-term stability [100]. This research has shown a new way to use rare earth metal oxide materials in clinical tests, antibody screening, and proteomics research.

In the neurological and hormonal systems of humans and other mammals, the important neurotransmitter dopamine plays a key function [101]. Due to its specialized position as a neuromodulator in the brain circuit, central and peripheral neuronal systems, dopamine is responsible for the physiological settings for memory, mobility, and attention [102]. Abnormal variations in dopamine levels or concentrations in the body can lead to abnormalities and diseases such as senile dementia, epilepsy, and Parkinson's disease [103]. Hypertension, asthma, and cordial violations during cardiac surgery are all caused by insufficient dopamine levels in the body. With its functional significance in mind, a quantitative approach for the precise measurement of dopamine in the sense of diagnosis and continuing surveillance of neurological imbalances must be established [104]. The numerous analytical estimation approaches for detecting dopamine levels appear to be complicated, expansive, and time consuming. The enzyme-based electrochemical biosensor approach is an excellent technology for rapid detection, ease of use, and simplicity in this regard [105]. Using a solution casting method, a dopamine biosensor was created by immobilizing the enzyme Tyr on the surface of the Au-La_2O_3/ITO electrode. The constructed electrode Tyr/Au-La_2O_3/ITO could be an effective biointerface for biosensors and bioelectronics using rare earth metal oxide nanoparticles [106].

Nanotechnologies have changed the face of science and technology in every discipline. It is concerned with the research and application of extremely small objects on the nanoscale (1–100 nm). Cerium is a common rare earth metal with various surface defects, primarily oxygen vacancies, resulting in the coexistence of two oxidation states: cerium (III) and cerium (IV), allowing for redox catalytic activity. Biosynthesis of nanoparticles has gotten a lot of attention since it is an environmentally beneficial process that uses plant extracts, microorganisms, nutrients, and other natural ingredients to make nanoparticles. Biosynthesized cerium oxide nanoparticles are thus non-toxic and biocompatible with living cells and tissues [107]. The contemporary context necessitates medical advancement due to an increase in the prevalence of lifestyle diseases, and the desire to provide treatment for life-threatening diseases such as cancer, HIV, and other disorders grows. Because of their unique redox capabilities, cerium oxide nanoparticles have been widely exploited in the field of biomedicine for cancer treatment, antimicrobial agents, bio-scaffolding, and biosensor device construction. These nanoparticles are also employed in solar cells, fuel oxidation catalysis, chemical mechanical polarisation, and corrosion

Table 1
Applications of rare earth elements.

Sr. No.	Atomic No.	Rare Earth Element	Applications
1.	57	Lanthanum(La)	Camera lenses and hybrid car batteries, studio lighting, laptop batteries, Electro microscopic tracer.
2.	58	Cerium (Ce)	Catalysts, ceramics, glasses, TV colour, Screen fluorescent lighting, Catalytic Converter, Carbon-arc Lighting.
3.	59	Praseodymium (Pr)	Ceramics, glass goggles for glass blowers and welders, motion picture industry for studio lighting and projector lights
4.	60	Neodymium (Nd)	IR filters, Specialised goggles for glass blowers, NIB magnets (PC, hand phones, medical equipment motors, wind turbines and Audio systems).
5.	61	Promethium (Pm)	Space craft and guide missiles atomic batteries
6.	62	Samarium (Sm)	Cancer treatment, carbon arc lighting for studio lighting and projection, Absorbers in nuclear reactors, magnets for headphones, and pickups for electric guitars.
7.	63	Europium (Eu)	Control rods for nuclear reactors, Compact fluorescent bulbs, anti-forgery marks on euro bank notes.
8.	64	Gadolinium (Gd)	MRI, Colour TV picture tubes, Microwave.
9.	65	Terbium (Tb)	Green phosphors in fluorescent lamps and color TV tubes. Speaker UV lights for euro bank notes, Magnet for wind turbine and hybrid car motors.
10.	66	Dysprosium (Dy)	Nuclear reactor control rods, Medium source rare –earth lamps MSRs) within the film industry, Compact discs and hard discs, Speakers, Used in dosimeters for measuring ionizing radiation.
11	67	Holmium (Ho)	Solid state lasers for non-invasive medical applications, Yellow or red colouring for glass, cubic zirconia, nuclear control rods,Used in medical, dental, and fiber-optical applications
12.	68	Erbium (Er)	Photographic filter, Colouring agent in glazes and glasses, laser for Skin (remove tattoo) Nuclear reactor control rods.
13.	69	Thulium (Tm)	Portable x-ray machine for medical use, Euro banknotes for its blue fluorescence under light to defeat counterfeiters.
14.	70	Ytterbium (Yb)	Fibre laser amplifiers, Catalyst, Stress gauges to monitor ground deformations caused by earthquakes or underground explosions, Source of gamma rays
15.	71	Lutetium (Lu)	Detectors in positron emission tomography, used in magnetic bubble memory devices.
16.	39	Yttrium (Y)	Garnets, High temperature superconductor YBCO, microwave filter, provide the red colour in television tubes.

prevention, in addition to biomedical fields. These nanoparticles have extraordinary capabilities, allowing them to be used in a wide range of medicinal, agricultural, and environmental applications. Because of its high antimicrobial efficiency, cerium oxide nanoparticles can be used in the production and commercialization of antimicrobial PPE (personal protective equipment), surgery suits, sanitizers, and other products [108–112].

Thulium oxide (Tm_2O_3) nanoparticles have catalytic, electrical, optical, and electrochemical applications. The nanostructured thulium oxide Tm_2O_3-based electrode provides a cost-effective technique and a novel promising platform for rare earth metal oxide material applications in electrochemistry and bioelectronics. Thulium oxide films have good conductivity and are stable in acidic and alkaline environments. As a result, it can be utilized as a modified electrode. Jay Singh et al. (2013) reported the optical and electro-analytical properties of the hydrothermally produced nanostructure Tm_2O_3 in the presence of AA. This study also demonstrates a very promising platform for the quick and precise quantification of AA in pharmaceutical and clinical samples using rare earth metal oxide material [113,114].

Motor vehicle exhaust is one of the most common sources of pollution in today's world. Catalytic purification is a widely utilized method of purifying car emissions on a global scale. Nano-rare earth catalysts are a novel type of high-efficiency car exhaust purification catalyst created by combining the high surface activity of nanomaterials with the properties of rare earth catalytic promoters in the catalyst. This catalyst combines the benefits of nanomaterials and rare earths into one package. Car exhaust can be properly purified with this device. Table 1 lists many other important applications for rare earth elements.

5. Conclusions and future perspectives:

The current research is a review of previous research on rare earth metal and rare earth metal oxide semiconductor (REMOSs) synthesis techniques and applications. Rare earth oxide nanoparticles have seen a tremendous increase in the last decade in terms of synthesis methods and uses. These studies show how to synthesise nanoparticles with a variety of properties and complex functions via a variety of synthetic techniques, including physical, chemical, biological, and hybrid methods. Rare earth nanoparticles have a wide spectrum of monodisperse or well-defined crystalline sizes, as well as sophisticated crystallite morphologies, compositions, and crystal structures. When used in catalysis, optics, sensors, and biological applications, well-controlled nanoparticles usually display good stability and great performance. High volumetric energy density, which can improve pseudo capacitive efficiency, environmentally friendly nature and abundant reserves, excellent redox properties, and rare earth oxides easily produce oxygen vacancies, which are conducive to the transport of electrolyte ions are all advantages of rare-earth-based nanomaterials. These are some of the notable benefits of nanostructures and nanocomposite made of rare-earth elements.

Rare earth nanoparticles are a novel class of material with predictable chemical characteristics and promising applications. They play a critical role in advancing modern society and raising of people living standards both today and in the future. The growth of rare earth elements into technology advancement, the ecology, and economic domains has resulted in a major increase in global demands. Over the next decade, global demand for autos, electronic goods, energy-efficient lighting, and catalysts is predicted to surge. The future of these technologies depends on REMs in future. The need for rare earth magnets is predicted to expand as the requirement for rechargeable batteries rises. Laparoscopic lasers, magnetic resonance imaging, and positron emission tomography scintillation detectors are projected to become more common as medical technology advances. Rapidly green technologies, including as electric car batteries, photovoltaic systems, and wind turbines, as well as others where REE are broadly utilized, are likely to generate great growth and demand for these metals in the near future, despite rising prices. REMs may be used in future military and naval arsenals to improve efficiency and handling. Modern treatment applications for REMOSs nanoparticles are being explored at an exponential speed, and upcoming technologies like nanotechnology may be leveraged in the future to improve their use in medicine.

CRediT authorship contribution statement

Amol S. Patil: Conceptualization, Methodology, Software, Formal analysis, Resources, Writing – original draft, Writing – review & editing, Visualization. **Arun V. Patil:** Supervision, Conceptualization, Methodology, Formal analysis, Resources, Writing – original draft, Writing – review & editing, Visualization. **Chandrakant G. Dighavkar:** Supervision, Conceptualization, Methodology, Formal analysis, Resources, Writing – original draft, Writing – review & editing, Visualization. **Vishnu A. Adole:** Writing – review & editing, Formal analysis, Visualization. **Umesh J. Tupe:** Conceptualization, Methodology, Software, Formal analysis, Resources, Writing – original draft, Writing – review & editing, Visualization.

Declaration of Competing Interest

The authors declare that they have no known competing financial interests or personal relationships that could have appeared to influence the work reported in this paper.

References

[1] V. Balaram, Rare earth elements: A review of applications, occurrence, exploration, analysis, recycling, and environmental impact, Geosci. Front. 10 (4) (2019) 1285–1303.
[2] N. Haque, et al., Rare earth elements: Overview of mining, mineralogy, uses, sustainability and environmental impact, Resources 3 (4) (2014) 614–635.
[3] M.L. Strauss, The recovery of rare earth oxides from waste fluorescent lamps. Colorado School of Mines, ProQuest Dissertations Publishing 10129925 (2016).
[4] P.H. Wald, A review of the literature on the toxicity of rare-earth metals as it pertains to the engineering demonstration system surrogate testing, Lawrence Livermore national laboratory University of California Livermore, California, 1989.
[5] F. Xie, et al., A critical review on solvent extraction of rare earths from aqueous solutions, Miner. Eng. 56 (2014) 10–28.
[6] I. Benammar, et al., The effect of rare earth element (Er, Yb) doping and heat treatment on suspension stability of Y_2O_3 nanoparticles elaborated by sol-gel method, J. Mater. Res. Technol. 9 (6) (2020) 12634–12642.
[7] B.o. Wu, et al., Ab initio study on structure and phase transition of A-and B-type rare-earth sesquioxides Ln2O3 (Ln= La–Lu, Y, and Sc) based on density function theory, J. Solid State Chem. 180 (11) (2007) 3280–3287.
[8] G.D. Wilk, R.M. Wallace, JáM Anthony, High-κ gate dielectrics: Current status and materials properties considerations, J. Appl. Phys. 89 (10) (2001) 5243–5275.
[9] Y. Guyot, et al., Luminescence properties of Y_2O_3 single crystals doped with Pr3+ or Tm3+ and codoped with Yb3+, Tb3+ or Ho3+ ions, Opt. Mater. 5 (1-2) (1996) 127–136.
[10] J. Hao, S.A. Studenikin, M. Cocivera, Blue, green and red cathodoluminescence of Y_2O_3 phosphor films prepared by spray pyrolysis, J. Lumin. 93 (4) (2001) 313–319.
[11] I.A. Smirnov, Rare-earth semiconductors studies in the soviet union, Le Journal de Physique Colloques 41 (C5) (1980) C5–143.
[12] Li, Shuan, et al. A review of rare-earth oxide films as high k dielectrics in MOS devices. Journal of Rare Earths 39. 2 (2020).doi.org/10.1016/j.jre.2020.10.013.
[13] M. Coll, et al., Towards oxide electronics: a roadmap, Appl. Surf. Sci. 482 (2019) 1–93.
[14] S. Liang, et al., Rare-earth based nanomaterials and their composites as electrode materials for high performance supercapacitors: a review. Sustainable, Energy Fuels 4 (8) (2020) 3825–3847.
[15] W. Gao, et al., Incorporation of rare earth elements with transition metal–based materials for electrocatalysis: a review for recent progress. Materials Today, Chemistry 12 (2019) 266–281.
[16] K. Chen, D. Xue, Formation of electroactive colloids via in situ coprecipitation under electric field: erbium chloride alkaline aqueous pseudocapacitor, J. Colloid Interface Sci. 430 (2014) 265–271.
[17] H. Zhao, et al., Rare earth incorporated electrode materials for advanced energy storage.", Coord. Chem. Rev. 390 (2019) 32–49.
[18] A.D. Yapryntsev, et al., Layered rare-earth hydroxides: a new family of anion-exchangeable layered inorganic materials, Russ. Chem. Rev. 89 (6) (2020) 629.
[19] M.P. Rosynek, Catalytic properties of rare earth oxides, Catalysis Reviews Science and Engineering 16 (1) (1977) 111–154.

[20] D.R. Mullins, The surface chemistry of cerium oxide, Surf. Sci. Rep. 70 (1) (2015) 42–85.
[21] E. Külah, et al., Surface chemistry of rare-earth oxide surfaces at ambient conditions: reactions with water and hydrocarbons, Sci. Rep. 7 (1) (2017) 1–10.
[22] C. Sun, H. Li, L. Chen, Nanostructured ceria-based materials: synthesis, properties, and applications, Energy Environ. Sci. 5 (9) (2012) 8475–8505.
[23] S. Sato, et al., Basic properties of rare earth oxides, Appl. Catal. A 356 (1) (2009) 57–63.
[24] R. Windiks, et al., Structure and optical properties of α-and γ-cerium sesquisulfide, J. Alloy. Compd. 459 (1-2) (2008) 438–446.
[25] M. Gasgnier, Rare earth metals, rare earth hydrides, and rare earth oxides as thin films, Phys. Status Solidi A 57 (1) (1980) 11–57.
[26] M. Gasgnier, et al., Rare-earth hydrides and rare-earth oxides in and from thin films of rare-earth metals, Journal of the Less Common Metals 34 (1) (1974) 131–142.
[27] Z. Yunyun, et al., Controllable design, synthesis and characterization of nanostructured rare earth metal oxides, Multifunctional Materials. De Gruyter (2020) 35–114, https://doi.org/10.1515/psr-2018-0084.
[28] H.-X. Mai, et al., Shape-selective synthesis and oxygen storage behavior of ceria nanopolyhedra, nanorods, and nanocubes, J. Phys. Chem. B 109 (51) (2005) 24380–24385.
[29] A.-W. Xu, et al., A simple method to synthesize Dy (OH) 3 and Dy2O3 nanotubes, J. Am. Chem. Soc. 125 (6) (2003) 1494–1495.
[30] X. Wang, Y. Li, Synthesis and Characterization of Lanthanide Hydroxide Single-Crystal Nanowires, AngewandteChemie 114 (24) (2002) 4984–4987.
[31] Z. Yang, et al., Fabrication of monodisperse CeO2 hollow spheres assembled by nano-octahedra, Cryst. Growth Des. 10 (1) (2010) 291–295.
[32] R.G. Wang, V. Sama, D.Q. Li, S.I. Mutinda, Hydrothermal synthesis of rare-earth oxide nanocatalysts for automotive exhaust clean-up, In Advanced Materials Research 512 (2012) 1624–1629.
[33] X.-L. Wang, Li-li Li, and Xue-chenDuan. Preparation of Nanometer Yttrium Oxide Powder, Rare Metals and Cemented Carbides 32 (1) (2004) 26–28.
[34] X.-B. Xiong, et al., Status in study of nanometer rare earth oxides prepared by precipitation methods, Xitu (Chinese Rare Earths) 34 (2) (2013) 81–86.
[35] Z. Tianshu, et al., Ionic conductivity in the CeO2–Gd2O3 system (0.05≤ Gd/Ce≤ 0.4) prepared by oxalate coprecipitation, Solid State Ionics 148 (3-4) (2002) 567–573.
[36] K. Higashi, et al., Synthesis and sintering of rare-earth-doped ceria powder by the oxalate coprecipitation method, J. Mater. Res. 14 (3) (1999) 957–967.
[37] S. Gai, et al., Recent progress in rare earth micro/nanocrystals: soft chemical synthesis, luminescent properties, and biomedical applications, Chem. Rev. 114 (4) (2014) 2343–2389.
[38] K.R. Jadhav, et al., Applications of micro-emulsion based drug delivery system, Curr. Drug Deliv. 3 (3) (2006) 267–273.
[39] A. Bumajdad, et al., Microemulsion-based synthesis of CeO2 powders with high surface area and high-temperature stabilities, Langmuir 20 (25) (2004) 11223–11233.
[40] P.A. Mello, J.S. Barin, R.A. Guarnieri, Microwave-assisted sample preparation for trace element analysis, Elsevier, Amsterdam, 2014, pp. 59–75.
[41] EdwardáH Grant, B.J. Halstead, Dielectric parameters relevant to microwave dielectric heating, Chem. Soc. Rev. 27 (3) (1998) 213–224.
[42] AdrineMalek Khachatourian, et al., Microwave synthesis of Y2O3: Eu3+ nanophosphors: A study on the influence of dopant concentration and calcination temperature on structural and photoluminescence properties, J. Lumin. 169 (2016) 1–8.
[43] C.-Y. Cao, et al., Ceria hollow nanospheres produced by a template-free microwave-assisted hydrothermal method for heavy metal ion removal and catalysis, The Journal of Physical Chemistry C 114 (21) (2010) 9865–9870.
[44] Q. Jinheng, et al., Preparation of ultrafine ceric oxide particles by different methods Sol-gel method [j], Journal of naijing university (natural sciences) 4 (1999) 486–490.
[45] G.S. Wu, et al., An improved sol–gel template synthetic route to large-scale CeO2 nanowires, Mater. Res. Bull. 39 (7-8) (2004) 1023–1028.
[46] M. Mogensen, Catalysis by ceria and related materials, Imperial College Press, London, 2002.
[47] A.E. Danks, S.R. Hall, Z.J.M.H. Schnepp, The evolution of 'sol–gel' chemistry as a technique for materials synthesis, Mater. Horiz. 3 (2) (2016) 91–112.
[48] Q. Yuan, et al., Ordered Mesoporous Ce1-x Zr x O2 Solid Solutions with Crystalline Walls, J. Am. Chem. Soc. 129 (21) (2007) 6698–6699.
[49] J. Hu, W. Deng, D. Chen, Ceria hollow spheres as an adsorbent for efficient removal of acid dye, ACS Sustainable Chem. Eng. 5 (4) (2017) 3570–3582.
[50] Reddy, LP Babu, H. G. Rajprakash, and Y. T. Ravikiran. Synthesis of yttrium trioxide (Y2O3) nanoparticles and investigations of its humidity sensing properties. AIP Conference Proceedings. Vol. 2142. No. 1. AIP Publishing LLC, 2019.
[51] D. Richard, et al., Preparation of In-doped Y2O3 ceramics through a sol-gel process: Effects on the structural and electronic properties, Ceram. Int. 46 (10) (2020) 16088–16095.
[52] G. Demazeau, Solvothermal reactions: an original route for the synthesis of novel materials, J. Mater. Sci. 43 (7) (2008) 2104–2114.
[53] G. Chen, et al., Template-free synthesis of single-crystalline-like CeO2 hollow nanocubes, Cryst. Growth Des. 8 (12) (2008) 4449–4453.
[54] G. Chen, et al., Benign synthesis of ceria hollow nanocrystals by a template-free method, Cryst EngComm 13 (8) (2011) 2904–2908.
[55] J. Yang, et al., Y_2O_3: Eu3+ microspheres: solvothermal synthesis and luminescence properties, Cryst. Growth Des. 7 (4) (2007) 730–735.
[56] H. Gu, M.D. Soucek, Preparation and characterization of monodisperse cerium oxide Nanoparticles in hydrocarbon solvents, Chem. Mater. 19 (5) (2007) 1103–1110.
[57] Goto, Aoi, Yoshio Ohta, and MikitoKitayama. Solid-state synthesis of metastable ytterbium (ii) oxide.Journal of Materials Science and Chemical Engineering 6.03 (2018) 85.
[58] D. Wang, et al., Mineralizer-assisted shape-control of rare earth oxide nanoplates, Chem. Mater. 26 (22) (2014) 6328–6332.
[59] H. Imagawa, S. Sun, Controlled synthesis of monodisperse CeO2 nanoplates developed from assembled nanoparticles, The Journal of Physical Chemistry C 116 (4) (2012) 2761–2765.
[60] Y.C. Cao, Synthesis of square gadolinium-oxide nanoplates, J. Am. Chem. Soc. 126 (24) (2004) 7456–7457.
[61] Ghiasi, M. and Malekzadeh, A. Synthesis, characterization and photocatalytic properties of lanthanum oxy-carbonate, lanthanum oxide and lanthanum hydroxide nanoparticles. SuperlatticesandMicrostructures 77(2015)295-304. doi. org/10.1016/j.spmi.2014.09.027.
[62] Y. Zhou, Controllable design, synthesis and characterization of nanostructured rare earth metal oxides, Multifunctional Materials. De Gruyter (2020) 35–114.
[63] H. Xu, B.W. Zeiger, K.S. Suslick, Sonochemical synthesis of nanomaterials, Chem. Soc. Rev. 42 (7) (2013) 2555–2567.
[64] Mason, Timothy J., and V. Sáez Bernal. An introduction to sonoelectrochemistry. Power Ultrasound in Electrochemistry: From Versatile Laboratory Tool to Engineering Solution (2012) 21-44.
[65] H.-X. Zhong, et al., Preparation and characterization of flowerlike Y2 (OH) 5NO3· 1.5 H2O and Y2O3 and their efficient removal of Cr (VI) from aqueous solution, The Journal of Physical Chemistry C 113 (9) (2009) 3461–3466.
[66] Y. Wang, L. Yin, A. Gedanken, Sonochemical synthesis of mesoporous transition metal and rare earth oxides, Ultrason. Sonochem. 9 (6) (2002) 285–290.
[67] W. Yuan, J. O'Connor, et al., Mechanochemical synthesis of homo-and hetero-rare-earth (III) metal–organic frameworks by ball milling, CrystEngComm 12 (11) (2010) 3515–3517.
[68] T. Zhang, F. Gu, D. Han, Z. Wang, G. Guo, Synthesis, characterization and alcohol-sensing properties of rare earth doped In2O3 hollow spheres, Sens. Actuators, B 177 (2013) 1180–1188.
[69] R. Djenadic, A. Sarkar, et al., Multicomponent equiatomic rare earth oxides, Materials Research Letters 5 (2) (2017) 102–109.
[70] T.D. Golden, Y. Shang, Q. Wang, T. Zhou, Electrochemical synthesis of rare earth ceramic oxide coatings, Advanced Ceramic Processing (2015) 85–110.
[71] Bonnet, G., Lachkar, M., Larpin, J.P. and Colson, J.C. . Organometallic chemical vapor deposition of rare earth oxide thin films. Application for steel protection against high temperature oxidation. Solid State Ionics 72(1994) 344-348.
[72] S. Prakash, S. Ghosh, et al., Intrinsic hydrophilic nature of epitaxial thin-film of rare-earth oxide grown by pulsed laser deposition, Nanoscale 10 (7) (2018) 3356–3361.
[73] Li, Hong, Fengjun Wei, and RuixiaoGao. Application of Nano Rare Earth Materials. E3S Web of Conferences 257 EDP Sciences (2021).
[74] Sousa, Paulo C. de, Juliana F. Lima, and Osvaldo A. Serra. "From lighting to photoprotection: fundamentals and applications of rare earth materials." Journal of the Brazilian Chemical Society 26 (2015): 2471-2495.
[75] K.K. Markose, R. Anjana, A. Antony, M.K. Jayaraj, Synthesis of Yb3+/Er3+ co-doped Y2O3, YOF and YF3 UC phosphors and their application in solar cell for sub-bandgap photon harvesting, J. Lumin. (2018) 204448–204456.
[76] H.M. Zakaly, A.S. Abouhaswa, S.A. Issa, M.Y. Mostafa, M. Pyshkina, R. El-Mallawany, Optical and nuclear radiation shielding properties of zinc borate glasses doped with lanthanum oxide, J. Non-Cryst. Solids 543 (2020), 120151.
[77] V.A. Adole, T.B. Pawar, P.B. Koli, B.S. Jagdale, Exploration of catalytic performance of nano-La2O3 as an efficient catalyst for dihydropyrimidinone/thione synthesis and gas sensing, Journal of Nanostructure in Chemistry 9 (1) (2019) 61–76.
[78] Z.S. Ghahsareh, S. Banijamali, A. Aghaei, Cerium oxide containing canasite based glass-ceramics for dental applications: Crystallization behavior, mechanical and chemical properties, Ceram. Int. 48 (6) (2022) 8489–8501.
[79] R.L. Saha, T.K. Nandy, R.D.K. Misra, K.T. Jacob, On the evaluation of stability of rare earth oxides as face coats for investment casting of titanium, Metall. Trans. B 21 (3) (1990) 559–566.
[80] L. Zhang, Y. Qu, X. Wan, J. Zhao, J. Zhao, Y. Yue, J. Kang, Influence of rare earth oxides on structure, dielectric properties and viscosity of alkali-free aluminoborosilicate glasses, J. Non-Cryst. Solids 532 (2020), 119886.
[81] Bao X.J., Zhang Z.J., Luo T.Z., Wu X.T., Xie Z.S., Lan S.K., Xie S.Z. and Zhou D.B. . Conversion of cerium and lanthanum from rare earth polishing powder wastes to CeO2 and La0. 6Ca0. 4CoO3. Hydrometallurgy 193(2020) 105317.
[82] K. Kannan, D. Radhika, A.S. Nesaraj, K.K. Sadasivuni, K.R. Reddy, D. Kasai, A. V. Raghu, Photocatalytic, antibacterial and electrochemical properties of novel rare earth metal oxides-based nanohybrids, Materials Science for Energy Technologies 3 (2020) 853–861.
[83] Y. Cheng, H. Nan, Q. Li, Y. Luo, K. Chu, A rare-earth samarium oxide catalyst for electrocatalytic nitrogen reduction to ammonia, ACS Sustainable Chem. Eng. 8 (37) (2020) 13908–13914.
[84] H.A. Saudi, W.M. Abd-Allah, K.S. Shaaban, Investigation of gamma and neutron shielding parameters for borosilicate glasses doped europium oxide for the immobilization of radioactive waste, J. Mater. Sci.: Mater. Electron. 31 (9) (2020) 6963–6976.
[85] L.P. Lingamdinne, S. Lee, J.S. Choi, V.R. Lebaka, V.R.P. Durbaka, J.R. Koduru, Potential of the magnetic hollow sphere nanocomposite (graphene oxide-

gadolinium oxide) for arsenic removal from real field water and antimicrobial applications, J. Hazard. Mater. 402 (2021), 123882.
[86] Y.F. Jiang, C.Z. Yuan, T.Y. Cheang, A.W. Xu, Highly active and durable Pd nanocatalyst promoted by an oxygen-deficient terbium oxide (Tb 4 O 7–x) support for hydrogenation and cross-coupling reactions, New J. Chem. 43 (23) (2019) 9210–9215.
[87] U. Gurer, O. Yilmaz, H. Karacali, S. Kaya, E. Yilmaz, Co-60 gamma radiation influences on the electrochemical, physical and electrical characteristics rare-earth dysprosium oxide (Dy2O3), Radiat. Phys. Chem. 171 (2020), 108684.
[88] D. Hu, X. Li, I. Snetkov, A. Yakovlev, S. Balabanov, M. Ivanov, X. Liu, Z. Liu, F. Tian, T. Xie, O. Palashov, Fabrication, microstructure and optical characterizations of holmium oxide (Ho2O3) transparent ceramics, J. Eur. Ceram. Soc. 41 (1) (2021) 759–767.
[89] D. Yılmaz, B. Aktaş, Ş. Yalçın, M. Albaşkara, Erbium oxide and Cerium oxide-doped borosilicate glasses as radiation shielding material, Radiat Eff. Defects Solids 175 (5–6) (2020) 458–471.
[90] Costa B.C., Guerreiro-Tanomaru J.M., Bosso-Martelo R., Rodrigues E.M., Bonetti-Filho I. and Tanomaru-Filho M. . Ytterbium oxide as radiopacifier of calcium silicate-based cements. Physicochemical and biological properties. Brazilian Dental Journal 29(2018) 452-458.
[91] Zhang D., Lin W., Lin Z., Jia L., Zheng W. and Huang F. . Lu2O3: A promising ultrawidebandgap semiconductor for deep UV photodetector. Applied Physics Letters 118(21)(2021) 211906.
[92] X.Y. Zhang, M. Xu, S.Z. Cao, W.B. Chen, W.Y. Yang, Q.Y. Yang, Enhanced thermal conductivity of diamond/copper composite fabricated through doping with rare-earth oxide Sc2O3, Diam. Relat. Mater. 104 (2020), 107755.
[93] D. Ghosh, N. Choudhury, S. Balaji, K. Dana, A. Dhar, Synthesis and characterization of Tm2O3-doped Lu2O3 nanoparticle suitable for fabrication of thulium-doped laser fiber, J. Mater. Sci.: Mater. Electron. 32 (4) (2021) 4505–4514.
[94] D.S. Filho, C. Paulo, et al., Amphiphilic cerium (III) β-diketonate as a catalyst for reducing diesel/biodiesel soot emissions, Appl. Catal. A 360 (2) (2009) 210–217.
[95] S. Filho, C. de Paulo, O.A. Serra, Rare earths in Brazil: historical aspects, production, and perspectives, Quim. Nova 37 (4) (2014) 753–760.
[96] L.M. Suli, et al., A review of rare earth mineral processing technology, Chemical Engineering Research Bulletin (2017) 20–35.
[97] M. Humphries, Rare earth elements: the global supply chain. Congressional Research Service, The Library of Congress, Washington, 2013.
[98] R. Tharumarajah, P. Koltun, Cradle to gate assessment of environmental impact of rare earth metals. Proceedings of the 7th Australian Conference on Life Cycle Assessment, 2011.
[99] C.H.E.N. Zhanheng, Global rare earth resources and scenarios of future rare earth industry, J. Rare Earths 29 (1) (2011) 1–6.
[100] J. Singh, A. Roychoudhury, A highly efficient rare earth metal oxide nanorods based platform for aflatoxin detection, Journal of material chemistry B 1 (35) (2013) 4493–4503, https://doi.org/10.1039/c3tb20690d.
[101] G.D. Stuber, M.F. Roitman, P.E.M. Phillips, R.M. Carelli, R.M. Wightman.Rapid dopamine signaling in the nucleus accumbens during contingent and noncontingent cocaine administration, Neuropsychopharmacology 30 (2005) 853-863. doi:10.1038/sj.npp.1300619.
[102] Shao-wen hao and Qun-hua jin. "Association between the +104T/C polymorphism in the 5'UTR of GDF5 and susceptibility to knee osteoarthritis: A meta-analysis".Spandidos publications Molecular medicine reports (2012) 485-488. doi.org/10.3892/mmr.2012.1179.
[103] M.L. Huffman, B.J. Venton, Carbon-fiber microelectrodes for in vivo applications, Analyst. Royal Society of chemistry 134 (2009) 18–24.
[104] H. Beitollahi, H. Karimi-Maleh, H. Khabazzadeh, Nanomolar and selective determination of epinephrine in the presence of norepinephrine using carbon paste electrode modified with carbon nanotubes and novel 2-(4-oxo-3-phenyl-3, 4-dihydro-quinazolinyl)-N′-phenyl-hydrazinecarbothioamide, Anal. Chem. 80 (24) (2008 2008,) 9848–9851.
[105] B.J. Venton, Q. Cao. Fundamentals of fast-scan cyclic voltammetry for dopamine detection. Analyst 145(2019) 1158-1168.
[106] Ankur Srivastava, Gargi Mishra. A highly efficient nanostructured Au@La2O3 based platform for dopamine detection.Material Letters 308 part B (2022) 131231.
[107] Kshitij RB Singh, VanyaNayak, TanushriSarkar and RavindraPratap Singh. Cerium oxide nanoparticles: properties, biosynthesis and biomedical application. RSC Advances 10 (2020) 27194-27214.
[108] K.R.B. Singh, M. Fernandes, T. Sarkar, P. Sridevi, Infect. Non, Infect. Dis. 4 (2019) 1–7, https://doi.org/10.24966/inid8654/100027.
[109] A. Corma, P. Atienzar, H. Garcia, J.Y. Chane-Ching, Hierarchically mesostructured doped CeO2 with potential for solar-cell use, Nat. Mater. 3 (6) (2004) 394–397.
[110] T. Zhang, Y. Xin, Z. Ren, F. Qi, C.K. Law, Catalytic oxidation of methane over PdO in wire microcalorimetry, Combust. Flame 160 (1) (2013) 149–154.
[111] K. Reed, A. Cormack, A. Kulkarni, M. Mayton, D. Sayle, F. Klaessig and B. Stadler Environ. Sci. Nano1(2014) 390–405. DOI: 10.1039/c4en00079j.
[112] V.K. Ivanov, A.B. Shcherbakov, A.V. Usatenko, Structure-sensitive properties and biomedical applications of nanodispersed cerium dioxide, Russ. Chem. Rev. 78 (9) (2009) 855, https://doi.org/10.1070/rc2009v078n09abeh004058.
[113] J. Singh, M. Srivastava, A. Roychoudhury, D.W. Lee, S.H. Lee, B.D. Malhotra, Optical and electro-catalytic studies of nanostructured thulium oxide for vitamin C detection, J. Alloy. Compd. 578 (2013) 405–412.
[114] M. Kouda, T. Kawanago, P. Ahmet, K. Natori, T. Hattori, H. Iwai, K. Kakushima, A. Nishiyama, N. Sugii, K. Tsutsui, Interface and electrical properties of Tm2O3 gate dielectrics for gate oxide scaling in MOS devices, J. Vacuum Sci. Technol. B, Nanotechnol. Microelectron.: Mater., Process., Meas., Phenom. 29(6)(2011) 062202.

IJCRT.ORG ISSN : 2320-2882

INTERNATIONAL JOURNAL OF CREATIVE RESEARCH THOUGHTS (IJCRT)

An International Open Access, Peer-reviewed, Refereed Journal

SYNTHESIS AND CHARACTERIZATIONS OF CUO-ZNO NANO COMPOSITE BINARY OXIDE THICK FILMS AS H_2S GAS SENSOR

*[1]Umesh J. Tupe, [2] M. S. Zambare, [3]A. V. Patil, [4]C.G. Dighavkar, [5]Amol S. Patil

[1]Department of Electronic Science, VADP's Arts, Science & Commerce College, Shirsondi, Tal – Malegaon, Dist-Nashik, Affiliated to SPPU, Pune, Maharashtra – 423208, India.

[2]Research Centre in Electronics, Department of Electronic Science, Fergusson College, Pune, (M.S.), Affiliated to Savitribai Phule Pune University, Pune, India.

[3]Department of Physics, MGV's, Arts, Science and Commerce College, Manmad, Dist. Nashik 423104, India

[4]Departmet of Physics, MGV's, Arts, Science and Commerce College, Surgana, Dist. Nashik 422211, India

[5]Department of Electronics, SSR College, Silvassa-396230, India

Abstract:

CuO and ZnO nanoparticles were synthesized using cost effective precipitation and green synthesis methods respectively. Synthesized nanoparticles were used to establish CuO-ZnO binary oxides thick films. Thick films have been developed by standard screen printing technique on a glass substrate. The structural characterizations of films were studied using FESEM, EDAX and XRD. The electrical characterization of thick films were studied using resistivity, activation energy and temperature coefficient of resistance (TCR). The XRD plots matched perfectly with JCPDS card number 80-1916 and 80-0074 for CuO and ZnO respectively and found that ZnO has hexagonal structure and CuO has monoclinic structure. Hydrogen sulphide gas sensing mechanisms of these films were investigated at various operating temperatures and PPM concentrations of gas. The 5% ZnO doped CuO binary oxide thick films shows maximum sensitivity of 78.8% sensitivity to 100 ppm of H_2S gas at operating different temperature 50^0 C. The films also showed a rapid response time of 8 seconds and recovery time of 20 seconds.

Keywords: *Synthesis, Nanoparticles, Binary oxide, Sensitivity, H_2S gas.*

1. Introduction

Because of the increased concentrations of poisonous gases in the environment due to industry, inorganic farming, cars, and other sources, the development of efficient gas sensors for the detection of harmful gases is critical. A gas sensor is a device that can tell us about the chemical composition of the air around it [1].Over 68 years ago, Brattain and Bardeen reported that gas absorption on the surface of a semiconductor can cause a change in the material's resistance. Since then, Seiyama et al 1962 and Taguchi 1970 have made persistent and effective efforts to use this change for gas detection [2, 3]. Metal oxides are one of them, and they are considered feasible materials for gas sensor applications due to their high stability, sensitivity, and ability to detect a wide range of target gases. Metal-oxide gas sensors have a number of drawbacks, including a long response time, low conductivity, a high operating temperature, and a slow recovery time. Gas sensors based on Metal Oxide Semiconductors have been utilized to monitor flammable and harmful gases in both residential and industrial environments. Because of their wide range of applications, low cost, reliability, small size, and low power consumption, gas sensors are in high demand [3, 4]. The two types of metal oxide semiconductors (MOS) are n-type and p-type. Electrons make up the majority of charge carriers in n-type MOSs, whereas holes make up the majority of charge carriers in p-type MOSs. MOS-based sensors work on the principle of resistance changes when exposed to the target gases or humidity. Oxidizing gases raise n-type semiconductor resistance while lowering p-type semiconductor resistance, whereas reducing gases do the opposite. Resistance decreases when p-type films are exposed to oxidising gases, but resistance increases when exposed to reducing gases. The resistance of n-type films increases when exposed to oxidising gases, while resistance decreases when exposed to reducing gases. When target gases combine with oxygen species, free electrons are produced [4-6]. Although p-type MOS has its own advantages, such as superior catalytic properties and lower humidity and operating temperature dependence [7, 8], N-type MOS has better sensitivity to target gases than p-type MOS. Traditional fabrication techniques have improved, allowing for the production of low-cost sensors with good response and dependability. Researchers wanted to create a highly sensitive gas sensor that could respond quickly and recover quickly. The detecting performance of MOS gas sensors is influenced by operating temperature, specific surface area, crystalline size, crystal structure, and resistivity quality. During the last few decades, extensive research has used doping methods to improve the characteristics of MOS. Doping and flaws have played a key role in enhancing material structural, electrical, optical, and mechanical properties over the years. Due to the deployment of sophisticated production and characterization technologies, we are mechanical properties by altering the fundamental structure at the nano-scale. Such research and discoveries are necessary to address technological, economic, and environmental challenges [9, 10].

2. Experimental work

2.1 Synthesis of copper oxide nanoparticles using precipitation method:

Cupric acetate [Cu (CH_3COO). H_2O] was used as a source of copper. Cupric acetate (7.9 gm) and NaOH pellet (5.4 gm) were dissolved separately into distill water (100 ml). The solution of cupric acetate and distill water stirred continuously at 80 ^oC for one hour using magnetic stirrer. Initially the cupric acetate greenish color and pH of solution is 5.29. Figure 1 (a) indicates the pH of cupric acetate and distills water solution. During the stirring NaOH solution mix drop wise in the cupric acetate solution still pH of solution reached at 11.20. Figure 1(b) indicates the pH of cupric acetate solution after added NaOH. After that the formation of obtained compound filtered using whatman filter paper 41 Figure 1(c). Using silica crucible the obtained compound was sintering at 400^oC for 2 hours. After that nanoparticles of CuO obtained shown in Figure 1 (d).

Figure 1 (a): The pH of cupric acetate and distills water solution, (b): The pH of cupric acetate solution after added NaOH, (c): Filter obtained compound using whatman filter paper 41 and (d): Obtained copper oxide nanoparticles after sintered at 400^oC.

2.2 Synthesis of ZnO nanoparticles using green synthesis method

The nanoparticles of zinc oxide synthesis by green synthesis method using zinc nitrate Zn ($NO_3O_2.6H_2O$). Zinc nitrate is a source of Zn. In this experiment 0.02M of Zinc nitrate hexa hydrate in 250 ml beaker and dissolved it into 50 ml distilled water, i.e. 5.94 gm of Zn ($NO_3O_2.6H_2O$) in 50 ml distilled water. During the addition of zinc nitrate in distilled water constant string is necessary after that aqueous leaf extract of corriandrum is introduces into above solution of zinc nitrate in the following particular set of addition of this extract into the solution. The obtained precipitate is dry at room temperature of 15-18 hrs then power of 240 pale white colored is dry on hot plate at 80- 90^oC for 5 hrs and after that pale white colored nano composites of ZnO is obtained. The flow chart of the experimental work performed for synthesis of ZnO nanoparticles using green synthesis method mention in Figure 2.

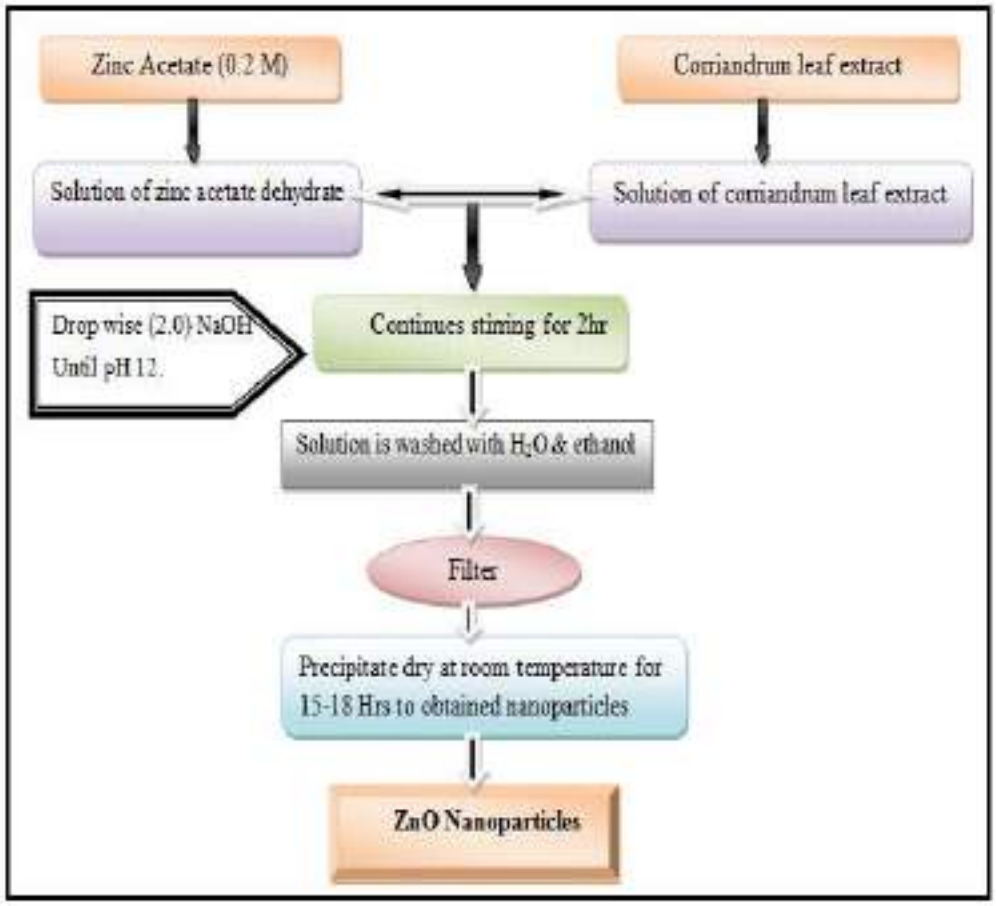

Figure 2: Synthesis of ZnO nanoparticles using green synthesis method

2.3 Preparation of pastes of additive and functional materials for thick films

Inorganic material 70% and organic material 30% were taken to prepare ZnO doped CuO binary oxide thick films. Inorganic material consists of synthesized nanoparticles of functional materials such as CuO. Organic part consists of ethyl cellulose (8%) and butyl carbitol acetate (92%). The ethyl cellulose as used as temporary binder and BCA used drop wise to prepare paste with a proper viscosity and Wt. % additive at different concentration (1%, 3% and 5%) were added in the functional base inorganic material for preparation of nanocomposites binary oxide thick films.

2.4 Thick film preparation method

In the current research study, 120 mesh nylon screens were used to develop thick film. A 1.25 cm x 2.50 cm rectangular window was developed using standard lithographic techniques on the screen. Paste or ink is an important part of thick film printing. The paste is evenly pressed to the top of the screen using mechanical drainage. The paste forms a layer on the surface of the substrate. Layer work is done by the components of the paste. The paste contains nano sized functional metal oxide material, ethyl cellulose and temporary binder likes BCA as a solvent. Using squeegee paste is put on glass substrate using screen printing setup. Ones films are prepared it kept in ambient condition for settle down. The films were exposed to infra-red radiation for approximately 30 min. The organic solvents were removed by this exposure. Ones material pasted on the substrate becomes stable films are ready to use for further process. The next phase involves the heat treatment of the prepared thick films. After firing approximately 350 ^{o}C into the muffle furnace, the film's fine material becomes a solid composite. This process is called firing. Figure 3 shows the steps for preparation of CuO-ZnO binary oxides thick films.

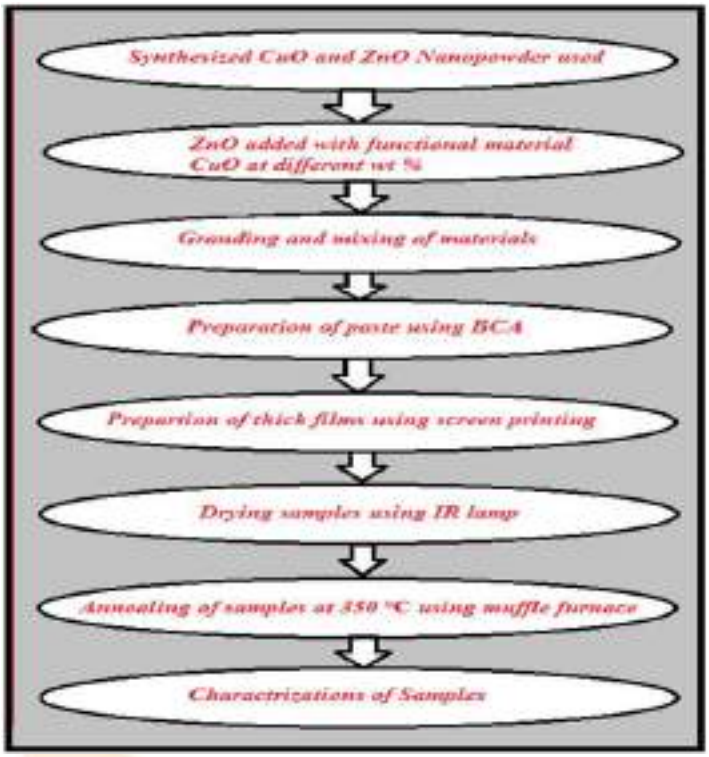

Figure 3: Steps for binary oxide thick film preparation.

2.5 Static system for study electrical and gas sensitivity

The D.C. resistance of the thick films was measured by using half bridge method as a function of temperature in home-built static measurement system as shown in Figure 4. The gas sensing study was also carried out using static gas system to sense H_2S gases. The binary oxide thick films were used as sensing component. The resistance of the sample was measured in an air atmosphere as well as in the presence of gas (at ppm level) of interest at different operating temperatures. The resistance (R_a) of the sample in air and (R_g) in gas atmosphere was measured by using half-bridge method [11-13].

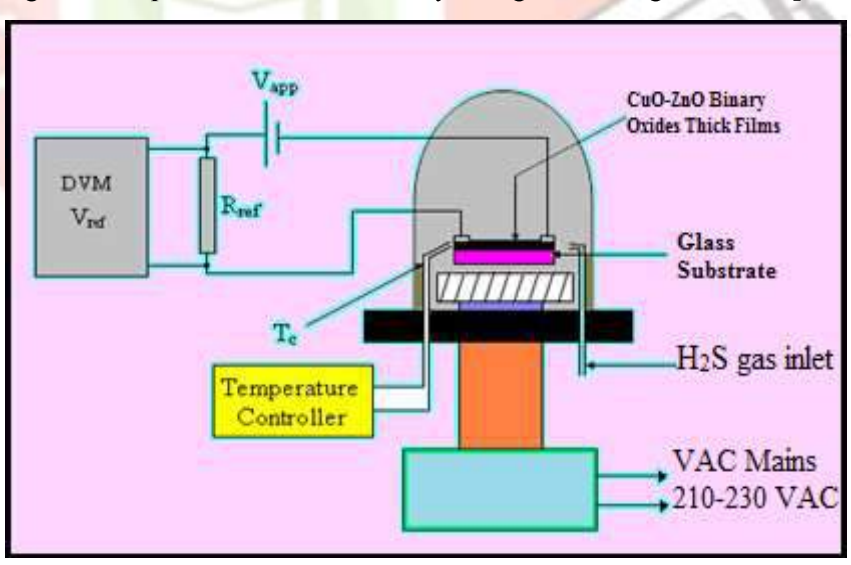

Figure 4: Schematic diagram of electrical and gas sensitivity static system.

2.6 Characterizations of CuO-ZnO binary oxides thick films

2.6.1 Electrical characterizations

2.6.1.1 Resistivity - The resistivity of the films was determined using following equation 1 [11],

$$\rho = \left(\frac{R \times b \times t}{l} \right) ohm - m \quad \text{..... (1)}$$

Where, t = thickness of the film sample, b = breadth of the thick film resistor in cm

2.6.1.2 Activation energy - The activation energy of thick film samples is calculated from Arrhenius plot using the equation 2 [11, 12],

$$R = R_o e^{-\Delta E/KT} \quad \text{..... (2)}$$

Where, R_o = the constant, ΔE = the activation energy of the electron transport in the conduction band (eV), K = Boltzman constant and T = Absolute temperature.

2.6.1.3 Temperature coefficient of resistance (TCR) - TCR was calculated by using the equation 3 [12],

$$TCR = \frac{1}{R_o}\left(\frac{\Delta R}{\Delta T} \right) \ /^{O} C \quad \text{..... (3)}$$

Where,

ΔR = change in resistance between temperature T_1 and T_2, ΔT = temperature difference between T_1 and T_2 and R_o = Initial resistance of the film sample.

2.6.2 Structural characterizations

The developed thick films were characterized by SEM, EDAX and XRD to study the surface morphology, elemental composition analysis and structural properties respectively. The thickness of the thick films was measured by using Taylor-Hobson (Taly-step UK) system. The thickness of the films was observed in the μ m range [11].

2.6.2.1 Scanning Electron Microscopy (SEM) - It is convenient technique to study surface morphology. Scanning Electron Microscopy (SEM) {Model JOEL 6300 LA GERMANY} was utilized to characterize the surface morphology. The magnifications of all SEM images are taken at 5000X. Average particle size and diameter of nanoparticles were determined using Image-J software of SEM images of thick films. The specific surface area of thick films was calculated using BET method for spherical particles using the equation 4 [12].

$$S_w = \frac{6}{\rho d} \quad \text{……..} \quad (4)$$

2.6.2.2 Energy dispersive X-Ray analysis (EDAX) – It is powerful analytical technique which provides X-ray distribution images, line scans and point analysis of trace elements of micro-volumes. EDAX give ratio of expected compounds of the elements present in the film. First, the entire sample was scanned for SEM and then the elements were detected by EDAX. The elemental analysis was carried out carried out using energy dispersive X-ray spectrometer EDAX (JOEL-2300, Germany). The specimen image can be

obtained along with the elemental analysis of the selected area/features and distribution of selected elements.

2.6.2.3 X-ray diffraction (XRD) – XRD tool was used to determine the crystalline structure and preferential orientation of the crystallite material and also to determine the crystallite size. For thick films low angle XRD was used X-ray generator [Miniflex Model, Japan] Rigaku diffractometer (DMAX-500) was employed. The XRD gives d values which were used for identification of different phases and corresponding structure of the material present in the developed films. The experimental (observed from X-ray data) d values are compared with the standard data (JCPDS/ASTM data files). 2θ was carried out to examine the final compositions of the CuO-ZnO nano composite binary oxides thick films. The crystallite size (D) was estimated by Debye Scherer's formula equation 5 [11, 13].

$$D = \frac{0.9\lambda}{\beta Cos\theta} \qquad \text{..... (5)}$$

Where, β = Full angular width of diffraction peak at the at half maxima peak intensity.

λ =wavelength of X-radiation.

2.7 Investigate gas sensitivity

The H_2S gas response of thick films was studied in test assembly. The electrical resistances of nano composite binary oxide thick film in air (*Ra*) and in the presence of H_2S gas (*Rg*) were measured to find the sensitivity (*S*) given by the equation,

$$S\% = \frac{Ra-Rg}{Ra} \times 100 \qquad \text{..... (6)}$$

Where, Ra is the resistances of the CuO-ZnO thick film in air and Rg is the resistances of the CuO-ZnO thick film in gas atmosphere.

3. Result and Discussion

3.1 Electrical Characterization

3.1.1 Resistivity

Resistance determines using home built characterization system. The DC resistance of films was determining by using half bridge method. Readings of temperature verses voltage were taken with the interval of 10°C temperature. The operating temperature range of thick films was 30°C to 350°C. The resistance of nano composite binary oxide thick films decreases with increase in temperature. This confirms the semiconductor behavior of ZnO: CuO nano composite binary oxide thick films by obeying $R= R_0e^{-\Delta E/KT}$ in the 30 °C to 350 °C temperature interval [11- 14].

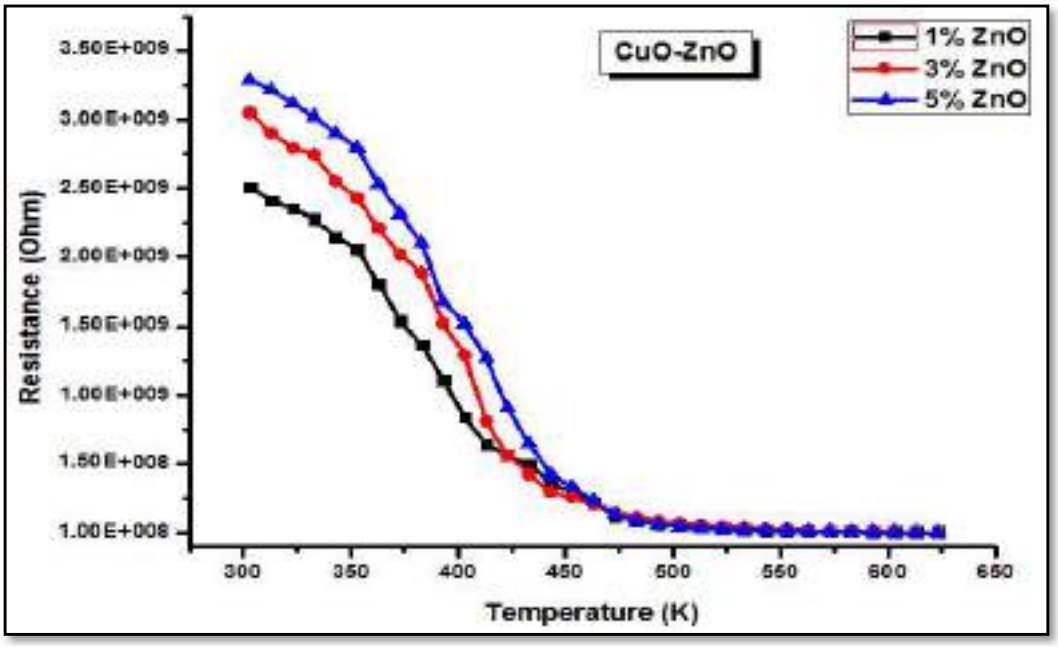

Figure 5 shows the change in resistance of 1 wt. %, 3 wt. %, and 5 wt. % additive (ZnO) added CuO thick film samples with respective change in temperature.

3.1.2 Activation Energy of ZnO: CuO nano composite binary oxide thick films

The activation energies of prepared ZnO: CuO nano composite binary oxide thick films in the low temperature and high temperature films were calculated using Arrhenius plot.

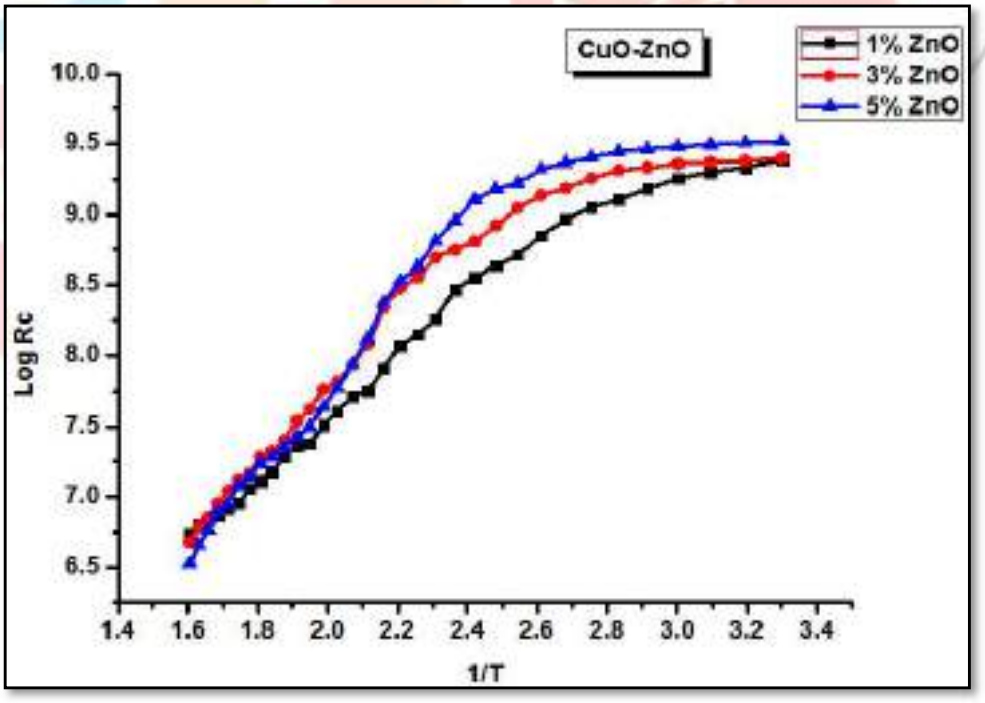

Figure 6 shows Arrhenius plot 1 wt. %, 3 wt. %, and 5 wt. % additive (ZnO) added CuO thick film samples.

In both cases i.e. heating and cooling cycles plot is found to be reversible and obeys the Arrhenius equation.

Table 1: Activation energy of ZnO: CuO thick film.

ZnO additive (wt. %) ZnO: CuO thick films	Activation energy (eV)	
	Low temperature region	High temperature region
1	0.3750	0.0619
3	0.6636	1.4211
5	0.7050	0.9456

The Activation energy for 1 wt. % for ZnO: CuO binary oxide thick film found 0.3750 eV and 0.0619 eV at low and at high temperature respectively. The Activation energy for 3 wt. % for ZnO: CuO binary oxide thick film found 0.6636 eV and 1.4211eV at low and at high temperature respectively. The Activation energy for 5 wt. % for ZnO: CuO binary oxide thick film found 0.7050 eV and 0.9456 eV at low and at high temperature respectively.

3.1.3 TCR of ZnO: CuO nano composite binary oxide thick films

The temperature coefficient of resistance (TCR) of ZnO: CuO nano composite binary oxide thick films are calculated by using equation 3.

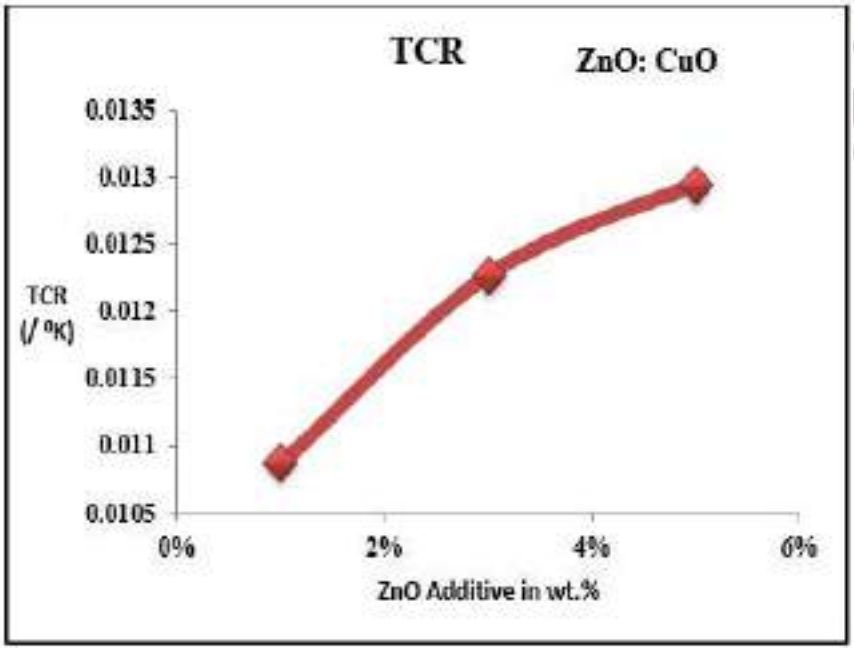

Figure 7: TCR of ZnO: CuO nano composite binary oxide thick films

Table 2: TCR of ZnO: CuO nano composite binary oxide thick films

ZnO additive (wt. %) ZnO: CuO thick films	**CR / ^{0} K**
1	-0.01087
3	-0.01227
5	-0.01294

Temperature coefficient of resistance is found negative to ZnO: CuO nano composite binary oxide thick films samples. The negative sign indicate the semiconductor behavior of the prepared thick films. High resistivity of thick film samples corresponds to a low TCR value [12].

Table 3: Electrical outcomes of ZnO: CuO nano composite binary oxide thick films

ZnO additive (wt. %) ZnO: CuO thick films	**Film Thickness (µm)**	**Resistivity(ρ) (Ω-m)**	**TCR (/°K)**	**Activation energy (eV)**	
				Low temperature region	High temperature region
1	24	30.01 X 10^4	-0.01087	0.7311	0.5999
3	26	40.30 X 10^4	-0.01227	0.7514	0.3825
5	25	41.25 X 10^4	-0.01294	1.2589	0.9543

Table-3 Present electrical characterization of ZnO: CuO nano composite binary oxide thick films sample. Table 3 indicates the different values of thickness and other electrical parameters for each of the ZnO: CuO nano composite binary oxide thick films sample.

3.2 Structural Characterization

3.2.1 SEM analysis of ZnO: CuO nano composite binary oxides thick films

Scanning electron microscopy (SEM) is one of the most popular and widely used techniques for the characterization of nanomaterial's and nanostructures. For the study of ZnO: CuO nano composite binary oxides thick films thick films thick film SEM magnification is 5000. The SEM images show the morphology of ZnO: CuO nano composite binary oxide thick films. wt. % of additive increases the change in surface morphology also found to be increasing in the SEM images. The particles grain size decreases with increases doping percentage of ZnO in the CuO. SEM results indicate the formation of particles with different shapes and sizes. The image shows, larger particles or grain agglomerates. SEM results also show particles have large porosity showing large numbers of voids. These voids are responsible for the adsorption of the gas molecules [15, 16].

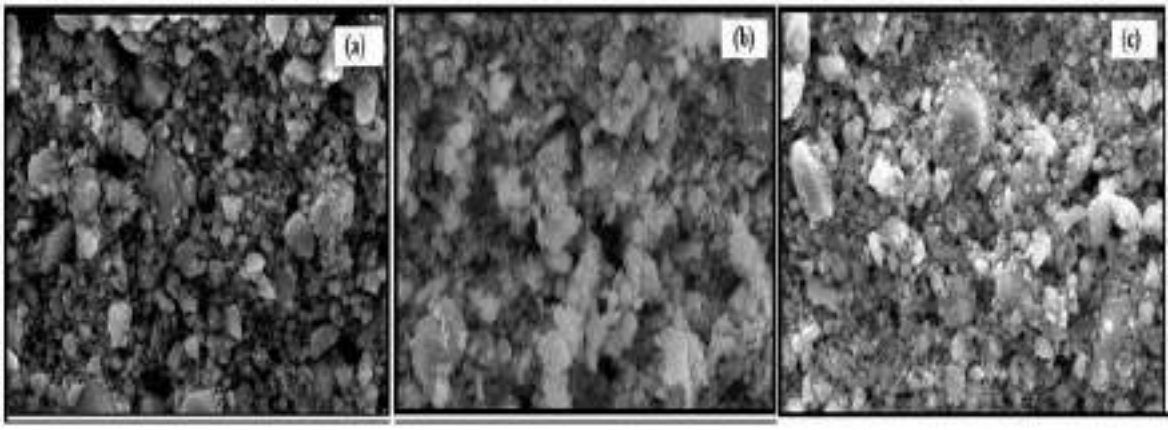

Figure 8 (a), (b) and (c) shows SEM images of 1 wt. %, 3 wt. %, and 5 wt. % additive (ZnO) added CuO thick film respectively.

The 2D images with high magnification were used to study surface morphology of these films. The specific surface area calculated by using SEM images. The diameter (*d*) of ZnO: CuO nanoparticles were measured by using Image J software. The rate of adsorption and desorption increases with large surface area of the films as well as nanoparticles of materials produced maximum chemisorption's. Using BET method, specific surface area of ZnO: CuO nano composite binary oxides thick films were calculated by equation 4 [12, 16].

Table 4: Specific surface area of ZnO: CuO nano composite binary oxide thick films.

ZnO additive wt%	Specific surface area in m^2/g
1%	1.3389
3%	2.2935
5%	2.7796

From above Table 4, it has been observed that the specific surface area of ZnO: CuO nano composite binary oxide thick films.

3.2.2 X-ray diffraction

The hkl parameters of CuO and ZnO match with JCPDS Card 80-1916 and 80-0074 respectively. Hence it clearly found that the structure of CuO is monoclinic and structure of ZnO is hexagonal for all percentage. Prominent peak of XRD found is at 38.71 which indicates [200] for 1wt. %, prominent peak of XRD found is at 35.63 which indicates [111] for 3wt. %, and prominent peak of XRD found is at 38.77 which indicates [111] for 5wt. %, Better crystallinity found because the maximum intensity of prominent peaks. The crystalline nature of the thick film material is confirmed by XRD. Average crystallite size was calculated from XRD pattern and using Debye-Scherrer equation 5 [12]. The crystallite size was found to be as 39 nm, 32 nm and 31 nm for 1 wt. %, 3 wt. %, and 5 wt. % respectively.

X-ray diffraction studies were conducted to understand the crystal structure and phase of ZnO: CuO nano composite binary oxide thick films. The CuKα radiation range is 20˚ to 80˚ for ZnO: CuO nano composite binary oxide samples. Following Figure 9 shows X-ray diffraction pattern obtained for 1 wt. %, 3 wt. %, and 5 wt. % ZnO: CuO thick films.

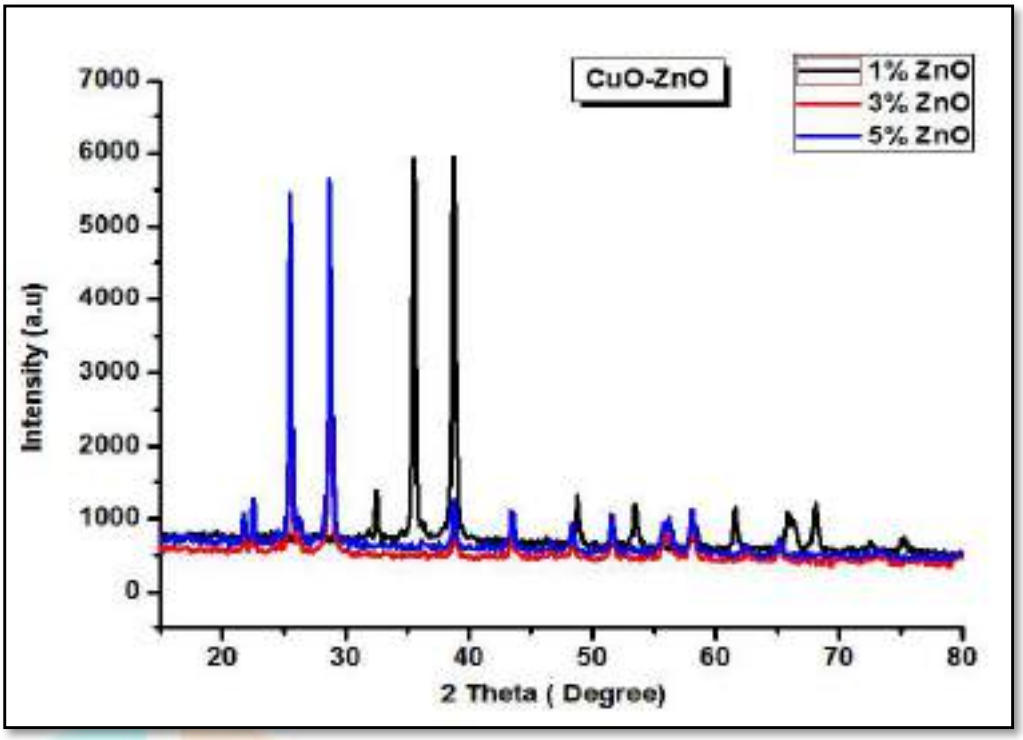

Figure 9**:** X-ray diffraction pattern of ZnO: CuO thick film samples

Table 5: Crystallite size for 1 wt. %, 3 wt. % and 5 wt. % concentration of ZnO added CuO thick film sensors

ZnO additive concentration (wt. %)	Average crystallite size (nm)
1	39
3	32
5	31

3.3. Gas sensing characterization

3.3.1 Study of H_2S gas sensing characterization of ZnO: CuO nano composite binary oxides thick films samples

The prepared ZnO: CuO nano composite binary oxides thick films samples were used as a H_2S gas sensor. Resistance of the film is measured in the form of voltage using half bridge method. This method is applied at different operating temperatures in H_2S gas atmosphere for ZnO: CuO nano composite binary oxides thick films samples. The H_2S gas was injected with different concentration level in ppm at normal atmospheric conditions.

3.3.2 Sensitivity on operating temperature with different concentration of H_2S gas in ppm.

The H_2S gas sensing behavior of ZnO: CuO thick films were studied by using home-built static measurement system. The ZnO: CuO nano composite binary oxides thick films sample resistance was measured by using half bride method with temperature in the H_2S gas atmosphere.

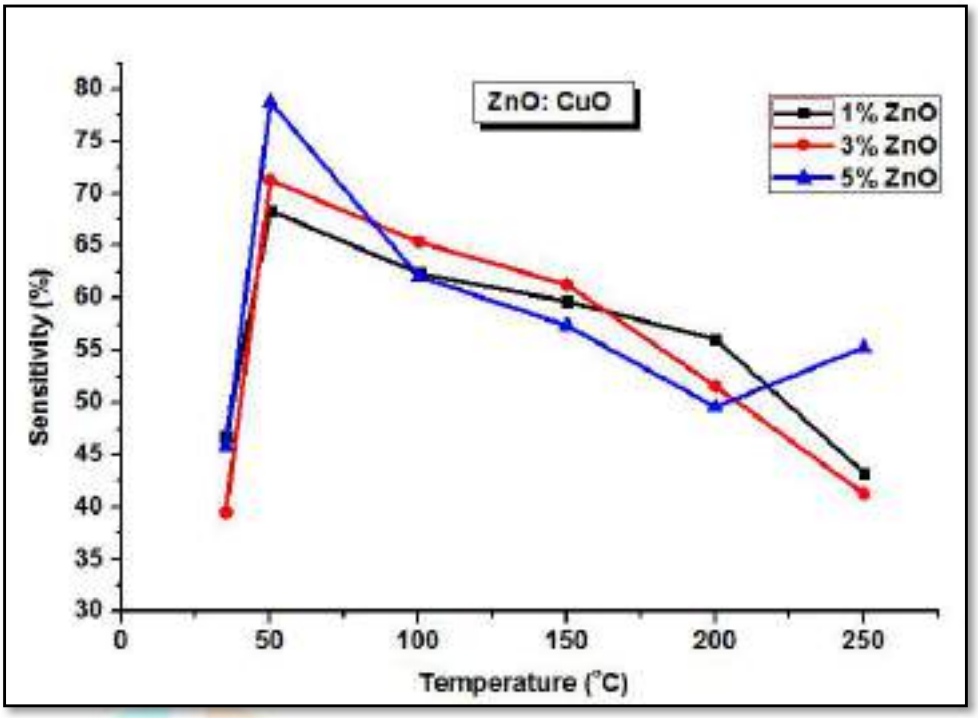

Figure 10: Sensitivity of ZnO: CuO nano composite binary oxides thick films sample

Time interval of operating temperature is 50°C during the measurement of gas response. For measurement of H_2S gas sensitivity the temperature range varied from room temperature (35°C) to 250°C. The gas sensitivity of the ZnO: CuO nano composite binary oxides thick films sample were calculated using equation 6. The concentration of H_2S gas in the current gas sensing study were taken in part per million (ppm). Here four concentrations 100 ppm, 200ppm, 500ppm and 1000 ppm of H_2S gas were used. Figure 10 shows the variation of % sensitivity for 1 wt. %, 3 wt. %, and 5 wt. % additive (ZnO) added CuO thick film samples. The 5% ZnO doped CuO binary oxide thick films shows maximum sensitivity of 78.8% sensitivity to 100 ppm of H_2S gas at operating different temperature 50^0 C.

3.3.3. Response time and recovery time of ZnO: CuO nano composite binary oxides thick films sample

The thick film sensor is kept at 50^0C optimum temperature. Then, H_2S gas is insert using syringe in the glass dome of the gas sensing system for measurement of response time.

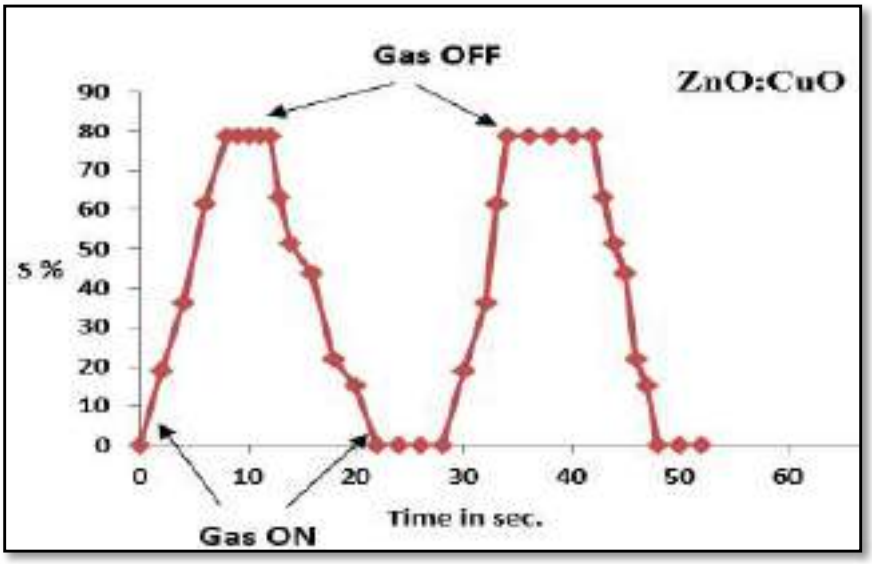

Figure 11 Response and recovery time of ZnO: CuO binary oxide thick film

From the time plot it is found that response time is 09 seconds whereas recovery time is 20 seconds to ZnO: CuO binary oxide thick film for H_2S gas at concentration 100 ppm and at 50 ^oC optimum temperature.

3.3.4 H_2S gas sensing mechanism for ZnO: CuO nano composite binary oxides thick film sample

ZnO is n-type semiconductors and CuO is a p-type semiconductor. Addition of ZnO into CuO makes ZnO: CuO nanocomposites binary oxide causes create p-n hetero junction that will promote high electrical resistance in the air [15, 16]. After exposure to H_2S gas, CuO is concerted into CuS phase shown in following reaction-

$CuO + H_2S = CuS + H_2O$

The effect of this reaction drastic increase electrical conductance result in decreases resistance of the film. The increase in percentage of ppm of Hydrogen gas sulfur atomic fraction increases which enhanced the sensitivity of the film because Cu decreases in these reaction and effect in change the resistance [17, 18].

References:

1. Anukunprasert, T., C. Saiwan, and Enrico Traversa. "The development of gas sensor for carbon monoxide monitoring using nanostructure of Nb–TiO2." *Science and Technology of Advanced Materials* 6.3-4 (2005): 359-363.
2. Eranna, G., et al. "Oxide materials for development of integrated gas sensors—a comprehensive review." *Critical Reviews in Solid State and Materials Sciences* 29.3-4 (2004): 111-188.
3. Balaguru, R. John Bosco, and B. G. Jeyaprakash. "Mimic of a gas sensor, metal oxide gas sensing mechanism, factors influencing the sensor performance and role of nanomaterials based gas sensors." *NPTEL–Electrical & Electronics Engineering–Semiconductor Nanodevices* (2004): 1-30.Sahm, T., et al. "Flame spray synthesis of tin dioxide nanoparticles for gas sensing." *Sensors and actuators B: Chemical* 98.2-3 (2004): 148-153.
4. Wang, Chengxiang, et al. "Metal oxide gas sensors: sensitivity and influencing factors." *sensors* 10.3 (2010): 2088-2106.
5. Dey, Ananya. "Semiconductor metal oxide gas sensors: A review." *Materials Science and Engineering: B* 229 (2018): 206-217.
6. Zhang, Jian, et al. "Metal-oxide-semiconductor based gas sensors: screening, preparation, and integration." *Physical Chemistry Chemical Physics* 19.9 (2017): 6313-6329.
7. Fine, George F., et al. "Metal oxide semi-conductor gas sensors in environmental monitoring." *sensors* 10.6 (2010): 5469-5502.
8. Bochenkov, V. E., and G. B. Sergeev. "Sensitivity, selectivity, and stability of gas-sensitive metal-oxide nanostructures." *Metal oxide nanostructures and their applications* 3 (2010): 31-52.
9. Bochenkov, V. E., and G. Bochenkov Sergeev. "Metal oxide nanostructures and their applications." *American Scientific Publishers* 3 (2010): 33.
10. Liu, Xiao, et al. "A survey on gas sensing technology." Sensors 12.7 (2012): 9635-9665.

11. Patil, Arun, et al. "Effect of Cr2O3 by Doping and Dipping On Gas Sensing Characteristics of ZnO Thick Films." *Journal of Electron Devices* 15 (2012): 1274-1281.

12. Tupe, U.J., Zambare, M.S., Patil, A.V. and Koli, P.B., 2020. The Binary Oxide NiO-CuO Nanocomposite Based Thick Film Sensor for the Acute Detection of Hydrogen Sulphide Gas Vapours. *Material Science Research India*, *17*(3), pp.260-269.

13. Li, Dan, et al. "Preparation and gas-sensing performances of ZnO/CuO rough nanotubular arrays for low-working temperature H2S detection." *Sensors and Actuators B: Chemical* 254 (2018): 834-841.

14. Kim, Jaehyun, Wooseok Kim, and Kijung Yong. "CuO/ZnO heterostructured nanorods: photochemical synthesis and the mechanism of H2S gas sensing." *The Journal of Physical Chemistry C* 116.29 (2012): 15682-15691.

15. Park, Sunghoon, et al. "Enhanced H2S gas sensing performance of networked CuO-ZnO composite nanoparticle sensor." *Materials Research Bulletin* 82 (2016): 130-135.

16. Wang, Xu, et al. "Low-temperature and highly sensitivity H2S gas sensor based on ZnO/CuO composite derived from bimetal metal-organic frameworks." *Ceramics International* 46.10 (2020): 15858-15866.

17. Nagarjuna, Yempati, and Yu-Jen Hsiao. "CuO/ZnO Heterojunction Nanostructured Sensor Prepared on MEMS Device for Enhanced H2S Gas Detection." *Journal of The Electrochemical Society* 168.6 (2021): 067521.

18. Vuong, Nguyen Minh, et al. "CuO-decorated ZnO hierarchical nanostructures as efficient and established sensing materials for H2S gas sensors." *Scientific reports* 6.1 (2016): 1-13.

IJCRT.ORG ISSN : 2320-2882

INTERNATIONAL JOURNAL OF CREATIVE RESEARCH THOUGHTS (IJCRT)

An International Open Access, Peer-reviewed, Refereed Journal

Review on: Synthesis of Perovskite using Sol-Gel approach

Ejaz Nazir Shaikh[1*], Umesh. J. Tupe[2], Arun V. Patil[3], Chandrakant. G. Dighavkar[4].

[1-3]Research Centre in Electronic Science and Department of Electronic Science,

[1]Loknete Vyankatrao Hiray Arts, Science and Commerce College Panchavati, Nashik, ndia.

[2]Department of Electronic Science, VADP's Arts, Science & Commerce College, Shirsondi, Tal - Malegaon, Dist-Nashik, Affiliated to SPPU, Pune, Maharashtra – 423208, India.

[3]Department of Physics, MGV's, Arts, Science and Commerce College, Manmad, Dist. Nashik 423104, India

[4]Departmet of Physics, MGV's, Arts, Science and Commerce College, Surgana, Dist. Nashik 422211, India

Abstract:

Lead halide perovskites have emerged as one of the leading photovoltaic materials due to their long carrier lifetimes, high absorption coefficients, high tolerance to defects, and facile processing methods. Which makes them now already comparably efficient to silicon-based photovoltaics. High efficiency, flexibility, and cell architecture of the emerging hybrid halide perovskite have caught the attention of researchers and technologists in the field. This article provides a comprehensive review on characteristics of perovskite materials; pervoskite material preparation and synthesis method and recent progresses are reported. Sol-Gel is a low cost, well-established and flexible synthetic route to produce a wide range of micro- and nanostructures. Small variations in pH, temperature, precursors, time, pressure, atmosphere, among others, can lead to a wide family of compounds that share the same molecular structures. In this work, we present a general review of the synthesis of $LaMnO_3$/ $LaCrO_3$based on Sol-Gel approach.

Keywords **-** Perovskite,Sol-Gel, nanoparticles, specific surface area, $LaMnO_3$ / $LaCrO_3$.

1. Introduction:

Every day, conventional, non-renewable fossil fuels energyconsumption rapidly increaseswhich causes humiliation of the environment through global warming, acid rains, increase in carbon dioxide content in the environment, smogetc. Eco-friendly energy resources such as solar, wind and tidal, and hydropower make best replacement for the fossil fuels so that, the utilization of conventional energy source can be avoided. Solar photovoltaic technology is one of the emerging renewable technologies.Recently, an emerging Photovoltaic solar cells based on organometal halide perovskite

materials which provide high efficiency and stability with low cost becomes attractive alternative to conventional photo voltaic Solar cell. The perovskite material has ability to achieve power conversion efficiency close to Cadmium Telluride (CdTe). The efficiency of methyl ammonium lead halide perovskite sensitized solar cells advancement from 3.8% to 22.1% within a very short period of research and development [1].

Perovskites shows diversity of electric, optical, and magnetic properties. Perovskite oxides shows variety of electrical properties and a variety of solid-state phenomena from insulating, semiconducting, metallic, and superconducting characters. Therefore, they are very interesting to be studied and applied in a large scale. The family of perovskite material consists large number of oxide forms, such as transition metal oxides with the general formula of ABO_3. The oxide perovskite materials are broadly synthesized and studied for wide applications in different technological fields.

Pervoskite was initially discovered by German geologist Gustav Rose in 1839 in Ural Mountains, and named after Russian mineralogist Lev A.Perovski, Lev Perovskihad discovered a cubic crystal structure with chemical composition $CaTiO_3$. This structure was named calcium titanium oxide ($CaTiO_3$) which had calcium ion (Ca^{2+}) at the corners, titanium ion (Ti^{2+}) BCC (body cubic-centred) and oxygen (O^{2-}) at the FCC (face cubic-centred) in a cubic crystal. Between both the cation, i.e. calcium and titanium, calcium ion was bigger in size. Perovskites exhibit general configuration ABX_3 which represents A as cation of bigger size, B as cation of smaller size, whereas X represents negative ion mostly of oxygen or halogens. In perovskites crystals, cation A is located between BX_6 octahedron connected through apex angle while cation B, possessing six fold coordination, is surrounded by an octahedral of anions [2,3].In 1926, V. M. Goldschmidt, who was the first which synthesize and study perovskites materials, which were $CaTiO_3$, $NaNbO_3$, $SrTiO_3$, and $BaTiO_3$. In 1986, high temperature superconductivity in ceramics and perovskites was discovered by J. G. Bednorz and K. A. Muller [4,5].

2. Overview of Perovskite materials :

The chemical formula of perovskite material must have neutral balanced charge; therefore, the sum of total charges at A and B sites cations must be equal to total charges at O site (oxygen) of anion(s). A suitable charge distribution is to be achieved in the forms of A^{3+} B^{3+} O^3 or A^{4+} B^{2+} O^3 or A^{1+} B^{5+} O^3.

Based on ionic size limitations for the required cations and anions, a stability and formability range for ABX_3 perovskite with a cubic crystal structures can be achieved byfollowing fundamental requirement, which are given as: The average ionic radii of A- and B-sites cations must be greater than 0.90 Å and 0.51 Å, respectively, and The value of tolerance factor must be lies in the range of 0.88–1.09.If the tolerance factor equal to unity i.e., t = 1.0 then it is indication ofideal perovskite crystal [6,7].

To form a perovskite structure, radius of ions A, B and X must obey the following rules:

$$\text{Rule of Tolerance Factor (TF):}\quad 0.81 < TF = \frac{RA+RX}{\sqrt{2}(RA+RX)} < 1.110$$

$$\text{Rule of octahedral factor (OF):}\quad 0.44 < \mu = \frac{RB}{RX} < 0.9$$

Where,

RA, RB and RX are ionic radii for A, B and X ions, respectively.

Following figure 1, shows structure of an ideal ABX_3- type perovskite with a cubic crystal structure.Where A and B are cations with different electronegativity and size while X is an anion that is bonded to both A and B. It is important that,an atom has lower electronegativity and bigger atomic radius than atom B, due to symmetrical purposes of the crystal cubic structure. Any material with same crystal structure is called perovskite material. Depending on cations and anion they exhibit different properties like super conductivity, ionic conductivity, high thermal power etc..[8-10]

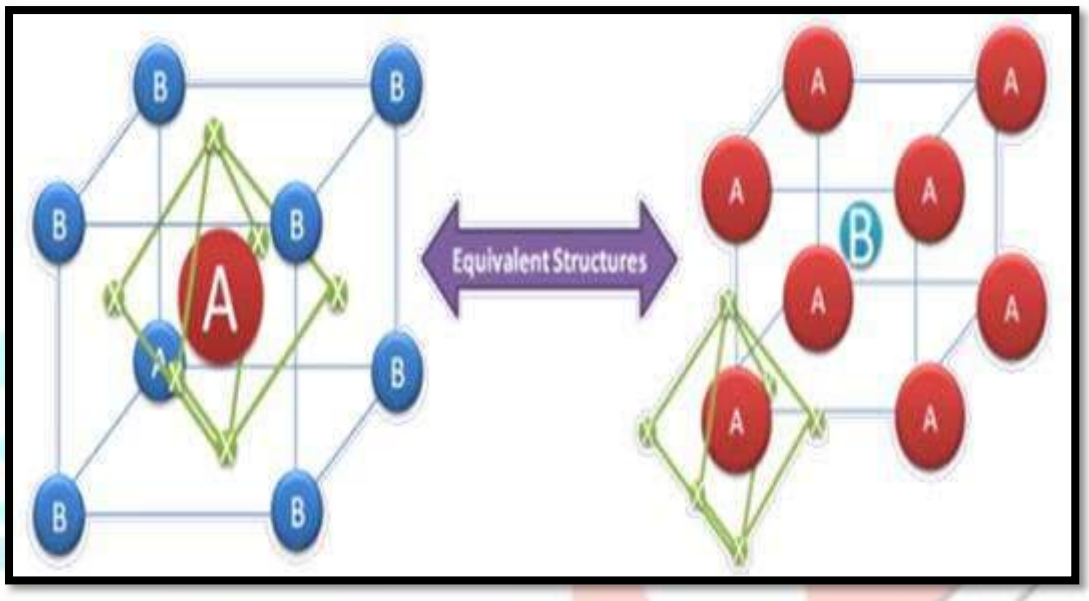

Figure 1: The generals perovskite cubical crystal structure ABX_3,

Where, Aand B are cations and X is an anion.

3. Synthesis methods of perovskite material:

There are various methods are reported to synthesis of the perovskites structure which are: solid state reaction, co-precipitation, hydrothermal, alkoxide hydrolysis, metal-organic processing, sol-gel, electro spinning, electrochemical, microwave synthesis, physical vapour deposition, molecular beam epitaxial, the Pechini process, chemical vapour deposition, chemical solution deposition, Combustion Methodetc.[11-14].

Athayde, D. Souza, D.F. Silva, A. Vasconcelos, D. Nunes, E.H. da Costa, J.C.D. reported that, Alkoxide, alkoxide-salt, and Pechini methods are the most popular Sol–Gel-based techniques used in the synthesis of perovskites. Sol-Gel method is one of the simplest techniques to synthesize high-quality nano and microstructures. The Sol-Gel Pechini method became the most used due to its versatility in preparing perovskite membranes, depositing dielectric films for the production of capacitors and multicomponent oxide materials. Sol-Gel is a low cost, well-established and flexible synthetic route to produce a wide range of micro- and nanostructures. Small variations in pH, temperature, precursors, time, pressure, atmosphere, among others, can lead to a wide family of compounds that share the same molecular structures. [15].

3.1Sol-gel method:

The Sol-gel method is frequently used to synthesize nanomaterials. High stability and selective sensitivity of ABO_3-type perovskite materials have an advantage that could be controlled by selecting suitable A and B atoms or by chemical doping. NiTiO3, CoTiO3, BaZrO3, LaMnO3, MnTiO3, PbTiO3 are some examples of common perovskite oxides. The Sol-gel process is one of the techniques among several reported techniques for preparation of perovskite materials. It is an appropriate technique for synthesis of dense nanomaterials with homogeneous texture and uniform morphology [60-61].

Parashar, M. Shukla, V.K. Singh, R. et. al. [16] describe that The Sol-Gel method involves the use of a colloidal solution (Sol) that evolves into a gel-like network including both a liquid and a solid phase as a result of several chemical reactions. It can be divided into two types: aqueous or hydrolytic and non-aqueous or non-hydrolytic. The aqueous Sol-Gel process can be described in five steps: hydrolysis, condensation, aging, drying and crystallization.

Sol-gel process gel is a chemical route used to synthesize glassy or ceramic materials at relatively low temperatures, based on wet chemistry processing, which involves the preparation of a sol, the gelation of the sol and the removal of the liquid existing in fine interconnected channels within the gel. It is combination of physical and chemical processes which includes following processes hydrolysis, condensation, polymerization, gelation, drying, and densification etc. The principle of Sol-gel method is based on a compound reaction between metal cations and a chelating agent (such as citric acid, or ethylene glycol also ethylenediaminetetraacetic acid (EDTA), oxalic acid, tartaric acid or glucose). The molar ratio for metal ions and chelating agent should be 1:1. It shows high reproducibility and an enhanced degree of homogeneity of the reaction mixture. In this method metal alkoxides as starting material, which is derivative of the alcohol ROH, where R is an alkyl group or a derivative of metal hydroxide M(OH)x. The stoichiometric amounts of metal alkoxides dissolved in alcohol or distilled water at a temperature of 60–80°C under constant stirring. pH value of the metal alkoxides solutions must be control to avoid the formation of the precipitation and the homogeneous gel which can be carried out using basic or acidic solutions. It is called hydrolysis and condensation,which brought out formation of polymer chain. The polymer chain improve the viscosity of reaction mixture and produces gel. Then produced gel were beaten and grinded, and then calcined for 5-6 hours at 550^0 C to obtain the pure materials[17-18]. Figure 2, reveals that the different stage of sol-gel method

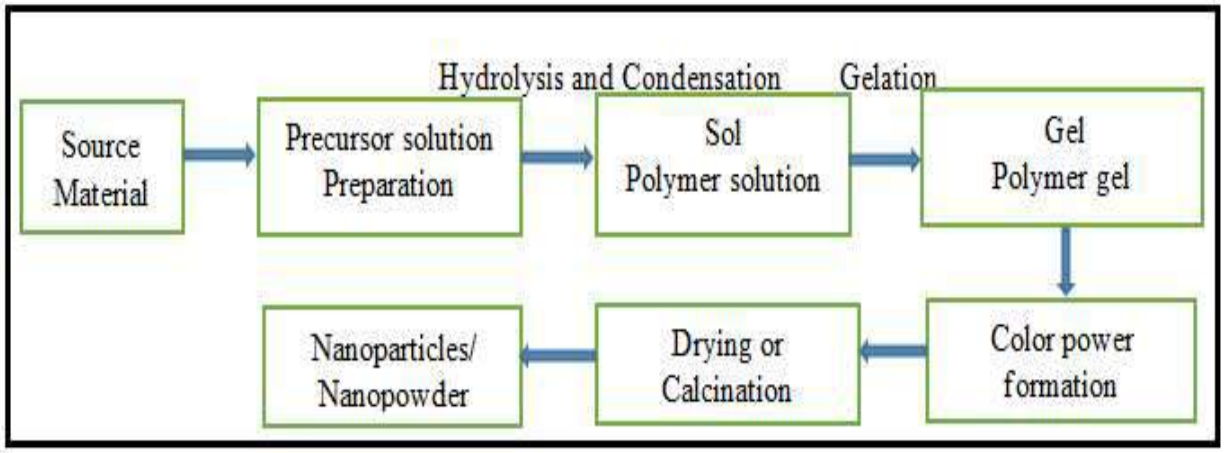

Figure 2: different stage of sol-gel method

Pechini, M.P.et al. [19]. reported that, the most significant advantages of Sol-Gel Pechini method process is its simplicity and the low-temperature precursor handling. This results in the fabrication of nanopowders with excellent purity and uniformity, as well as precise control of the final composition of the material. This method is also a popular choice for the synthesis of various mixed oxides due to its capacity to combine chemicals (such as lactic, glycolic, citric, and EDTA acids) leading to the creation of polybasic acid chelates with dissolved cations.

Kurajica, S. et al. [20] reported that, Chelating agents are employed to prevent et. al. partial metal segregation in the final compound, which might occur as a result of various interactions between metal ions in the solution. The polyesterification of chelates occurs when a polyhydroxy alcohol is added to the solution and heated, resulting in a cross-linked chain of metal atoms connected to organic radicals. When two chelating agents work together to complex all metal ions, a precursor solution is formed with all metal ions entirely bound. As a result, a more stable chelate complex system develops and the polymerization is aided by the following addition of ethylene glycol, which enhances uniformity. This method tends to reduce metal segregation after decomposition under heat treatment settings. In the synthesis process and subsequent heat treatment, the ratio of metal precursors to chelating agents is critical. In theory, this ratio should be high enough to ensure that all metal ions are tightly bound to their structures and prevents precipitates in the solution. The Sol-Gel Pechini method offers an excellent control over perovskite structure producing very homogeneous solutions. At temperatures near 1000 ◦C, this approach results in the creation of pure crystal perovskite structure [21].

Shinde, V.S. Kapadnis, K.H. Sawant, C.P. Ahiraro, A.N.et. al. [22] synthesized $LaCrO_3$ by sol-gel method. For this synthesis intiallyhydrolyze 3.03 g lanthanum nitrate [$La(NO_3)_3$], 3g chromium nitrate [$Cr(NO_3)_3$] in optimum distilled water,and1.72g citric acid in different beaker. Both solutions are mixed and then heated at 80^0C with constant stirring on magnetic stirrer to evaporate distilled water for minimum 2- 3 hours. During process of stirring a homogeneous viscous gel were obtained having dark greyishcolour. This gel get initially dried under IR lamp for 1-2 hours. Then rough particles were beaten and grinded, and then calcined for 5-6 hours at 550^0 C. finally, pure material of $LaCrO_3$ obtain in greyishcolour.

Pechini, M.P.et. al. [19]reported that, $LaMnO_3$ is a perovskite with the general formula ABO_3. Each B atom occupies the vertex of the perovskite lattice and six oxygen atoms surround it to form an octahedron. The A element occupies the center of eight octahedrons. The oxidation state of B cation can be modulated by varying preparation steps during the perovskite synthesis, such as temperature, non-stoichiometry of cations A or B or substituting La^{3+} by lower oxidation state cations, such as Ca^{2+}, Ba^{2+} or Sr^{2+}, or even higher oxidation state cation such as Ce^{4+}. Sol-Gel technique is one of the easiest and most efficient methods to synthesize different $LaMnO_3$ nanoparticles.

Liu et. al. [27] synthesised $LaMnO_3$ of high surface area using citric acid and ethylenediaminetetraacetic acid (EDTA) as chelating agents. They found that EDTA-citrate produced smaller nanoparticles than the single citrate acid. The samples exhibited a high specific surface area showing excellent oxygen reduction and evolution reaction catalytic performance.

Shaterianet. al. [28] synthesised $LaMnO_3$ nanoparticles via Sol-Gel process using stearic acid as complexing reagent. The as-synthesized nanoparticles showed pure perovskite structure which presented a rhombohedral structure with average particle sizes of 20–30 nm.

Onrubia-Calvo et. al. [29] synthesised a series of Sr-doped $La_{1-x}Sr_xMnO_3$perovskites (x = 0.1, 0.2, 0.3, 0.4 and 0.5) by varying citrate to nitrate molar ratio in the starting solution, pH and calcination protocol.

ChaozhuShuet. al. [30] used a facile nonstoichiometric strategy to introduce A-site cationic vacancies in $LaMnO_3$, $La_{0.9}MnO_3$, $La_{0.7}MnO_3$, perovskite oxides were synthesized by combining Sol-Gel method and thermal treatment process in air. This procedure provides the advantage of great specific surface area and abundant cationic La vacancies on the surface, $La_{0.7}MnO_{3-\delta}$ ($L_{0.7}MO$) can provide effective active sites for oxygen electrode reactions and a large storage space for Li_2O_2 accommodation.

Amador, C.; Martin de Juan, L et. al. [31] reported that, the specific surface area (SSA) plays an important role in the synthesis processes. Depending on the preparation method of the pervoskite material, the porosity, size and shape of pores and the pore distribution are impressively distinct. The comparative study of pervoskite material, synthesis method and specific surface area are mentioned in following Table 1.

Table 1: Comparison of sol gel and other synthesis approaches w.r.to specific surface area

Perovskite Material	Preparation Method	specific surface area (SSA) in (m^2/g)	References
$LaCoO_3$	Solid-state synthesis	3.0	34
$LaCoO_3$	Sol-gel Method	15.0	37
$LaCoO_3$	Combustion method	5.7	39
$LaCoO_3$	Co-precipitation	8.0	38
$LaMnO_3$	Solid-state synthesis	4.0	34
$LaMnO_3$	Sol-gel Method	22.0	36
$LaMnO_3$	Combustion method	21.8	41
$LaMnO_3$	Co-precipitation	11.0	40
$LaFeO_3$	Solid-state synthesis	3.1	34
$LaFeO_3$	Sol-gel Method	16.5	32
$LaFeO_3$	Combustion method	9.3	32
$LaFeO_3$	Co-precipitation	5.4	32
$BaTiO_3$	Solid-state synthesis	0.4	35
$PbTiO_3$	Solid-state synthesis	0.5	35
$LaAlO_3$	Sol-gel Method	4.0	36
$LaAl_{0.6}Mn_{0.4}O_3$	Sol-gel Method	25.0	36
$LaAl_{0.4}Mn_{0.6}O_3$	Sol-gel Method	26.0	36
$LaNiO_3$	Solid-state synthesis	4.8	34
$LaCuO_3$	Solid-state synthesis	0.6	34
$NdMnO_3$	Sol-gel Method	20.0	43
$SmMnO_3$	Sol-gel Method	19.0	43
$NdFeO_3$	Sol-gel Method	2.3	44
$SmFeO_3$	Sol-gel Method	4.3	44
$PrCoO_3$	Co-precipitation	5.1	42
$NdCoO_3$	Co-precipitation	1.6	42

$GdCoO_3$	Co-precipitation	2.1	42
$LaCrO_3$	Solid-state synthesis	1.9	42
$LaCrO_3$	Sol-gel Method	5-7	33
$LaCr_{0.5}Mg_{0.5}O_3$	Sol-gel Method	6.08	33
$LaCr_{0.5}Mg_{0.5}O_3 \cdot 2MgO$	Sol-gel Method	13.6	33
$LaCr_{0.5}Mg_{0.5}O_3 \cdot 6MgO$	Sol-gel Method	24.2	33

The specific surface area of the perovskite is strongly affected by which preparation method to be used. From above table.2 it is conclude that, the highest surface areas mainly obtained by sol-gel better than other synthesis methods. Sol gel method provide better control of the structure, including porosity and particle size; possibility of incorporating nanoparticles and organic materials into sol-gel-derived oxides. Also sol gel method allows the fabrication of any oxide composition, but also some non-oxides, as well as the production of new hybrid organic-inorganic materials, which do not exist naturally. It provide high purity due to mixing at the molecular level. It does not requirespecial or expensive equipment.

4. Characterization of perovskites:

Lozano-Gorrín, A.D [45], and Abd Al-Rahman [46].Reported that, Phase and purity of synthesized nanoparticles plays very important role for the conclusion about the properties exhibited by the nanoparticles. Hence X-ray diffraction technique to identify the phase of perovskites. Phase purity of synthesized pervoskite can beidentify by matching the XRD pattern of the synthesized material with the standard XRD pattern of the cubic phase of $CaTiO_3$ perovskite, Relative phase fractions of different phases present, lattice constants, unit cell volume, crystallite size, lattice strain, and theoretical density in the prepared nanoparticles can easily recognize by XRD data. Also FTIR (Fourier-transform infrared spectroscopy) used to identify chemical bonding and chemical structure of the prepared perovskites, FTIR can give structural confirmation which is similar to that obtained through XRD. Thermal stability and decomposition temperature of the prepared perovskites can be characterized by using thermal analysis techniques like Thermogravometric analysis (TGA), Differential thermal Analysis (DTA), and Differential scanning calorimetry(DSC).Scanning electron microscopies (SEM) and transmission electron microscopies (TEM) can be used to recognize the different morphological and surface characteristics of the synthesized perovskites.Measurement of the specific surface area of the prepared materials become important because, electrochemical performance and electro catalytic activity of the perovskites are mostly related with the specific surface area of the materials. Hence surface area values of synthesizedperovskites can be measured by Brunauer–Emmett–Teller (BET) nitrogen adsorption. XPS (X-ray photoelectron spectroscopy) also used to identify surface compositions of the various components of the prepared perovskites.

Shinde, V.S. Kapadnis, K.H. Sawant, C.P. Ahiraro, A.N. et. al. [22]. Synthesized the synthesis of $LaCrO_3$ nanoparticles dopped with Yetrria by sol-gel technique, This is a very simple and cost effective method, also their thick film preparation by screen printing method and their characterization done by XRD, SEM, EDS and IR spectroscopy. The prepared nanoparticles were characterized by XRD from

which the average crystallite size calculated by Scherer's formula found to be 24.66nm. The SEM spectrum shows greyish black surface of lanthanum oxide nanoparticles. The EDS of $LaYCrO_3$ nanomaterial shows the elemental composition of prepared nanoparticles. The infrared spectrum analyze the typical IR stretching frequencies of La-O and Cr-O found to be 590.22 cm- and 447.49 cm- respectively.

Gosavi, P.V. Biniwale, R.B. et al. [47]. Synthesized LaFeO3 using sol-gel, combustion, and co-precipitation and measured the surface area and the average pore diameter of the prepared perovskites. They reported that, the surface area and Average pore diameter of the prepared $LaFeO_3$ as shown in Table 2 below.

Table 2: The Specific Surface area and Average pore diameter of the prepared $LaFeO_3$ for different synthesis methods.

Perovskite Material	**Preparation Method**	**specific surface area (SSA) in (m^2/g)**	Average pore diameter in A°
$LaFeO_3$	Sol-gel Method	16.5 m^2/ g	119 °A
$LaFeO_3$	Combustion Method	9.3 m^2/ g	140 °A
$LaFeO_3$	Co-precipitation Method	5.4 m^2/ g	205 °A

From above table it is observed that,Sol-gel and combustion methods resulted in higher porous surface with large internal pores contributing to higher surface area, while co-precipitation method resulted in less internal pores and lower surface area due to longer calcination time.

Situmeang, Rudy &Sembiring, Simon &Simanjuntak, Wasinton&Sembiring, Zipora&Yuwono, Suripto. et al. [56]. Synthesis $LaCrO_3$ nanomaterial is using simultaneously the sol–gel and the freeze-drying method. Nitrate salts of lanthanum and chrome are dissolved in a pectin solution. The sample is thoroughly stirred using a magnetic stirrer while adjusting pH to 11 until a gel is formed. After the freeze-drying process, the precursors are subjected to a calcination treatment at 600°C, 700°C, and 800°C and subsequently characterized by X-ray diffraction (XRD), TEM and DRS analysed. The results verify that a major crystalline phase of $LaCrO_3$ perovskite is formed as the temperature of calcination increases. The crystallites size identification using the Scherrer equation shows that the size increases with calcination temperature increase. But the grain size analysis by TEM verifies that the calcination temperature has in fact a small effect on the size. The DRS analysis indicates that the band-gap energy is affected by the calcination temperature. The values obtained increase from 2.62 eV to 2.89 eV and 2.98 eV with temperature increase.

lham, Chadli& Omari, Mahmoud & Abu-Dalo, Muna&Albiss, Borhan. et al. [57]Synthesized $LaCr1_{-x}Zn_xO_3$ through sol– gel method. The effect of Zn doping on the lanthanum chromite prepared was investigated. Thermal decomposition of the dried gel of $LaCr_{0.8}Zn_{0.2}O_3$ was characterized by TG/DTA thermal analysis. The synthesized powders were characterized by means of X-ray diffraction (XRD), infrared spectra (IR), and scanning microscope (SEM). Electrical properties were characterized by the standard four-probe technique. From the preceding analysis, it show the amorphous powders

crystallize in the orthorhombic structure with Pbnm (62) space group, where the crystallite size ranges from 29.46 to 53.21 nm. The oxides $LaCr_{1-x}Zn_xO_3$ have the comportment of semiconductors in the working temperature range 25–35^0 C. The electrical conductivity increases with the degree of substitution x, whereas the maximum electrical conductivity obtained is 13.8 S/cm at 350 C for $LaCr_{0.3}Zn_{0.3}O_3$ where the electrical conduction occurs by a thermal activated of small polarons hopping. At higher temperature, the electrical behavior is similar to that of pure metal.

JamshaidAlam Khan and Javed Ahmad [58] reported the optical and transport properties of double perovskite La_2CrMnO_6 synthesized by auto combustion sol-gel method. The single phase formation with orthorhombic structure having Pbns symmetry has been confirmed by Rietveld refinement of x-ray diffraction (XRD) pattern. The particle size has been calculated from Debye Scherer formula and scanning electron micrograph (SEM). The elemental composition has been checked using energy dispersive x-ray (EDX) spectroscopy. The infrared (IR) reflectivity spectrum has been measured in the frequency range of 30–7500 cm^{-1} at near normal incidence at room temperature. We observed only eight well resolved phonon modes. Indirect optical band gap 0.96 eV has been estimated using Tauc relation from UV-visible absorption spectrum. The DC electrical resistivity measurement suggests small polaronic hopping above room temperature. The temperature and frequency dependent AC dielectric measurements and the value of activation energy support semiconducting nature of the material.

Enhessari, Morteza&Salehabadi, Ali &Khoobi, Asma&Amiri, Razieh. Et al. [59] Synthesized $LaCrO_3$ perovskite nanopowders using a sol-gel method using stoichiometric proportion of materials containing lanthanum and chromium in stearic acid complexing agent. Structural analysis of $LaCrO_3$ indicated an octahedral framework in its XRD pattern bearing crystallite size in the range of 28 nm. The particle sizes were confirmed by morphological scanning of the sample. The optical properties of $LaCrO_3$ nanopowders clearly indicated an interesting optical activity of $LaCrO_3$ in the UV and visible ranges. The degradation activation energy (Ed) was calculated from the output of a moderate thermal programming profile at about 207.97 kJ·mol−1 using Kissinger equation. Capacity, impedance and AC resistance of the perovskites was obtained at 2.970 nF, 2.522 MΩ and 16.19 MΩ, respectively.

Sol-Gel is a low cost, well-established and flexible synthetic route to produce a wide range of micro- and nanostructures. Small variations in pH, temperature, precursors, time, pressure, atmosphere, among others, can lead to a wide family of compounds that share the same molecular structures. Sol-Gel method is one of the simplest techniques to synthesize high-quality nano and microstructures. This method provides several advantages over other synthesis routes such as control over the texture, size and surface properties of the materials, easy to implement, low cost, high quality, and production of materials with large surface areas. This flexibility and simplicity make it very popular in the production of nanoscale powders and its wide used as a coating method [48-54].

Navas, D. Fuentes, S. Castro-Alvarez, A. Chavez-Angel, E. et al. [55] reported that the Sol-Gel method has many unique advantages over other synthesis method which are: Possibility of obtaining special products such as powders, films or coatings, microspheres, fibers. Obtaining new solids with

improved properties. High purity and homogeneity of the materials obtained. Saving energy during the process. Full control over the particle size and morphology. The solution and reaction step allows to incorporate easily, uniformly and quantitatively some trace elements, achieving a uniform doping at the molecular level.Also have following disadvantages which are: Very sensible to moisture. Difficult to scale up. Can include several steps and is a time-consuming process. Dimension and volume changes during different steps.

5. Conclusion and Discussion:

This review article provide basics of the perovskite structure also summarized that, Sol-Gel is a low cost, well-established and flexible synthetic route to produce a wide range of micro- and nanostructures. Small variations in pH, temperature, precursors, time, pressure, atmosphere, among others, can lead to a wide family of compounds that share the same molecular structures. Sol-Gel method offers a unique synthesis route to produce novel and tailor-made nanomaterials with full control of morphology, size, composition, and crystallinity porosity enhanced by combustion or hydrothermal/solvothermal treatment. Nevertheless, some precautions must be taken in order to obtain the best results. Sol-Gel method is one of the simplest techniques to synthesize high-quality nano and microstructures. This method provides several advantages over other synthesis routes such as control over the texture, size and surface properties of the materials, easy to implement, high quality, and production of materials with large surface areas. This flexibility and simplicity make it very popular in the production of nanoscale powders and its wide used as a coating method.The nanoparticle composition must be analysed before running the synthesiswe have briefly described how can be phase identification of the perovskites and their structural analysis using Rietveld refinement of the XRD data. The morphological, surface characteristics, optical studies and how to identify surface compositions of the various components of the prepared perovskites were also included in characterisation of perovskite. The specific surface area of the perovskite, which is very important characteristic of a solid catalyst, is strongly affected by the preparation method used. We conclude that, porous surface with internal pores contributing the highest surface areas mainly obtained by sol-gel better than other synthesis methods.i.e. sol-gel is simple, cheap and better method to synthesize perovskite material. Sol-Gel processes in the future could be assisted with photocatalyst during synthesis. This could induce the formation of desirable doping processes or could reduce the formation of secondary phases. The use of biomaterials in the synthesis of Sol-Gel, especially organic waste, offers a novel low-cost and ecological platform for the manufacture of functional materials.

Acknowledgment:

The authors thank to Principal, L. V. H. College and Research Centre in Electronic Science, Panchavati, Nashik, India, for providing Library, computer and internet facilities.

References:

1. Di Zhou, Tiantian Zhou, Yu Tian, Xiaolong Zhu and YafangTu .2018. :"Perovskite-based solar cells: material, methods and future Perspectives"Journal of Nanomaterial volume, page-14.
2. Weidner, D. J. and Navrotsky, A. 1986. Perovskite: A Structure of Great Interest to Geophysics and Materials Science, volume 45. AGU, Washington, DC.
3. Bhalla, A. Guo, S. R. and Roy, R. 2000. The perovskite structure – a review of its role in ceramic science and technology. Material Research Innovations, 4(1):3–26.
4. Goldschmidt, V. M. 1926. Die Gesetze der Krystallochemie. Naturwissenschaften. 14:477-485.
5. Bednorz, J.G. and Muller, K.A. 1986. Possible highTc superconductivity in the BaLaCuO system. Zeitschriftf˙urPhysik B Condensed Matter, 64(2):189–193.
6. Johnsson, M. Lemmens, P. 2005. Crystallography and chemistry of perovskites. In: Kronmuller H, Parkin S, editors. Handbook of Magnetism and Advanced Magnetic Materials. Vol. 4. USA: John Wiley & Sons; pp. 1-11
7. Atta, N.F. Galal, A. El-Ads, E.H. 2016. Synthesis, characterization and applications. In: Pan L, Zhu G, editors. Perovskite Nanomaterials. London: IntechOpen; pp. 107-151. Ch. 4
8. Labhasetwar, N. Saravanan, G. Kumar, S. Manwar,M.N. Khobragade, R. Doggali, P. Grasset, F. 2015. Perovskite – type catalytic materials for environmental applications, Sci. Tech. Adv. Mat., 16, 036002, 13 pp.
9. Hortschitz, W. Steiner, H. Stifter, M. Kainz, A. Kohl, F. Siedler, C Schalko, J. and Keplinger, F. 2016. Novel MOEMS Lorentz force transducer for magnetic fields, Proc. Eng., 168, 680-683.
10. Zheng, K. Zhu, Q. Abdellah, M. Messing, M. E. Zhang,W. A. Generalov, 2015. "Exciton Binding Energy and the Nature of Emissive States in Organometal Halide Perovskites," The Journal of Physical Chemistry Letters, vol. 6 (15), pp. 2969-2975.
11. Robert, W. Schwartz. (1997) Chemical Solution Deposition of Perovskite Thin Films. Chemistry of Materials, 9(11):2325–2340.
12. Jana Luxov,A. Petra Sulcov,A. and Trojan, M. 2008. Study of perovskite compounds. ˇ Journal of Thermal Analysis and Calorimetry, 93(3):823–827.
13. Weidner, D. J. andNavrotsky, A. 1989. Perovskite: A Structure of Great Interest to Geophysics and Materials Science, volume 45. AGU, Washington, DC.
14. Nada, F. Atta, Ahmed Galal and Ekram, H. El-Ads 2016. Perovskite Nanomaterials – Synthesis, Characterization, and Applications, Perovskite Materials - Synthesis, Characterisation, Properties, and Applications, Likun Pan and Guang Zhu, IntechOpen, DOI: 10.5772/61280.
15. Athayde, D. Souza, D.F. Silva, A. Vasconcelos, D. Nunes, E.H. da Costa, J.C.D. Vasconcelos, W. Review of perovskite ceramic synthesis and membrane preparation methods. Ceram. Int. 2016, 42, 6555–6571.
16. Parashar, M. Shukla, V.K. Singh, R. Metal oxides nanoparticles via sol–gel method: A review on synthesis, characterization and applications. J. Mater. Sci. Mater. Electron. 2020, 31, 3729–3749.
17. Brinker, C.J. Scherer, G.W. 1990. Sol-Gel Science: The Physics and the Chemistry of Sol-Gel Processing. London: Academic Press Inc.
18. Rahaman, M.N. 2003. Ceramic Processing and Sintering. 2nd ed. New York: Marcel Dekker Inc.
19. Pechini, M.P. Patent: Method of Preparing Lead and Alkaline Earth Titanates and Niobates and Coating Method Using the Same to Form a Capacitor. Available online: https://patents.google.com/patent/US3330697A/en
20. Kurajica, S. A Brief Review on the Use of Chelation Agents in Sol-gel Synthesis with Emphasis on β-Diketones and β-Ketoesters. Chem. Biochem. Eng. Q. 2019, 33, 295–301.
21. Roy, R. Ceramics by the Solution-Sol-Gel Route. Science 1987, 238, 1664–1669.
22. Shinde, V.S. Kapadnis, K.H. Sawant, C.P. Ahiraro, A.N. 2018. Synthesis and Characterization of LaCrO3 by Sol-gel method. International journal of chemical and physical science7,311-316.
23. Liesegang, R.E. UebereinigeEigenschaften von Gallerten. Z. Chem. Ind. Kolloide 1896, 11, 212; Reprint: Liesegang, R.E. UebereinigeEigenschaften von Gallerten. Z. Chem. Ind. Kolloide 1907, 1, 212

24. Li, Y. Xue, L. Fan, L. Yan, Y. The effect of citric acid to metal nitrates molar ratio on sol–gel combustion synthesis of nanocrystalline $LaMnO_3$ powders. J. Alloys Compd. 2009, 478, 493–497.
25. Yin, X. Wang, S. Wang, B. Shen, L. Perovskite-type $LaMn_{1-x}B_xO_{3+\delta}$ (B = Fe, CO and Ni) as oxygen carriers for chemical looping steam methane reforming. Chem. Eng. J. 2021, 422, 128751.
26. Yin, X. Shen, L. Wang, S. Wang, B. Shen, C. Double adjustment of Co and Sr in $LaMnO_{3+\delta}$ perovskite oxygen carriers for chemical looping steam methane reforming. Appl. Catal. B Environ. 2021, 301, 120816.
27. Li, C. Yu, Z. Liu, H. Chen, K. High surface area $LaMnO_3$ nanoparticles enhancing electrochemical catalytic activity for rechargeable lithium-air batteries. J. Phys. Chem. Solids 2018, 113, 151–156.
28. Shaterian, M.; Enhessari, M.; Rabbani, D.; Asghari, M.; Salavati-Niasari, M. Synthesis, characterization and photocatalytic activity of $LaMnO_3$ nanoparticles. Appl. Surf. Sci. 2014, 318, 213–217.
29. Calvo, J.A.O. Ayo, B.P. De La Torre, U. González-Velasco, J.R. Key factors in Sr-doped $LaBO_3$ (B = Co or Mn) perovskites for NO oxidation in efficient diesel exhaust purification. Appl. Catal. B Environ. 2017, 213, 198–210.
30. Du, D. Zheng, R. He, M. Zhao, C. Zhou, B. Li, R. Xu, H. Wen, X. Zeng, T. Shu, C. A-site cationic defects induced electronic structure regulation of $LaMnO_3$ perovskite boosts oxygen electrode reactions in aprotic lithium–oxygen batteries. Energy Storage Mater. 2021, 43, 293–304
31. Amador, C.; Martin de Juan, L. 2012. Strategies for structured particulate systems design. Comput. Aided Chem. Eng. 39, 509–579.
32. Gosavi, P.V. Biniwale, R.B. 2010. Pure phase LaFeO3 perovskite with improved surface area synthesized using different routes and its characterization. Materials Chemistry and Physics; 119:324–329.
33. Rosso, I.; Saracco, G.; Specchia, V.; Garrone, E. 2003. Sulphur poisoning of $LaCr_{0.5-x}Mn_xMg_{0.5}O_3 \cdot yMgO$ catalysts for methane combustion. Appl. Catal. B , 40, 195–205.
34. Arai, H.; Yamada, T.; Eguchi, K.; Seiyama, T. 1986. Catalytic combustion of methane over various perovskite-type oxides. Appl. Catal. 26, 265–276.
35. Popescu, I.; Sandulescu, I.; Redey, A.; Marcu, I.C. 2011. Study of the catalytic activity–semiconductive properties relationship for BaTiO3 and PbTiO3 perovskites, catalysts for methane combustion. Catal. Lett. 141, 445–451.
36. Cimino, S.; Lisi, S.; De Rossi, S.; Faticanti, M.; Porta, P. 2003. Methane combustion and CO oxidation on LaAl1−xMnxO3 perovskite-type oxide solid solutions. Appl. Catal. , 43, 397–406
37. Kirchenerov, J.; Klvana, D. 1994. Preparation and characterization of high surface perovskite electrocatalysts. Int. J. Hydrogen Energ, 19, 501–506.
38. Busca, G.; Daturi, M.; Finocchio, E.; Lorenzelli, V.; Ramis, G.; Willey, R.J. 1997. Transition metal mixed oxides as combustion catalysts: Preparation, characterization and activity mechanisms. Catal. Today, 33, 239–249.
39. Milt, V.G.; Spretz, R.; Ulla, M.A.; Lambardo, E.A. 1996. The nature of active sites for the oxidation of methane on La-based perovskites. Catal. Lett. 42, 57–63
40. Cimino, S.; Lisi, L.; Pirone, R.; Russo, G.; Turco, M. 2000. Methane combustion on perovskites-based structured catalysts. Catal. Today, 59, 19–31.
41. Wei, X.; Hug, P.; Figi, R.; Trottmann, M.; Weidenkaff, A.; Ferri, D. 2010. Catalytic combustion of methane on nano-structured perovskite-type oxides fabricated by ultrasonic spray combustion. Appl. Catal. 94, 27–37.
42. Baiker, A.; Marti, P.E.; Keusch, P.; Fritsch, E.; Relier, A. 1994. Influence of the A-Site cation in $ACoO_3$ (A = La, Pr, Nd, perovskite-type oxides on catalytic activity for methane combustion. J. Catal.146, 2 68–276.
43. Ciambelli, P.; Cimino, S.; De Rossi, S.; Faticanti, M.; Lisi, L.; Minelli, G.; Pettiti, I.; Porta, P.; Russo, G.; Turco, M. 2000. $AMnO_3$ (A = La, Nd, Sm) and $Sm_{1-x}Sr_xMnO_3$ perovskites as combustion catalysts: Structural, redox and catalytic properties. Appl. Catal. 24, 243–253.
44. Ciambelli, P.; Cimino, S.; De Rossi, S.; Lisi, L.; Minelli, G.; Porta, P.; Russo, G. 2001. $AFeO_3$ (A = La, Nd, Sm) and $LaFe_{1-x}Mg_xO_3$ perovskites as methane combustion and CO oxidation catalysts: Structural, redox and catalytic properties. Appl. Catal. 29, 239–250.

45. Lozano-Gorrín, A.D. 2012 Polycrystalline Materials—Theoretical and Practical Aspects. In: Zakhariev Z, editor. Universidad de La Laguna. Spain: InTech; p 107–124. Chapter 5.
46. Abd Al-Rahman, Y.M. 2013. Characterization and some applications of nano-inorganic oxides synthesized by microwave technique [MSc thesis]. Faculty of Science Cairo University.
47. Gosavi, P.V. Biniwale, R.B. 2010. Pure phase $LaFeO_3$ perovskite with improved surface area synthesized using different routes and its characterization. Materials Chemistry and Physics; 119:324–329.
48. Danks, A.E. Hall, S.R. Schnepp, Z. The evolution of 'sol–gel' chemistry as a technique for materials synthesis. Mater. Horizons 2016, 3, 91–112.
49. Ye, C.-Q. Sol-Gel Processes of Functional Powders and Films. In Chemical Reactions in Inorganic Chemistry; IntechOpen: London, UK, 2018.
50. Purcar, V. Somoghi, R. Ni¸tu, S.G. Nicolae, C.-A. Alexandrescu, E. Gîfu, I.C. Gabor, A.R. Stroescu, H. Ianchi¸s, R. Căprărescu, S. The Effect of Different Coupling Agents on Nano-ZnO Materials Obtained via the Sol–Gel Process. Nanomaterials 2017, 7, 439.
51. Fu, M. Li, Y. Wu, S. Lu, P. Liu, J. Dong, F. Sol–gel preparation and enhanced photocatalytic performance of Cu-doped ZnO nanoparticles. Appl. Surf. Sci. 2011, 258, 1587–1591.
52. Purcar, V. Rădi¸toiu, V. Dumitru, A. Nicolae, C.-A. Frone, A.N. Anastasescu, M. Rădi¸toiu, A. Raduly, M.F. Gabor, R.A. Căprărescu, S. Antireflective coating based on TiO_2 nanoparticles modified with coupling agents via acid-catalyzed sol-gel method. Appl. Surf. Sci. 2019, 487, 819–824.
53. Spataru, C.I. Purcar, V. Ghiurea, M. Radovici, C. Stanga, G. Donescu, D. Effects of the nanoassociation of hexadecyltrimethoxysilane precursors on the sol–gel process. J. Sol-Gel Sci. Technol. 2013, 65, 344–352.
54. Znaidi, L. Sol–gel-deposited ZnO thin films: A review. Mater. Sci. Eng. B 2010, 174, 18–30.
55. Navas, D.; Fuentes, S.; Castro-Alvarez, A.; Chavez-Angel, E. Review on Sol-Gel Synthesis of Perovskite and Oxide Nanomaterials. Gels 2021, 7, 275.
56. Situmeang, Rudy &Sembiring, Simon &Simanjuntak, Wasinton&Sembiring, Zipora&Yuwono, Suripto. CHARACTERISTICS OF $LaCrO_3$ NANOMATERIAL THE EFFECT OF THE CALCINATION TEMPERATURE. 2019. 54. 715-720.
57. Ilham, Chadli& Omari, Mahmoud & Abu-Dalo, Muna&Albiss, Borhan. Preparation by sol–gel method and characterization of Zn-doped $LaCrO_3$ perovskite. Journal of Sol-Gel Science and Technology. 2016 80. 10.1007/s10971-016-4170-5.
58. JamshaidAlam Khan and Javed Ahmad 2019 *Mater. Res. Express* 6 115906
59. Enhessari, Morteza&Salehabadi, Ali &Khoobi, Asma&Amiri, Razieh. Kinetic properties and structural analysis of LaCrO3 nanoparticles. Materials Science-Poland. 2017. 35. 10.1515/msp-2017-0043.
60. SALAVATI-NIASARI M., DAVAR F., FARHADI M., J. Sol-Gel Sci. Technol 2009, 1, 48.
61. NOORI E., MIR N., SALAVATI-NIASARI M., GHOLAMI T., MASJEDI-ARANI M., J. Sol-Gel Sci. Technol.,2014, 3 , 544.

IJCRT.ORG ISSN : 2320-2882

INTERNATIONAL JOURNAL OF CREATIVE RESEARCH THOUGHTS (IJCRT)

An International Open Access, Peer-reviewed, Refereed Journal

Review on: IoT based Air pollution monitoring techniques

*[1]Monali S.Hase, [2] Umesh. J. Tupe, *[3]Vijay S. Kale

[1, 3]Department of Electronic Science and Research Center, Loknete Vyankatrao Hiray Arts, Science and Commerce College Panchavati, Nashik, Affiliated to SPPU, Pune, Maharashtra - 422003, India.

[2]Department of Electronic Science,VADP's Arts, Science & Commerce College, Shirsondi, Tal – Malegaon, Dist-Nashik, Affiliated to SPPU, Pune, Maharashtra – 423208,India.

Abstract:-

During the previous few decades, global warming and climate change have been major issues among scientists. Almost all atmospheric scientists agree that global warming is a serious environmental hazard caused by increased quantities of certain trace gases in the atmosphere. The pollution level has risen through time due to a variety of growing populations, increased vehicle use, industrialisation, and urbanisation, all of which have negative consequences on human wellbeing by directly impacting the health of those who are exposed to it. Monitoring of poisonous gases such as CO_2, Methane, NH_3, CFC, Dichlorofluoromethane, NOx, and others is a necessity in today's world. IoT provides a versatile platform for monitoring these types of gases. The Internet of Things (IoT) might be a global network of "smart gadgets" that perceive and communicate with their environment, as well as interact with humans and other systems. It will display the air elements in PPM on the Display and on the website so that we can easily monitor them. The current research paper discusses the various IoT-based air pollution monitoring techniques.

Keywords:*Global Warming, NOx, CFC, Internet of Things, Air Pollution.*

I. Introduction:

The rise of technology, as well as increased harmful pollutants from factories and automobiles, causes atmospheric conditions to deteriorate each year. Despite the fact that air is a life-giving resource, many people are unaware of the severity of air pollution or have only just become aware of the issue [1, 2]. Air pollution is the most hazardous and severe of the numerous types of pollutants, including water, soil, heat, and noise, and is responsible for climate change and daily life illnesses. Pollution has very serious health consequences, including strokes, emphysema, and cardiovascular disease. Moreover, as evidenced by recent global air pollution concerns like ozone depletion [3, 4], air pollutants have a

harmful influence on humans and the earth's ecology. As a result, monitoring and control of air quality are major concerns [1, 4].

In recent years, new technologies such as the Internet of Things (IoT) and cloud computing have unveiled new real-time monitoring possibilities in a variety of industries. The Internet of Things (IOT) is a system in which matter and people are given limited identities and the ability to move data over a network without the need for two-way human-to-human (source-to-destination) or human-to-computer (human-to-computer) communication. As a result, numerous researchers [5-8] have looked at integrating these technologies into indoor air quality monitoring systems. These investigations, on the other hand, were limited to incorporating an IoT platform architecture to monitor air quality in real time. Combining these new technologies, which include a wireless sensor network that automatically transmits, processes, analyses, and visualises data, can provide significant benefits in terms of improving indoor air quality [9, 10].

The properties of the Internet of Things, such as an ultra-large network of things, device and network level heterogeneity, and massive quantities of events generated spontaneously by these things, will make expansion of diverse applications and services extremely difficult. Middleware, in general, will make the development process easier by coordinating the actions of heterogeneous data and networking equipment and facilitating interoperability between different software and systems. A lot of suggestions for IoT middleware have surfaced in recent months. Wireless sensor networks (WSN), a critical component of IoT, were the focus of these concepts [10, 11].

To create an IoT-based pollution monitoring system that can be accessible through Wi-Fi and used to assess the level of pollution in a specific location or site. A variety of sensors are used to collect data from the atmosphere or its contents. Sensors that measure air pollution and noise pollution measure sound levels [9-12]. The distance between the Garbage Bin lids is measured using ultrasonic sensors. Ultrasonic sensors collected data. The IoT Platform integrates the fire alarm and monitoring systems. It can detect smoke, temperature changes, and flames, among other things. All of the data from these sensors is essentially analogue. These signals are digitally transformed. The system also includes a Wi-Fi module for transferring data to other locations or gaining access to data from afar [10-13].

The Air Pollution Monitoring System uses the Internet to monitor the air quality and will sound an alert if the air quality drops below a particular level, which indicates there are enough harmful gases. It will display the air quality in PPM (Parts Per Million) on the display unit and on the website page so that it can be readily monitored.

II. Literature Survey:

The wireless standard was used to design, build, and observe an Air Pollution Monitoring System for monitoring the combination of key air pollutant gases. Using semiconductor sensors, this device measures a mixture of hazardous gases. A single-chip microprocessor, an array of air pollution sensors, a GSM-Module, and a GPS-Module are all included in the hardware unit. The Central-Server is an internet-connected high-end personal computer application server. The hardware collects air pollution levels and stores them in a frame that includes the GPS physical location, time, and date. Finally, the

frame is uploaded to the GSM-Modem and communicated through WSN to the Central-Server. Environmental air pollution has a substantial impact on the mixture of elements in the atmosphere, resulting in global warming and acid rain. It is critical to have an air pollution monitoring system in place to avoid such detrimental natural imbalances. The typical air quality monitoring method, which is overseen by the Pollution Control Department, is too expensive. Wireless Sensor Networks are a novel and difficult study subject for embedded system design automation because their design must adhere to strict power and cost constraints [12, 13].

Saiye, Y.D. et al. (2020) [14] designed air quality detection and monitoring system employs a wireless sensor network to monitor air quality in various places while also producing near real-time information and data that can be retrieved via smartphones, tablets and internet compatible device. Designed system that can track the amount of contaminants in the air developed by using Arduino Uno, a WIFI module, and a MQ135 gas sensor.

Chourey, Pet al. (2022) [15]Designed IoT baised air pollution monitoring system using MQ135, MQ7, and DHT11 gas sensors. These sensors will respond to the esp32 module, which will show the information on the ThinkSpeak web server, and configure a buzzer to notify us if the air quality drops below the set value.

Sunil Mahesh Pattar et al. (2018) [12] reported survey on IoT-based air pollution monitoring system and purposed the level of pollution has risen through time due to a variety of factors such as population growth, increased vehicle use, industrialisation, and urbanisation, all of which have negative consequences on human wellbeing by directly impacting the health of those who are exposed to it. an IOT-based Air Pollution Monitoring System in which we will monitor the air quality over the internet using a web server and will activate an alarm when the air quality drops below a certain level, which means when there is a sufficient amount of harmful gases such as CO_2, smoke, alcohol, benzene, and NH_3 gas in the atmosphere. It will display the air components in PPM on the LCD and on the website so that we can easily monitor them. One can use your computer or smartphone to monitor the air pollutants in this IoT project.

Harsh Gupta and colleagues (2019) [16] developed an IoT based air pollution monitoring system for smart cities. Smart cities are under pressure to stay livable as the world's population becomes more urbanised. The air quality of urban centers has become a prominent source of worry around the world in recent years. As a result, in order to make a city smart and livable, it is vital to regularly evaluate its air quality index. We propose and construct an IoT-based Air Quality Monitoring System for Smart Cities in this research. Air quality data is retrieved in real time via smart devices and analysed to determine the influence on city people. Temperature, Humidity, Carbon Monoxide, LPG, Smoke, and other harmful particulate matters like PM2.5 and PM10 levels in the atmosphere can all be measured using smart devices. An Android application makes the obtained data available to everyone in the world.

Harsh N. Shah and colleagues et al. (2018) [17] developed IOT based air pollution monitoring system using ATmega328P, Wi-Fi module ESP8266, MQ135 Gas sensor, MQ 6 LPG gas sensor, LM35 temperature sensor and humidity sensor SY-H5220. The Internet of Things-based Air Pollution Monitoring System is used to monitor the air quality via a web server. It will sound an alert if the air quality falls below a particular threshold, which signifies there are enough dangerous gases in the air, such as CO_2, smoking, alcohol, benzene, NH_3, and NOx. It will display the air quality in PPM on the LCD as well as on the webpage, allowing for easy monitoring of air pollution.

Patil, P., et al. (2017) [18] developed smart IoT based system for vehicle noise and pollution monitoring. The hardware architecture as well as the software implementation are thoroughly detailed. IoT technology is also used to verify the system's performance. The clever intelligent environmental system that was built monitors the pollutants produced by automobiles and alerts vehicle owners to take action to reduce pollution. The data on pollution levels is also sent to a server for further study. Air pollution authorities can examine data and identify car registration numbers that contribute to increased pollution in the atmosphere. The designed system is low-cost, easy-to-use, and may be placed in any location. The created system outperforms the old system in terms of accuracy and cost.

Saha, A.K., et al. (2018) [19] developed raspberry Pi controlled cloud based air and sound pollution monitoring system with temperature and humidity sensing using Raspberry Pi, Wi-Fi module. Authors reported controlling and carefully monitoring the situation has become necessary in order to take the necessary steps to alleviate the situation. An IOT-based technique for monitoring the Air Quality Index and Noise Intensity of a region has been proposed in this research. The Air Quality Index Monitoring Module, the Sound Intensity Detection Module, the Cloud-based Monitoring Module, and the Anomaly Notification Module are the four modules that make up the recommended technology. To begin, the Air Quality Index is calculated based on the presence of five specific air contaminants. The sound intensity is then detected using the appropriate sensor. After that, the Cloud-based Monitoring Module ensures the data collection process with the support of the Raspberry Pi's Wi-Fi module, achieving the goal of data analysis on a regular basis. Finally, the Anomaly Notification Module notifies the user if there is a problem.

Advances in wireless communication and sensor technologies have resulted in a kaleidoscope of changes in the air pollution monitoring paradigm in recent years. The Internet of Things has made it possible to produce smart environments in which items communicate and collaborate. In order to avoid tragic mishaps, the researchers used Raspberry Pi and IoT to monitor dangerous gas leakage and air quality.

III. Conclusion:

This review article provides details of IoT based system used in recants years. The review provided technological details as well as recent communication standards and embedded system platforms used in air pollution monitoring systems.

Acknowledgment

The authors thank to Principal, L. V. H. College and Research Centre in Electronic Science, Panchavati, Nashik, India, for providing computer and internet facilities.

References:

1. Jo, J., Jo, B., Kim, J., Kim, S. and Han, W., 2020. Development of an IoT-based indoor air quality monitoring platform. *Journal of Sensors*, *2020*.
2. Parmar, G., Lakhani, S. and Chattopadhyay, M.K., 2017, October. An IoT based low cost air pollution monitoring system. In *2017 International Conference on Recent Innovations in Signal processing and Embedded Systems (RISE)* (pp. 524-528). IEEE.
3. Okokpujie, K.O., Noma-Osaghae, E., Odusami, M., John, S.N. and Oluga, O., 2018. A smart air pollution monitoring system. *International Journal of Civil Engineering and Technology (IJCIET)*, *9*(9), pp.799-809.
4. Kulkarni, K.A. and Zambare, M.S., 2018. The impact study of houseplants in purification of environment using wireless sensor network. *Wireless Sensor Network*, *10*(3), pp.59-69.
5. Marques, G., Ferreira, C.R. and Pitarma, R., 2019. Indoor air quality assessment using a CO2 monitoring system based on internet of things. *Journal of medical systems*, *43*(3), pp.1-10.
6. Taştan, M. and Gökozan, H., 2019. Real-time monitoring of indoor air quality with internet of things-based E-nose. *Applied Sciences*, *9*(16), p.3435.
7. Rackes, A., Ben-David, T. and Waring, M.S., 2018. Sensor networks for routine indoor air quality monitoring in buildings: Impacts of placement, accuracy, and number of sensors. *Science and Technology for the Built Environment*, *24*(2), pp.188-197.
8. Benammar, M., Abdaoui, A., Ahmad, S.H., Touati, F. and Kadri, A., 2018. A modular IoT platform for real-time indoor air quality monitoring. *Sensors*, *18*(2), p.581.
9. Ghayvat, H., Mukhopadhyay, S., Gui, X. and Suryadevara, N., 2015. WSN-and IOT-based smart homes and their extension to smart buildings. *Sensors*, *15*(5), pp.10350-10379.
10. Gupta, K. and Rakesh, N., 2018, January. IoT based automobile air pollution monitoring system. In *2018 8th international conference on cloud computing, data science & engineering (Confluence)* (pp. 14-15). IEEE.
11. Pradhan, M.A., Patankar, S., Shinde, A., Shivarkar, V. and Phadatare, P., 2017, August. IoT for smart city: Improvising smart environment. In *2017 International Conference on Energy, Communication, Data Analytics and Soft Computing (ICECDS)* (pp. 2003-2006). IEEE.
12. Mohesh, P.S. and Rajendra, P.B., A survey Paper on Air Pollution Monitoring using IOT. *IJARIIE-ISSN (O)*, *4*.
13. Shaikh, I.R. and Tankkar, S., IoT Based Air Quality Monitoring With Multi-Model Analysis Using Ml Algorithms.
14. Saiye, Y.D. and Ajose-Ismail, B.M., 2020. IoT Based Air Quality Detection and Monitoring System. *International Journal of Research and Innovation in Applied Science*, *5*(7), pp.66-68.

15. Chourey, P., Soni, K., Singh, N.J. and Agarwal, R., 2022. IoT-Sodar Network for Airshed Management Planning. *IETE Journal of Research*, pp.1-15.
16. Gupta, H., Bhardwaj, D., Agrawal, H., Tikkiwal, V.A. and Kumar, A., 2019, February. An IoT based air pollution monitoring system for smart cities. In *2019 IEEE International Conference on Sustainable Energy Technologies and Systems (ICSETS)* (pp. 173-177). IEEE.
17. Shah, H.N., Khan, Z., Merchant, A.A., Moghal, M., Shaikh, A. and Rane, P., 2018. IOT based air pollution monitoring system. *International Journal of Scientific & Engineering Research*, *9*(2), pp.62-66.
18. Patil, P., 2017, May. Smart IoT based system for vehicle noise and pollution monitoring. In *2017 International Conference on Trends in Electronics and Informatics (ICEI)* (pp. 322-326). IEEE.
19. Saha, A.K., Sircar, S., Chatterjee, P., Dutta, S., Mitra, A., Chatterjee, A., Chattopadhyay, S.P. and Saha, H.N., 2018, January. A raspberry Pi controlled cloud based air and sound pollution monitoring system with temperature and humidity sensing. In *2018 IEEE 8th Annual Computing and Communication Workshop and Conference (CCWC)* (pp. 607-611). IEEE.

IJCRT.ORG ISSN : 2320-2882

INTERNATIONAL JOURNAL OF CREATIVE RESEARCH THOUGHTS (IJCRT)

An International Open Access, Peer-reviewed, Refereed Journal

Synthesis And Characterization Of Zinc Oxide Nanoparticles Using Green Synthesis Method

Archana A. Chaudhari[1*], Umesh. J. Tupe[2], Arun V. Patil[3], Chandrakant. G. Dighavkar[4].

[1, 3, 4]Research Centre in Electronic Science and Department of Electronic Science, Loknete Vyankatrao Hiray Arts, Science and Commerce College Panchavati, Nashik, Affiliated to SPPU, Pune, Maharashtra - 422003, India.

[2]Department of Electronic Science, VADP's Arts, Science & Commerce College, Shirsondi, Tal – Malegaon, Dist-Nashik, Affiliated to SPPU, Pune, Maharashtra – 423208, India.

[3]Department of Physics, MGV's, Arts, Science and Commerce College, Manmad, Dist. Nashik 423104, India

[4]Departmet of Physics, MGV's, Arts, Science and Commerce College, Surgana, Dist. Nashik 422211, India

Abstract: Nanoparticles (NPs) exhibit distinct features from their bulk materials, and they have applications in many different of domains in life science. Green-synthesized NPs have attracted a lot of attention because of their intrinsic characteristics like efficiency, eco-friendliness, and cost-effectiveness. The current research focuses on the green synthesis of zinc oxide (ZnO) nanoparticles (NPs) employing wheatgrass extract. Wheatgrass extract acts as a capping agent, as evidenced by its presence on the surface of ZnO nanoparticles. X-Ray Diffraction (XRD), Scanning Electron Microscopy (SEM), Energy Dispersive X-Ray Analysis (EDAX), and Fourier Transform Infrared spectroscopy (FTIR) were used to characterise the synthesised ZnO nanoparticles. The wurtzite hexagonal structure of the synthesised ZnO nanoparticles was polycrystalline in nature, with a preferential orientation along the (101) plane. Using Scherer's formula, the crystallite size was determined to be 36.18 nm. The morphological and elemental analysis of the films were investigated using SEM and EDAX tools, respectively. The presence of this extract on the surface of ZnO NPswas investigated using FTIR analysis, which confirmed the presence of many functional groups on the surface of ZnO NPs.

Keywords **-** ZnO nanoparticles, Wheatgrass extract,FTIR, Green-synthesis, Crystallite Size.

1. Introduction:

Environmental engineering is an interesting research topic that aims to improve human living standard. Environmental engineering uses nanotechnology in a variety of ways. Green eco-friendly approach has been impressively explored for the synthesis of a diverse range of nanostructures during the previous few decades [1]. Plant-based nanoparticles have numerous benefits over traditional physico-chemical processes and have a wide range of applications in biology and medicine [2].

ZnO is a rare inorganic compound found in nature. It's usually found as a crystalline substance. Manganese impurities in naturally occurring ZnO give it a classic red or orange color. ZnO is a white crystalline powder that is almost water insoluble when purified. The semiconductor nature of ZnO is n-type. It has a wide band gap of 3.37eV at ambient temperature with a high excitation binding energy (60meV), superior chemical stability, low dielectric constant, strong electrochemical coupling coefficient, and excellent optical absorbance [3].

ZnO NPs have been extensively applied in textile materials, beauty products, diagnostic, solar cells, sensing applications, dielectric materials, electric actuators, as a piezoelectric element, for room temperature UV lasing are only a few of the applications and even micro-electronics due to the relatively low toxicity and size dependant characteristics [3-6].For biosynthesis of NPs for therapeutic reasons, ZnO has been proven to be more beneficial and efficient than other metals. Several investigations have shown that plant extracts can be used to synthesise ZnO NPs [4, 7].The size of NPs is also affected by the plant type or source species from which the plant extract used for NP synthesis is derived [2, 5].

Agropyronrepens, BrotedelTrigo, Agropyre, Doggrass, Elymusrepens, GraminisRhizoma, Quackgrass, Scotch Quelch, Triticumrepens, and Wheat Grass were some of the other names for wheatgrass. This plant grows from the young grass of the ordinary wheat plant, Triticumaestivum. Wheatgrass juice and powder have numerous medicinal qualities for both humans and other animals [1, 8]. This plant's medicinal qualities include lowering blood pressure and cholesterol, preventing tooth decay, healing wounds, and acting as an antibiotic. Vitamin C, vitamin E, thiamin, niacin, pantothenic acid, protein, riboflavin, polyphenol, amino acid, and other substances were found in wheatgrass extract [9]. Although numerous investigations on nanoparticle syntheses have been conducted.

The incorporation of biological components in the nanoparticle synthesis always has been a preferred option for a green synthesis method. Green synthesis has been shown to be particularly effective at controlling the desired NP size and shape, in addition to the environmental ecosystem benefits [10].

2. Experimental Work:

2.1 Synthesis of ZnO nanoparticles using green synthesis method

In the current research work, commercially available AR grade (99.99 % purity) chemicals were used.ZnO nanoparticles have been synthesized by using Zinc nitrate hexahydrate $Zn(NO_3)_2 \cdot 6H_2O$as a source of Zn.20 gm of wheat grass pieces were kept in 100ml distilled water and then boiled for 10 min. at 60 °C temperature. After that, 3 gm Zinc nitrate hexahydrate added in the prepared solution and stirred continuously for 2 hrs using magnetic stirrer up till the coloured of solution become yellow. The obtained

precipitate was annealed at 600°C for 2 hours using muffle furnace. After that nanoparticles of ZnO obtained.

2.2 Structural Characterization:

The synthesized ZnO NPs were characterized by XRD, FESEM, and EDAX to study the structural properties, surface morphology, and elemental composition analysis respectively.

Using FTIR analysis, the functional groups of ZnO NPs were confirmed.

2.2 2.2.1 X-Ray Diffraction (XRD)

On a Rigaku diffractometer (DMAX-500), an X-ray diffractometer with CuKα radiation and wavelength (λ) = 0.154059 nm, XRD patterns of synthesized ZnO NPs were observed. The 2θ values obtained were compared to data files from the Joint Committee on Powder Diffraction Standards (JCPDS). Debye Scherer's formula, Eq. 1, was used to determine the crystallite size [3].

$$D = \frac{K\lambda}{\beta Cos\theta} \quad (1)$$

Where,

D= Crystallite size,

K= Scherrer constant (0.9),

β = Full width of half maxima (FWHM),

λ =wavelength of X source (0.154059 nm).

By using Bragg's formula Eq.2, the interplaner spacing was calculated.

$$d=\lambda/2Sin\Theta \quad (2)$$

Where, λ = wavelength of X-radiation.

2.2.2 SEM

The surface morphology of synthesized ZnO NPswere characterized using a Field Emission Scanning Electron Microscope (FESEM) [Model JOEL 6300 LA GERMANY].

2.2.3 EDAX

Energy dispersive X-ray spectrometer (JOEL-2300, Germany) was used to study the elemental analysisof synthesized ZnO NPs.

2.2.4FTIR

Bonding characteristics of the thick films were analysed by using Shimadzu IR Affinity-1 Fourier transformed infrared spectrometer (FTIR). The FTIR was recorded from 400 to 4000 cm^{-1} with a resolution of 2 cm^{-1}.FTIR analysis was used to evaluate the existence of functional groups of synthesized ZnO NPs.

3. Results and Discussion:

3.1 X-Ray Diffraction (XRD)

Diffraction peaks was seen at 31.64°, 34.31°, 36.12°, 47.43°, 56.48°, and 67.35°, per the results. This pattern clearly matches the phase of standard ZnO (JCPDS card No. 36-1451) [11], which is a hexagonal wurtzite polycrystalline structure with lattice planes (hkl) of (100), (002), (101), (102), (110), (103), and (112), as illustrated in Figure 1.

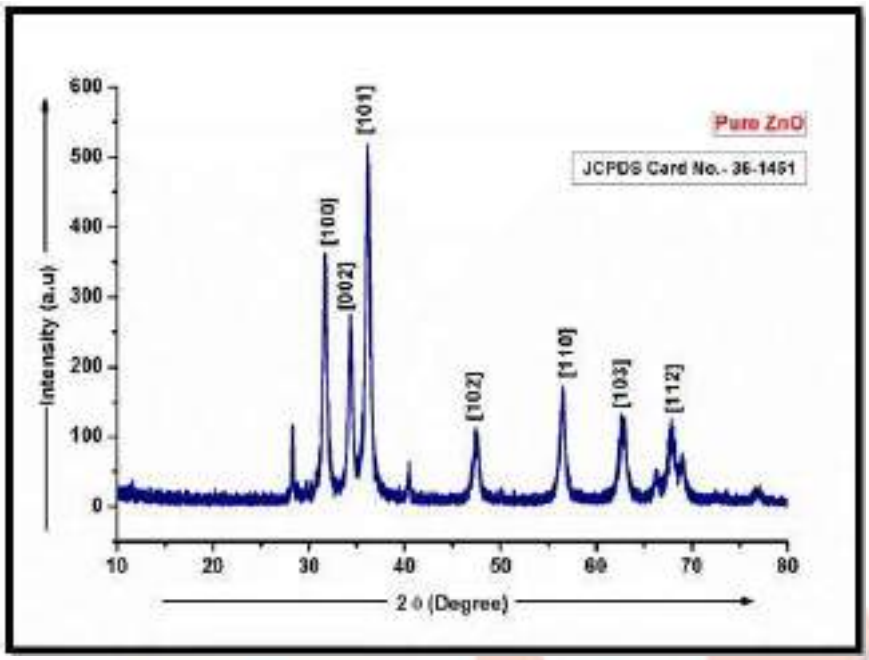

Figure 1: XRD pattern of ZnO nanoparticles

However, there were no peaks of other contaminants found. The observed ZnO spectra in various phases corroborated the high purity of the synthesised ZnO using the green synthesis approach [12]. A high crystallinity of ZnO was revealed by the presence of strong and narrow diffraction peaks in the XRD pattern [13]. The Debye–Scherrer equation was used to compute the crystallite size of ZnO NPs, which was found to be 36.18 nm.

3.2 Scanning Electron Microscopy (SEM)

Figure 2 shows a SEM micrograph of the synthesised ZnO NPs. The formation of spherical nanoparticles with large agglomeration was observed in SEM images of ZnO NPs obtained using the green synthesis method. Kim and Park [14] and Ong et al. [15] found the exact structure in ZnO nanoparticles. During synthesis, the capping agent could be utilised to minimise particle size. The size of nanoparticles were determined using a scanning electron microscope. The particle size ranged from 37.77 to 64.13 nm, as indicated in Figure-2 by the SEM micrograph [16].

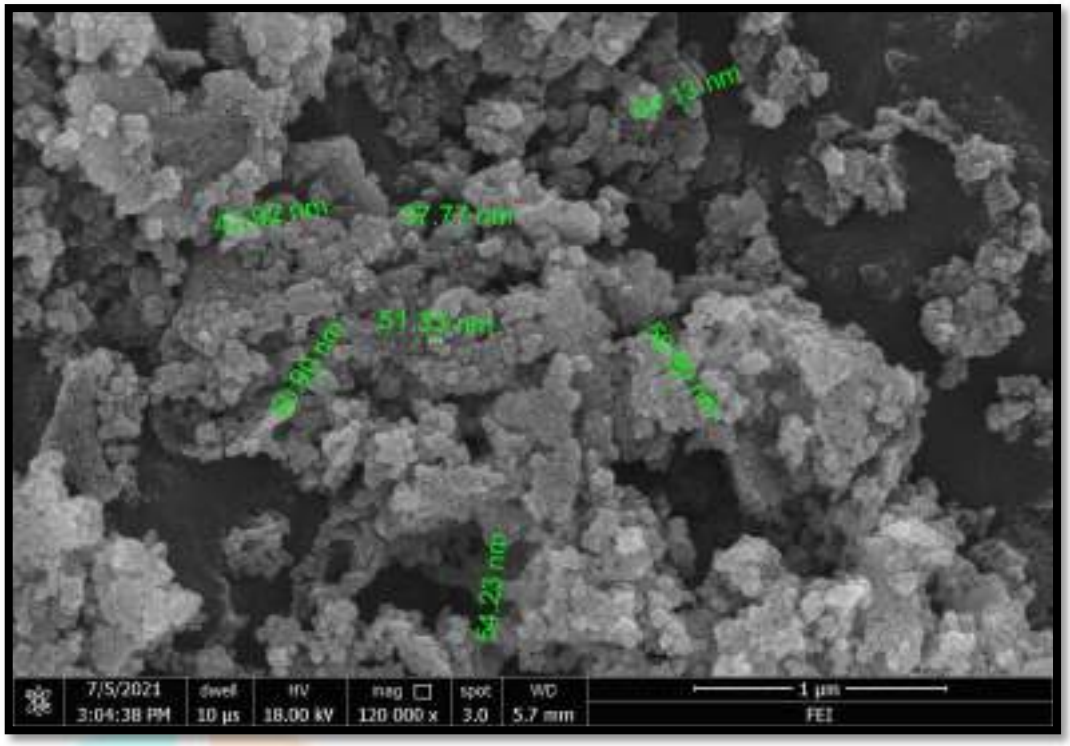

Figure 2: FESEM micrograph of ZnO nanoparticles

3.3 Energy Dispersive X-Ray Analysis (EDAX)

The proportional elemental composition of ZnO nanoparticles was confirmed using the energy dispersive X-rays Analysis (EDAX) tool, as illustrated in Figure 3, by measuring the intensity of the characteristic emitted x- rays. In synthesised zinc oxide nanoparticles, EDAX revealed only the presence of two elements: zinc and oxygen. The atomic and weight percent compositions of elements were shown in Table 1. The purity of the synthesised ZnO NPs was confirmed by EDAX analysis, and our findings are consistent with those of other studies Raj and Jayalakshmyet al. [17, 18].

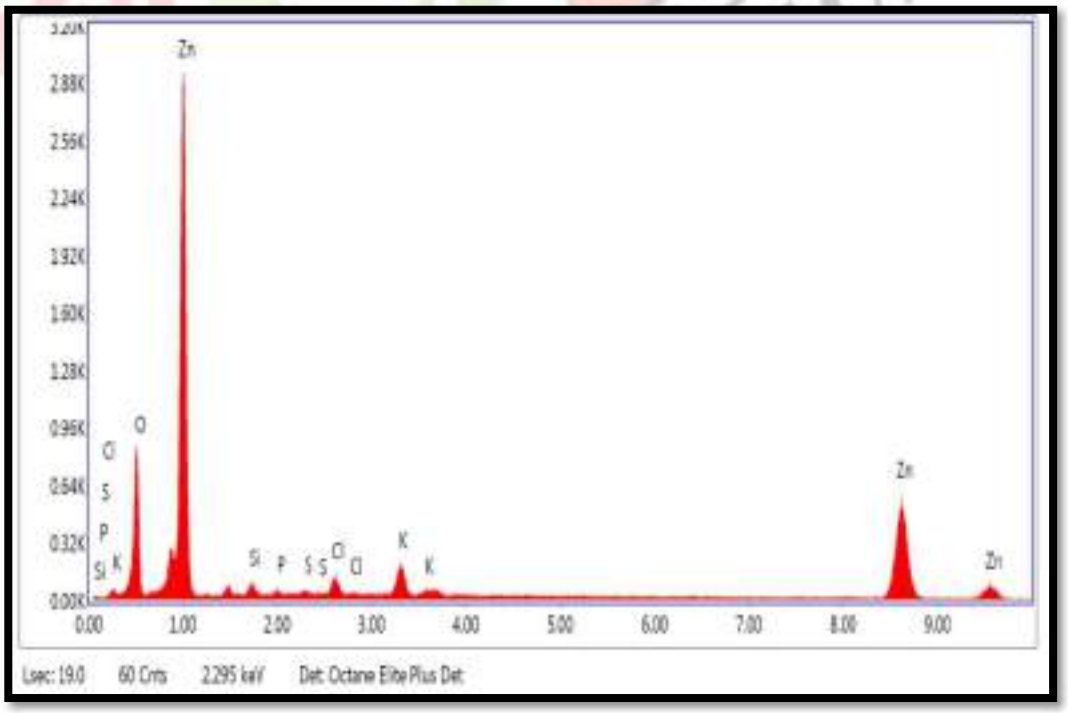

Figure 3: EDAX spectra of ZnO nanoparticles

Table 1: Elemental composition of ZnO nanoparticles

Element	Weight %	Atomic %
O	23.09	53.18
Zn	69.93	39.42

3.4 Fourier Transform Infrared spectroscopy (FTIR)

Synthesized zinc nanoparticles were subjected to FT-IR analysis to detect the various characteristic functional group associated with the synthesized nanoparticles. FTIR spectrum of the synthesized ZnO nanoparticles showed in Figure-4. The peaks indicate the characteristics functional group present in the synthesized zinc oxide nanoparticles. It is inferred that the samples have absorption peaks in the range of 3533.59 cm^{-1}, 3321.42 cm^{-1}, 1178.71 cm^{-1}, 1045.42 cm^{-1}, and 410.84 cm^{-1}[16]. The absorption peak at 410.84 to 575.9 cm^{-1}corresponds to metal-oxygen (ZnO stretching vibrations) vibration mode. The peak at 1045.42 $cm^{-1}$is ascribed to the stretching vibration of C-N bond of the primary amine or to the stretching vibration of the C-O bond of the primary alcohol. The peak at 1178.71 $cm^{-1}$was ascribed to primary alcohol in-plane bend or vibration. The peaks at 3321.42 $cm^{-1}$and 3533.59 $cm^{-1}$are ascribed to the stretching vibration of hydroxyl compounds [19, 20].

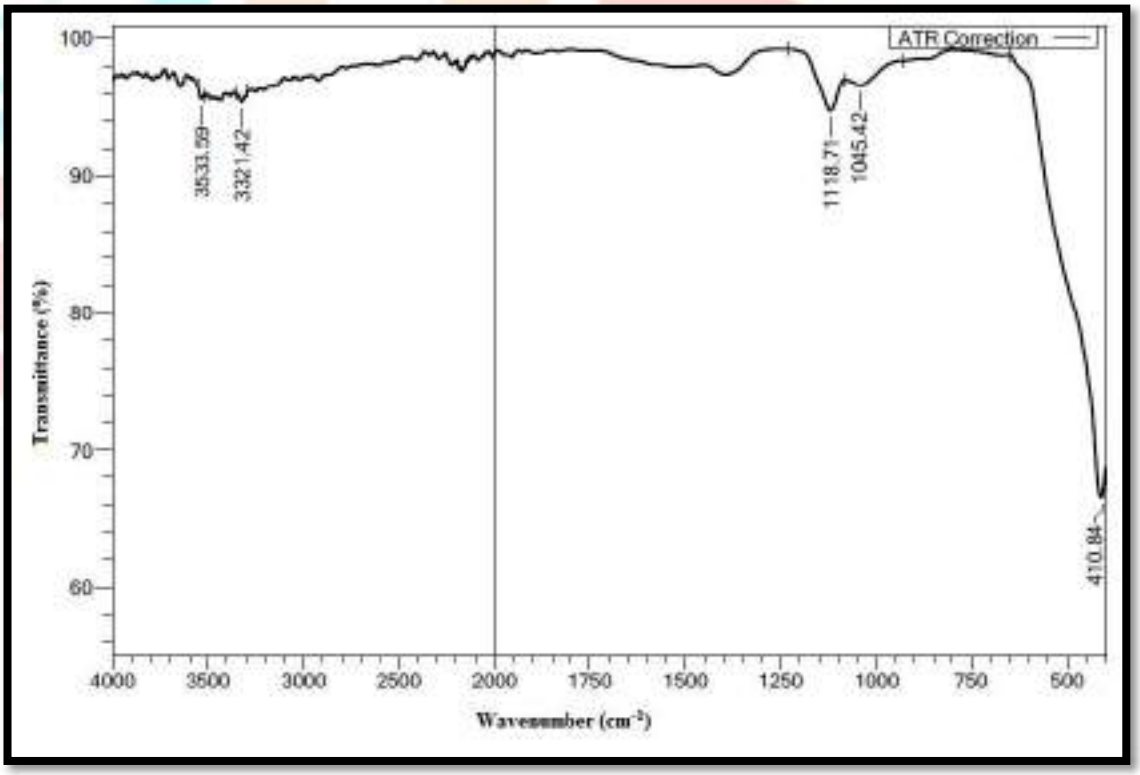

Figure 4: FTIR spectra of ZnO nanoparticles

4. Conclusion and Discussion:

ZnO nanoparticles were successfully synthesized by green synthesis method using Zinc nitrate hexahydrate and wheat grass pieces. SEM analyses revealed that the synthesized ZnO was spherical in shape and particle size ranged from 37.77 to 64.13 nm.The crystallite size and purity of the sample are investigated by XRD.In FTIR spectroscopy, pure ZnO nanoparticles showed stretching vibrations and peaks were match with standard fictional groups of ZnO.

Acknowledgment:

The authors thank to Principal, L. V. H. College and Research Centre in Electronic Science, Panchavati, Nashik, India, for providing laboratory facilities. The authors also acknowledge and pay sincere thanks to Head, Department of Physics, S. P. Pune University, Pune for providing the laboratory facilities for SEM, EDAX, and XRD characterization for present research work.

References:

1. Kouhbanani, M.A.J., Beheshtkhoo, N., Fotoohiardakani, G., Hosseini-Nave, H., Taghizadeh, S. and Amani, A.M., 2019. Green synthesis and characterization of spherical structure silver nanoparticles using wheatgrass extract. *Journal of Environmental Treatment Techniques*, *7*(1), pp.142-149.
2. Naseer, M., Aslam, U., Khalid, B. and Chen, B., 2020. Green route to synthesize Zinc Oxide Nanoparticles using leaf extracts of Cassia fistula and Meliaazadarach and their antibacterial potential. *Scientific Reports*, *10*(1), pp.1-10.
3. Patil, A.V., Dighavkar, C.G., Sonawane, S.K. and Borse, R.Y., 2010. Effect of firing temperature on structural parameters of screen printed ZnO thick films. *Invertis Journal of Science & Technology*, *3*(4), pp.207-214.
4. Barzinjy, A.A. and Azeez, H.H., 2020. Green synthesis and characterization of zinc oxide nanoparticles using Eucalyptus globulusLabill. leaf extract and zinc nitrate hexahydrate salt. *SN Applied Sciences*, *2*(5), pp.1-14.
5. Wagh, M.S., Jain, G.H., Patil, D.R., Patil, S.A. and Patil, L.A., 2006. Modified zinc oxide thick film resistors as NH_3 gas sensor. *Sensors and Actuators B: Chemical*, *115*(1), pp.128-133.
6. M Awwad, A., Albiss, B. and L Ahmad, A., 2014. Green synthesis, characterization and optical properties of zinc oxide nanosheets using Oleaeuropea leaf extract. *Advanced Materials Letters*, *5*(9), pp.520-524.
7. Xu, H., Wang, H., Zhang, Y., Wang, S., Zhu, M. and Yan, H., 2003. Asymmetric twinning crystals of zinc oxide formed in a hydrothermal process. *Crystal Research and Technology: Journal of Experimental and Industrial Crystallography*, *38*(6), pp.429-432.
8. Mazzeo, M.F., Di Stasio, L., D'Ambrosio, C., Arena, S., Scaloni, A., Corneti, S., Ceriotti, A., Tuberosa, R., Siciliano, R.A., Picariello, G. and Mamone, G., 2017. Identification of early represented gluten proteins during durum wheat grain development. *Journal of Agricultural and Food Chemistry*, *65*(15), pp.3242-3250.
9. Ben-Arye, E., Goldin, E., Wengrower, D., Stamper, A., Kohn, R. and Berry, E., 2002. Wheat grass juice in the treatment of active distal ulcerative colitis: a randomized double-blind placebo-controlled trial. *Scandinavian journal of gastroenterology*, *37*(4), pp.444-449.

10. Shaikh, F., Panhwar, Q.K., Balouch, A., Ali, S., Panhwar, W.A. and Sheikh, F., 2020. Synthesis of zinc oxide nanoparticles and their functionalisation with chrysin: Exploration of its applications. *International Journal of Environmental Analytical Chemistry*, pp.1-10.
11. Elmorsi, T.M., Elsayed, M.H. and Bakr, M.F., 2017. Enhancing the removal of methylene blue by modified ZnO nanoparticles: kinetics and equilibrium studies. *Canadian Journal of Chemistry*, *95*(5), pp.590-600.
12. Chen, X., Jing, X., Wang, J., Liu, J., Song, D. and Liu, L., 2013. Self-assembly of ZnO nanoparticles into hollow microspheres via a facile solvothermal route and their application as gas sensor. *CrystEngComm*, *15*(36), pp.7243-7249.
13. Chithambo, M.L., Nyirenda, A.N., Finch, A.A. and Rawat, N.S., 2015. Time-resolved optically stimulated luminescence and spectral emission features of α-Al2O3: C. *Physica B: Condensed Matter*, *473*, pp.62-71.
14. Kim, S.J. and Park, D.W., 2009. Preparation of ZnO nanopowders by thermal plasma and characterization of photo-catalytic property. *Applied surface science*, *255*(10), pp.5363-5367.
15. Ong, C.B., Ng, L.Y. and Mohammad, A.W., 2018. A review of ZnO nanoparticles as solar photocatalysts: Synthesis, mechanisms and applications. *Renewable and Sustainable Energy Reviews*, *81*, pp.536-551.
16. Geetha, K., Chellapandian, M., Arulnathan, N. and Ramanathan, A., 2020. Nano zinc oxide–An alternate zinc supplement for livestock. *Veterinary World*, *13*(1), p.121.
17. Raj, L.F.A. and Jayalakshmy, E., 2015. Biosynthesis and characterization of zinc oxide nanoparticles using root extract of Zingiberofficinale. *Orient. J. Chem*, *31*(1), pp.51-56.
18. Rawashdeh, R.Y., Harb, A.M. and AlHasan, A.M., 2020. Biological interaction levels of zinc oxide nanoparticles; lettuce seeds as case study. *Heliyon*, *6*(5), p.e03983.
19. Mousa, M.A. and Khairy, M., 2020. Synthesis of nano-zinc oxide with different morphologies and its application on fabrics for UV protection and microbe-resistant defense clothing. *Textile Research Journal*, *90*(21-22), pp.2492-2503.
20. Getie, S., Belay, A., Chandra Reddy, A.R. and Belay, Z., 2017. Synthesis and characterizations of zinc oxide nanoparticles for antibacterial applications. *J NanomedNanotechno S*, *8*(004).

Certificate of Publication

INTERNATIONAL JOURNAL OF CREATIVE RESEARCH THOUGHTS | ISSN: 2320 - 2882

An International Open Access, Peer-reviewed, Refereed Journal

The Board of

International Journal of Creative Research Thoughts

Is hereby awarding this certificate to

Umesh. J. Tupe

In recognition of the publication of the paper entitled

SYNTHESIS AND CHARACTERIZATION OF ZINC OXIDE NANOPARTICLES USING GREEN SYNTHESIS METHOD

Published In IJCRT (www.ijcrt.org) & 7.97 Impact Factor by Google Scholar

Volume 10 Issue 2 February 2022 , Date of Publication: 25-February-2022

UGC Approved Journal No: 49023 (18)

PAPER ID : IJCRTL020042

Registration ID : 216280

ISSN 2320-2882 IJCRT

EDITOR IN CHIEF

Scholarly open access journals, Peer-reviewed, and Refereed Journals, Impact factor 7.97 (Calculate by google scholar and Semantic Scholar | AI-Powered Research Tool) , Multidisciplinary, Monthly Journal

INTERNATIONAL JOURNAL OF CREATIVE RESEARCH THOUGHTS | IJCRT

An International Scholarly, Open Access, Multi-disciplinary, Indexed Journal

Website: www.ijcrt.org | Email id: editor@ijcrt.org | ESTD: 2013

IJCRT | ISSN: 2320-2882 | IJCRT.ORG

Certificate of Publication

INTERNATIONAL JOURNAL OF CREATIVE RESEARCH THOUGHTS | ISSN: 2320 - 2882

An International Open Access, Peer-reviewed, Refereed Journal

The Board of

International Journal of Creative Research Thoughts

Is hereby awarding this certificate to

Umesh J. Tupe

In recognition of the publication of the paper entitled

SYNTHESIS AND CHARACTERIZATIONS OF CUO-ZNO NANO COMPOSITE BINARY OXIDE THICK FILMS AS H2S GAS SENSOR

Published In IJCRT (www.ijcrt.org) & 7.97 Impact Factor by Google Scholar

Volume 10 Issue 2 February 2022 , Date of Publication: 25-February-2022

UGC Approved Journal No: 49023 (18)

ISSN 2320-2882 IJCRT

PAPER ID : IJCRTL020023

Registration ID : 216302

EDITOR IN CHIEF

Scholarly open access journals, Peer-reviewed, and Refereed Journals, Impact factor 7.97 (Calculate by google scholar and Semantic Scholar | AI-Powered Research Tool) , Multidisciplinary, Monthly Journal

INTERNATIONAL JOURNAL OF CREATIVE RESEARCH THOUGHTS | IJCRT

An International Scholarly, Open Access, Multi-disciplinary, Indexed Journal

Website: www.ijcrt.org | Email id: editor@ijcrt.org | ESTD: 2013

IJCRT | ISSN: 2320-2882 | IJCRT.ORG

Certificate of Publication

INTERNATIONAL JOURNAL OF CREATIVE RESEARCH THOUGHTS | ISSN: 2320 - 2882

An International Open Access, Peer-reviewed, Refereed Journal

The Board of

International Journal of Creative Research Thoughts

Is hereby awarding this certificate to

Umesh. J. Tupe

In recognition of the publication of the paper entitled

REVIEW ON: SYNTHESIS OF PEROVSKITE USING SOL-GEL APPROACH

Published In IJCRT (www.ijcrt.org) & 7.97 Impact Factor by Google Scholar

Volume 10 Issue 2 February 2022 , Date of Publication: 25-February-2022

UGC Approved Journal No: 49023 (18)

PAPER ID : IJCRTL020041

Registration ID : 216281

ISSN 2320-2882 IJCRT

EDITOR IN CHIEF

Scholarly open access journals, Peer-reviewed, and Refereed Journals, Impact factor 7.97 (Calculate by google scholar and Semantic Scholar | AI-Powered Research Tool) , Multidisciplinary, Monthly Journal

INTERNATIONAL JOURNAL OF CREATIVE RESEARCH THOUGHTS | IJCRT

An International Scholarly, Open Access, Multi-disciplinary, Indexed Journal

Website: www.ijcrt.org | Email id: editor@ijcrt.org | ESTD: 2013

IJCRT | ISSN: 2320-2882 | IJCRT.ORG